The Pennsylvania State University

The Graduate School

SYNTHESIS AND CHARACTERIZATION OF TRANSITION METAL NITRIDE AND SELENIDE NANOCRYSTALS AND HETEROSTRUCTURES

A Dissertation in

Chemistry

by

Robert W. Lord

Submitted in Partial Fulfillment
of the Requirements
for the Degree of

Doctor of Philosophy

August 2021

The dissertation of Robert W. Lord was reviewed and approved by the following:

Raymond E. Schaak
DuPont Professor of Materials Chemistry
Professor of Chemical Engineering
Dissertation Advisor
Chair of Committee

Kenneth L. Knappenberger, Jr
Professor of Chemistry

Benjamin J. Lear
Associate Professor of Chemistry

Venkatraman Gopalan
Professor of Material Science and Engineering
Professor of Physics

Philip C. Bevilacqua
Distinguished Professor of Chemistry
Distinguished Professor of Biochemistry and Molecular Biology
Head of the Department

ABSTRACT

The properties of nanomaterials are intimately dependent on their size, morphology, composition both elemental and structural, as well as their crystal structure or atomic arrangement. There exists a fundamental need to develop methods to precisely control and tune these parameters in order to target desirable materials. Colloidal chemistries utilize wet chemical precursors to synthesize inorganic nanomaterials from the bottom up and produce high quality materials. In addition to single component material synthesis, colloidal chemistries have been developed to synthesize multicomponent nanomaterials systems through a process called seeded growth. Seeded growth utilizes preformed nanoparticles as substrates to nucleate and grow new materials from their surfaces. This has led to the synthesis of highly complex heterostructured nanoparticles which allow for the incorporation of multiple material properties within single particle frameworks. While these techniques can control the structure and composition of the synthesized material, they do not allow for as much control over the resulting crystal structure. Other methods have been developed which allow for crystallographic templating and compositional modulation by post-synthetic cation exchange. Cation exchange utilizes molecular agents to solvate and exchange host cations in preformed crystals with those in solution while maintaining the anion sublattice relatively unperturbed. The crystallographic symmetry of the anion sublattice determines the symmetry of the final product phase. As such, cation exchange has allowed researchers to synthesize materials which are either metastable in bulk or not easily assessable through other methods.

In this dissertation I discuss my efforts to utilize these synthetic tools to synthesize new and complex inorganic nanoparticles. First, I describe the seeded growth of Cu_3N and Cu_3PdN on Pt and Au nanocrystals. Utilizing Pt-Cu_3PdN as the model system, it was observed that Cu_3PdN nucleated and grew in a step-wise pathway with the initial deposition of Cu onto the surface. This was followed by the deposition of Pd onto the corners and edges of the Pt nanocubes which was

followed by the coalescence and crystallization of Cu with the Pd to ultimately give Cu_3PdN. When nucleating on more faceted or spherical seeds, whether Pt or Au, the resulting heterostructures took on more core@shell structures. In the absence of Pd, Cu_3N nucleates indiscriminately on the surface of Pt without any of the regioselectivity seen with Cu_3PdN. When utilizing Au seeds, AuCu alloy formation is observed without any apparent heterostructure formation. These observations helped us develop guidelines which are anticipated to be applicable to the formation of other ternary nitride heterostructures.

Second, I discuss the synthesis of a new, metastable phase of copper selenide nanoparticles. This material was shown by EDS and XPS to adopt a nominally 2:1 stoichiometry and the XRD pattern did not match any known phase of $Cu_{2-x}Se$. However, the nanoparticles did adopt a crystal structure similar to previously observed weissite $Cu_{2-x}Te$. A structural model for our $Cu_{2-x}Se$ phase was developed utilizing a recently reported structural model for weissite $Cu_{2-x}Te$ which was computationally verified in collaboration with Professor Ismaila Dabo's group. Weissite-like $Cu_{2-x}Se$ has trigonal symmetry (space group $P\bar{3}m1$) and is a layered structure with alternative Cu-rich and Cu-deficient layers sandwiched between layers of Se. UV-vis-NIR spectroscopy of weissite-like $Cu_{2-x}Se$ showed a broad plasmon absorbance band centered around 1550 nm.

Lastly, I discuss my efforts to develop synthetic guidelines for the competitive synthesis of ternary copper selenide phases during their nucleation on Pt nanoparticle seeds. We showed experiments which allude to two potential synthetic pathways for the formation of $CuFeSe_2$ and $CuInSe_2$. It was observed that the $CuInSe_2$ forms through a multistep pathway starting with the initial nucleation of $Cu_{2-x}Se$ followed by the incorporation of the In^{3+} through a high temperature cation exchange reaction. However, $CuFeSe_2$ was shown to most likely to form by direct nucleation. The differences in these reactions were observed when their simultaneous nucleation was attempted, where only Pt–$CuInSe_2$ formed.

TABLE OF CONTENTS

LIST OF FIGURES

LIST OF TABLES

ACKNOWLEDGEMENTS

First and foremost, I want to thank my parents, Lucille and David Lord. Thank you for your love and support throughout my life. I wouldn't have been here without your wisdom, guidance, and teaching me to take the ups and downs in life with laughter and humility. Thank you so much.

I want to thank my friends near and far for being there for me and helping keep me sane. I appreciate all the conversations and laughter we have shared. I want to thank one of my best friends, Nathan Wood, who's persistent curiosity and steadfast friendship has bolstered me through these many long years. I want to thank all the members of the Schaak lab, past and present, for being such an amazing group of people who have continued to push me to be a better scientist. I want to thank Ben Steimle for all the conversations and laughs we shared both as the old men in lab and desk mates. I want to thank all the people whom I have had the fortune to work on projects with; Dr. Julie Fenton, Dr. Lucas Alameda, Dr. Cameron Holder, Dr. Emil A. Hernández-Pagán, Dr. Katherine Plass, Dr. Kenneth L. Knappenberger Jr., Dr. Ismaila Dabo, Ben Steimle, Abigail Fagan, Julian Fanghanel, Auston Butterfield, Rebecca Katz, Katelyn Baumler, Gabriella Di Domizio, Connor McCormick, Sarah O'Boyle, Joseph M. Veglak, Katherine Thompson, and Gaurav R. Dey.

I want to acknowledge my thesis advisor, Raymond E. Schaak. His guidance and support have pushed me to strive for the highest level of academic and professional excellence. I could not have asked for a better mentor and friend to help guide me through the ups and downs of graduate school. Thank you, Ray. I also want to thank my committee, Benjamin J. Lear, Kenneth L. Knappenberger Jr., and Venkatraman Gopalan, for reading this dissertation and providing their support during my time here at Penn State.

Last but certainly not least, I want to thank my wonderful wife, Trâm Lord, without whom I would not be where I am today. I owe my success to your endless love and support. Thank you

for always being in my corner and pushing me to be the best person possible and breaking me out of my comfort zone. I look forward to a lifetime of adventures together. I love you.

The material presented in this dissertation was supported by the U.S. National Science Foundation (NSF) under grant CH-1707830, grant DMR-1904122, DMREF and INFEWS programs of the NSF under grant DMREF-1729338. This work was also supported by funds from the Pennsylvania State University. Any findings, conclusions, recommendations, or opinions expressed in this publication are those of the authors and do not necessarioy reflect the views of the NSF or the Pennsylvania State University.

Chapter 1

Introduction

1.1 Colloidal Synthesis of Inorganic Nanoparticles

Over the past several decades, there has been extensive research efforts into the discovery and development of inorganic nanomaterials. Nanomaterials often possess properties unique to their bulk counterparts due to their large surface–to–volume ratios and size-dependent optical and electronic properties.[1] For example, metallic nanoparticles (e.g., Ag, Au, and Al) possess tunable optical absorbances and observed color due to the interaction between their surface plasmons and incident light.[2–4] In catalytic applications, shape control allows for the development of catalysts which terminate in high activity facets and surface sites such as step edges and corners.[5] Advances in these applications and others are underpinned by a need for synthetic methods which produce high quality nanoparticles with tight control over their size, shape, and crystal structure. Colloidal synthesis has become one the most effective methods to produce high quality, monodisperse nanoparticles using wet chemical agents through a bottom up approach. Compared to other methods of producing high quality nanoparticles, wet chemical approaches are more readily scalable allowing for more rapid materials development and discovery. Colloidal nanoparticles are readily processed for a variety of applications such as catalysis,[6] optoelectronics,[7] biomedical imaging,[8] as well as energy production and storage.[9–10] There are a number of colloidal methods to synthesize high quality nanoparticles though the most commonly used are heat up approaches,[11] hot-injection,[12] and seeded growth.[13] Before discussing these approaches, it is prudent to understand how nanoparticles nucleate and grow to better understand how to control their property-defining features.

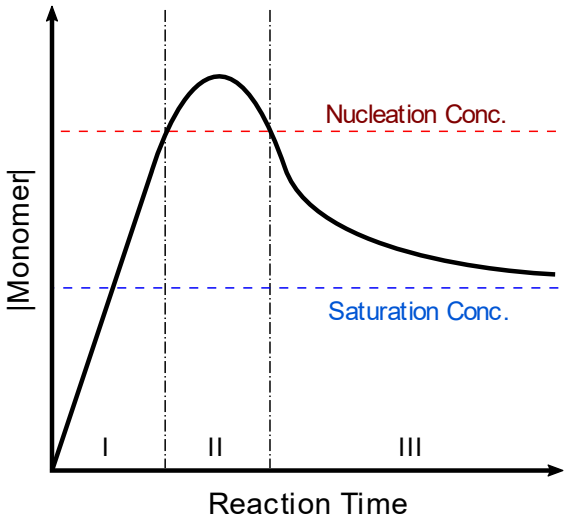

Figure 1.1: Schematic representation of the concentration of precursor monomers during nanoparticle synthesis. Initial monomer formation (region I) occurs by the decomposition of precursor salts or molecular compounds. After reaching critical concentrations (region II) nucleation of atomic aggregates and clusters occurs using up solution monomers. The growth regime (region III) occurs after monomer concentration decreases below the critical concentration for spontaneous nucleation but remains above the solution saturation concentration. Modified and reproduced with permission from ref 14. Copyright 1950 American Chemical Society.

The mechanism by which nanoparticles nucleate and grow is a topic of continual research, though the prevailing mechanism is believed to follow the theory proposed by LaMer and coworkers.[14] Their theory proposed that there were essentially three regimes depending on the concentration of reactive monomers in solution, seen in Figure 1.1. Initially, metal precursor reagents (e.g., salts and molecular compounds) decompose in solution to form monomer building blocks.[15–17] As the reaction continues, the concentration of these monomers increases beyond the saturation concentration until it reaches a critical concentration where aggregation is favorable causing the spontaneous nucleation of atomic clusters.[18] As the precursor reagents are used up, monomer concentration dips below the necessary levels to sustain nucleation. If this concentration remains above the saturation limit of the solution, growth of the nucleated aggregates occurs. Tuning the rate of monomer formation through careful control over reaction temperature, ligand and solvent mixtures, and reagent reactivity allow for the careful control over particle size, morphology, polydispersity, and crystal structure, seen in Figure 1.2.[19–20] Decades of research have

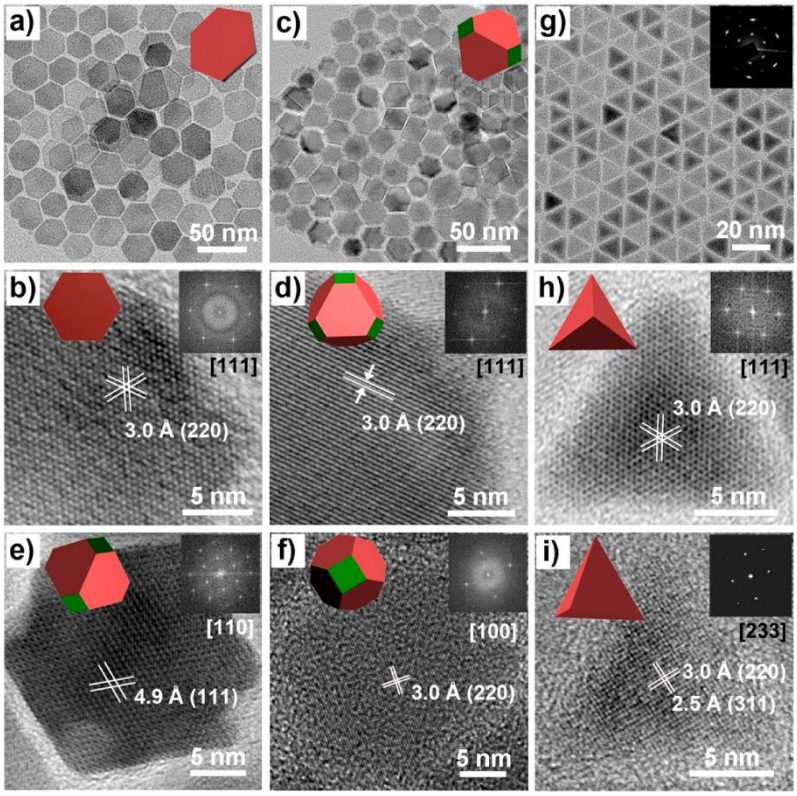

Figure 1.2: Transmission electron microscope (TEM) images with accompanying electron diffraction (ED), fast Fourier transform (FFT), and cartoon rendering of various morphologies of monodispersed Fe_3O_4 nanoparticles synthesized through the modulation of precursor concentration, solvent–surfactant mixture, time, and temperature. Lattice spacings and associated crystallographic planes show the different surface facets associated with the different morphologies. Reproduced with permission from ref 20. Copyright 2015 American Chemical Society.

been devoted to understanding how to tune these synthetic parameters and the library of high quality, colloidally accessible inorganic nanocrystals of diverse shape and crystal structure continues to grow.

As previously mentioned, the most commonly used methods in colloidal nanochemistry are heat up, hot-injection, and seeded growth. I will discuss seeded growth in greater detail in Section 1.2. Heat up approaches, favored for their relative simplicity, utilize single pot reaction mixtures where all the precursors are present at the start of the reaction then heated up to the desired temperatures.[11] These reactions favor continuous nucleation and growth with monomer concentrations primarily being controlled by reagent reactivities, temperature ramp rates, and

reaction times. Hot-injection reactions utilized the injection of precursor mixtures injected into hot solvent and surfactants causing burst nucleation from rapid monomer formation leading to narrow size distributions.[21] Additionally, the rate precursor is introduced into the reaction can enact control over monomer concentration allowing for size and shape control.[22] The diversity of inorganic nanoparticles synthesized by these two methods grown tremendously to include metals,[23] metal oxides,[24] metal pnictides,[25, 26] metal chalcogenides,[27] and metal halides.[28, 29]

1.2 Seeded Growth Synthesis to Form Heterostructured Inorganic Nanoparticles

As the methods for synthesizing nanoparticles using single material components have evolved so has our understanding of how to create materials of increasing sophistication and functionality. One way material complexity can be engineered to increase functionality is the incorporation of multiple materials within a single nanoparticle framework. One of the most widely used methods to integrate multiple materials is by seeded growth; the process by which preformed nanoparticles are used as substrates to nucleate new material domains forming new heterostructured nanoparticles.[30] Heterostructured nanoparticles, sometimes called hybrid nanoparticles, are characterized by the formation of one or more new discreet domains on the seed crystals. They are characterized by their solid-state interface between each disparate material.[31] This interface allows for the direct electronic communication between materials with potential for synergistic or emergent properties not attributable to each component individually.[32] Additionally, particle complexity and functionality can be further enhanced by utilizing multiple sequential seeded growth steps to form higher order hybrid systems (e.g., two-component dimer, three-component trimer, and four-component tetramer).[33] The library of material systems which have been interfaced in this way has grown significantly to include metal-metal,[34] metal-metal oxide,[35] metal oxide-metal oxide,[36] metal-metal chalcogenides,[37] metal-metal pnictides,[38] and more highlighting the versatility of seeded growth synthesis.[39] This expansive library of materials has been extensively

studied for their applications in catalysis,[40] biomedical imaging,[41] energy harvesting,[42] and optoelectronics.[43]

While heterostructured nanoparticles have sparked great enthusiasm and seen much success, progress is hampered by our lack of control over domain locality. This is even further exacerbated when more than two materials are interfaced, as seen in Figure 1.3, where having multiple domains available for nucleation can lead to numerous possible configurations.[31] Overlooked or nuanced factors may preference one heterostructure over another or indeed could provide insights into ways of directing nucleation. For example, Hodges et al. observed that when nucleating Ag on Pt–Fe_3O_4 nanoparticles the Ag first nucleates on the Fe_3O_4 domain then

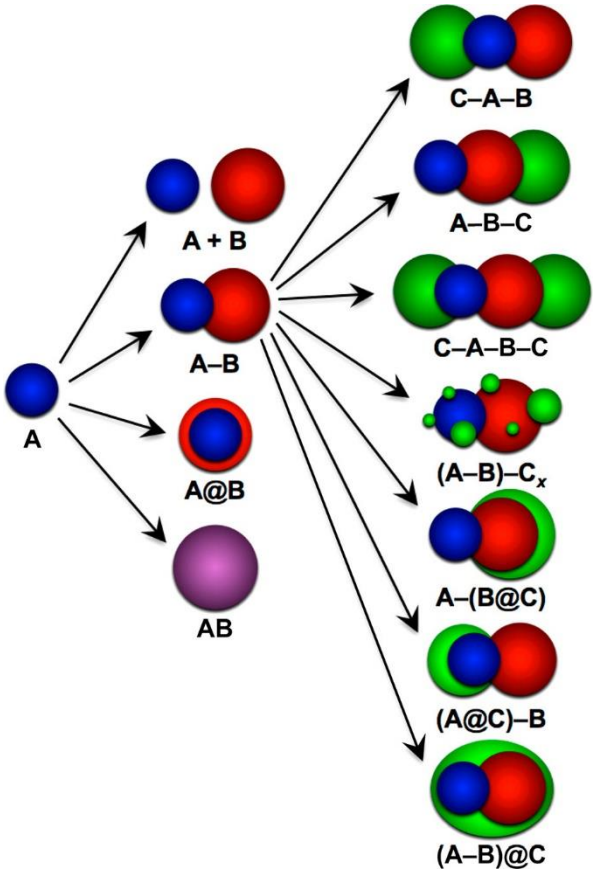

Figure 1.3: Cartoon representations of the possible configurations two-component and three-component hybrid nanoparticles highlighting the increasing configurational complexity in multicomponent systems. Reproduced with permission from ref 31. Copyright 2017 American Chemical Society.

subsequently surface migrates to coalescence on the Pt domain.[44] Additionally, they observed that the presence of a small FeO_x shell on the surface of Pt nanoparticle seeds, which formed during the synthesis of Pt–Fe_3O_4 heterodimer seeds, could direct or limit the nucleation of Ag when trying to form the heterotrimer nanoparticles. Another example of nuance in hybrid nanoparticle synthesis was observed by Saunders et al. who observed different nucleation behaviors when Au was nucleated on CdS in the presence or absence of air during the reaction.[45] They hypothesized that air exposure increased the number of vacancies on the surface of CdS nanorods which acted as nucleation sites for Au resulting in multiple domains of Au growing on the nanorods. When air was absent in the reaction, only a single domain of Au grew on the tips of the rods. Insights such as these can help us better understand the factors which affect heterostructure formation and allow the development of synthetic protocols and guidelines which will allow for the rational control over heterostructure formation.

1.3 Nanoscale Cation Exchange Reactions

In Section 1.1, I outlined some of the wet chemical methods developed for the direct synthesis of high quality, monodispersed nanoparticles possessing many unique morphologies and crystal structures. These methods often rely on the complex interplay of chemical precursors, high temperatures, and nucleation and growth processes. Even though our knowledge in this area has grown significantly, advances remain largely due to serendipity. Cation exchange offers researchers a predictable synthetic framework for tuning nanoparticle composition and crystal structure.[46, 47]

Due to their size, diffusion pathways in nanoparticles are inherently short meaning that mobile cations in their crystalline lattices can be extracted and replaced with solvated cations in solution. This process is driven by the differences in binding affinities between cations and ligands in solution and cations in the host nanocrystal rationalized by Pearson's hard-soft acid-base theory.[48] For example, softer cations such as Cu^+ or Ag^+ can be extracted using soft, bulky bases

such as trioctylphosphine (TOP) or thiols and replaced by harder cations such as Cd^{2+} or Zn^{2+} all the while leaving the anion sublattice relatively unperturbed.[49, 50]

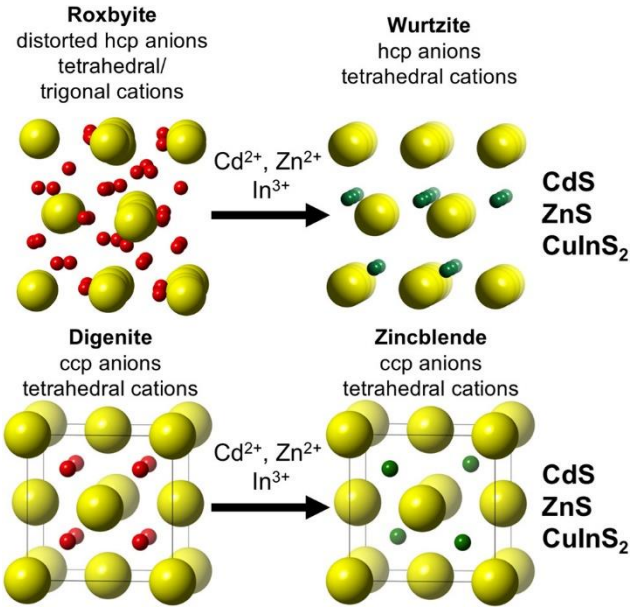

Figure 1.4: Schematic diagrams of the accessible crystal structures obtained through crystallographic templating of different polymorphs of $Cu_{2-x}S$ nanoparticles. Cu atoms are red, S atoms are yellow, and Cd/Zn/In atoms are green. Reproduced with permission from ref 51. Copyright 2019 American Chemical Society.

The symmetry of the anion sublattice (e.g., hexagonally closed packed or cubic closed packed) in the host nanocrystal is retained through the exchange reaction, seen in Figure 1.4, along with particle morphology.[51] Crystallographic templating in this way has allow access a library of material polymorphs without having to develop individual protocols to access each material. Interestingly, when Manna and coworkers performed a Cu^{+} exchange on CdSe nanoparticles, the resulting $Cu_{2-x}Se$ nanoparticles were of a previously unknown phase not observable on the bulk Cu–Se phase diagram.[52] Their result implies the potential of cation exchange to allow researchers access to new, non-equilibrium material phases which may not be accessible through other means. Since morphology is retained during cation exchange, only the chemistries to control starting particle morphology are needed allowing access to desirable morphologies which may be difficult to obtain if not completely inaccessible through direct synthetic methods.[47]

1.4 Experimental Work

In this dissertation, I describe my efforts to discover new inorganic nanomaterials and develop synthetic guidelines to control their morphology, crystal structure, and composition. In Chapter 2, I present the synthesis of heterostructured, transition metal nitride nanoparticles by seeded growth on noble metal seeds. Transition metal nitrides represent a class of material which has largely been missing from the hybrid nanoparticle literature due to issues with colloidally available nitrogen sources. Cu_3N and Cu_3PdN were chosen for their colloidal accessibility at moderate temperatures and reaction conditions. Cu_3N and Cu_3PdN heterostructures were synthesized by seeded growth on Au and Pt seeds. The morphologies of the resulting heterostructures were shown to vary depending on a number of factors. When seeding the growth of Cu_3PdN, the degree of faceting of the starting seed was shown to modulate the final heterostructure morphology from regioselective growth on nanocubes to indiscriminate surface nucleation on nanospheres. When seeding the growth of Cu_3N, no regioselective growth was observed when using Pt seeds regardless of seed morphology. When using Au seeds, no Cu_3N heterostructures formed, instead favoring the formation of AuCu alloy nanoparticles. Focusing on the Pt–Cu_3PdN system, it was shown that the Cu_3PdN domains formed through a multistep process. First, Cu deposits on the surface followed by the deposition of Pd onto the high energy surfaces (edges and corners) then the simultaneous coalescence and crystallization of Cu_3PdN. Using the guidelines developed from these observations, we were able to synthesize a highly complex, multicomponent heterostructure using Pt–Fe_3O_4 seeds. A number of characterization techniques were used in this study, including transmission electron microscopy (TEM), high-resolution TEM (HRTEM), selected area electron diffraction (SAED), scanning transmission electron microscopy (STEM), energy dispersive spectroscopy coupled with STEM (STEM-EDS), X-ray diffraction (XRD), and X-ray photoelectron spectroscopy (XPS). This work was a collaborative effort with Dr. Julie L. Fenton and Dr. Cameron F. Holder assisting with the materials characterization.

In Chapter 3, I present the synthesis of a metastable phase of $Cu_{2-x}Se$ nanoparticles with near infrared (NIR) plasmon absorbance. Since the properties of materials are dependent on their atomic arrangements or crystal structure, significant research efforts have been devoted to the discovery of new crystalline phases and controlling crystal structure. Copper selenides have received significant attention for their applications in catalysis, plasmonics, and energy storage. I demonstrated the synthesis of copper selenide nanoparticles which take on a hexagonal, platelet morphology as observed by TEM. Elemental analysis by EDS and XPS showed a nominal Cu:Se stoichiometry of 2:1. When comparing the XRD pattern of our $Cu_{2-x}Se$ nanoparticles, it did not match any known phase of copper selenide. Expanding our search to other copper chalcogenide systems showed our material was similar to the pattern for weissite $Cu_{2-x}Te$. Utilizing a previous computational model for the structure of weissite $Cu_{2-x}Te$, we were able to develop, with the help of Professor Ismaila Dabo's group, a structural model for our $Cu_{2-x}Se$ material. The crystal structure of weissite-like $Cu_{2-x}Se$ has trigonal symmetry with space group $P\bar{3}m1$. The structure is a layered structure characterized by Cu-rich and Cu-deficient layers sandwiched by Se. HRTEM imaging of our nanoparticles showed atomic positions and lattice spacings which match those predicted by our structural model. Thermal annealing studies were performed on our nanoparticles to test their stability. Extended reaction times and high temperature thermal annealing showed the weissite-like phase does not persist and the particles undergo a phase change to the cubic berzelianite $Cu_{2-x}Se$ phase. As $Cu_{2-x}Se$ has been shown to be plasmonic, we analyzed our particles by UV-vis-NIR spectroscopy which showed a broad plasmon absorbance band centered around 1550 nm. The particles were additionally shown to be relatively oxidatively stable with little shifting of the plasmon band under reductive and oxidative conditions. This work was done in collaboration with Dr. Cameron F. Holder and Julian Fanghanel who assisted with the XPS characterization and computational work, respectively.

In Chapter 4, I demonstrate the synthesis of ternary copper selenide heterostructures seeded on Pt nanoparticle seeds. The individual synthesis of $CuInSe_2$ and $CuFeSe_2$ seeded on preformed Pt nanoparticles. It was shown that when no additional metals were injected, trigonal $Cu_{2-x}Se$ nanoparticles were seeded onto the Pt nanoparticles to form Pt–$Cu_{2-x}Se$ heterodimers. To probe the synthetic pathway for ternary selenide formation, cation exchange reactions were done on the $Cu_{2-x}Se$ nanoparticles. It was shown that when using cadmium as an analogue for indium, wurtzite CdSe was formed validating the templating of the anion sublattice in trigonal $Cu_{2-x}Se$. To probe the potential mechanism for $CuFeSe_2$ growth, iron based cation exchange was developed and showed the formation of β-FeSe, showing the potential viability of an *in situ* cation reaction being the viable mechanism. However, when $Cu_{2-x}Se$ nanocrystals were subjected to the growth conditions for $CuFeSe_2$, no apparent exchange occurred, implying a different synthetic pathway; seeded nucleation and growth. However, when attempting to grow $CuFeSe_2$ and $CuInSe_2$ simultaneously, we only observed the formation of Pt–$CuInSe_2$ heterodimers. We concluded that there were competing mechanisms, step-wise nucleation and *in situ* cation exchange versus seeded nucleation. This was further validated when particle formation was chemically slowed with oleic acid. Particles were observed with incomplete indium incorporation with no apparent $CuFeSe_2$ particle formation. Understanding competitive processes in domain nucleation and growth is necessary for the development of methods for synthesizing complex heterostructures.

1.5 References

(1) Reske, R.; Mistry, H.; Behafarid, F.; Cuenya, B. R.; Strasser, P. Particle Size Effects in the Catalytic Electroreduction of CO_2 on Cu Nanoparticles. *J. Am. Chem. Soc.* **2014**, *136*, 6978–6986.

(2) González, A. L.; Noguez, C.; Beránek, J.; Barnard, A. S. Size, Shape, Stability, and Color of Plasmonic Silver Nanoparticles. *J. Phys. Chem. C* **2014**, *118*, 9128–9136.

(3) Link, S.; El-Sayed, M. A. Size and Temperature Dependence of the Plasmon Absorption of Colloidal Gold Nanoparticles. *J. Phys. Chem. B* **1999**, *103*, 4212–4217.

(4) Ekinci, Y.; Solak, H. H.; Löffler, J. F. Plasmon Resonances of Aluminum Nanoparticles and Nanorods. *J. Appl. Phys.* **2008**, *104*, 083107.

(5) Núñez, M.; Lansford, J. L.; Vlachos, D. G. Optimization of the Facet Structure of Transition-Metal Catalysts Applied to the Oxygen Reduction Reaction. *Nat. Chem.* **2019**, *11*, 449–456.

(6) Xie, C.; Niu, Z.; Kim, D.; Li, M.; Yang, P. Surface and Interface Control in Nanoparticle Catalysis. *Chem. Rev.* **2020**, *120*, 1184–1249.

(7) Gan, X. Y.; Crawford, S. E.; Eikey, E. A.; Sen, R.; Killinger, J. R.; Millstone, J. E. Optoelectronic Impacts of Particle Size in Water-Dispersible Plasmonic Copper Selenide Nanoparticles. *J. Phys. Chem. C* **2020**, *124*, 4747–4754.

(8) Han, X.; Xu, K.; Taratula, O.; Farsad, K. Applications of Nanoparticles in Biomedical Imaging. *Nanoscale* **2019**, *11*, 799–819.

(9) Nakayama, K.; Tanabe, K.; Atwater, H. A. Plasmonic Nanoparticle Enhanced Light Absorption in GaAs Solar Cells. *Appl. Phys. Lett.* **2008**, *93*, 121904.

(10) Wu, Z.-S.; Ren, W.; Wen, L.; Gao, L.; Zhao, J.; Chen, Z.; Zhou, G.; Li, F.; Cheng, H.-M. Graphene Anchored with Co_3O_4 Nanoparticles as Anode of Lithium Ion Batteries with Enhanced Reversible Capacity and Cyclic Performance. *ACS Nano* **2010**, *4*, 3187–3194.

(11) Van Embden, J.; Chesman, A. S. R.; Jasieniak, J. J. The Heat-Up Synthesis of Colloidal Nanocrystals. *Chem. Mater.* **2015**, *27*, 2246–2285.

(12) Timonen, J. V. I.; Seppälä, E. T.; Ikkala, O.; Ras, R. H. A. From Hot-Injection Synthesis to Heating-Up Synthesis of Cobalt Nanoparticles: Observation of Kinetically Controllable Nucleation. *Angew. Chem., Int. Ed.* **2011**, *50*, 2080–2084.

(13) Zong, R.; Wang, X.; Shi, S.; Zhu, Y. Kinetically Controlled Seed-Mediated Growth of Narrow Dispersed Silver Nanoparticles Up to 120 nm: Secondary Nucleation, Size Focusing, and Ostwald Ripening. *Phys. Chem. Chem. Phys.* **2014**, *16*, 4236–4241.

(14) LaMer, V. K.; Dinegar, R. H. Theory, Production and Mechanism of Formation of Monodispersed Hydrosols. *J. Am. Chem. Soc.* **1950**, *72*, 4847–4854.

(15) Xiong, Y.; Washio, I.; Chen, J.; Sadilek, M.; Xia, Y. Trimeric Clusters of Silver in Aqueous $AgNO_3$ Solutions and Their Role as Nuclei in Forming Triangular Nanoplates of Silver. *Angew. Chem., Int Ed.* **2007**, *46*, 4917–4921.

(16) Ciacchi, L. C.; Pompe, W.; De Vita, A. Initial Nucleation of Platinum Clusters after Reduction of K_2PtCl_4 in Aqueous Solution: A First Principles Study. *J. Am. Chem. Soc.* **2001**, *123*, 7371–7380.

(17) Ciacchi, L. C.; Pompe, W.; De Vita, A. Growth of Platinum Clusters via Addition of Pt(II) Complexes: A First Principles Investigation. *J. Phys. Chem. B* **2003**, *107*, 1755–1764.

(18) Wang, Y. W.; He, J. T.; Liu, C. C.; Chong, W. H.; Chen, H. Y. Thermodynamics Versus Kinetics in Nanosynthesis. *Angew. Chem., Int. Ed.* **2014**, *54*, 2022–2051.

(19) Xia, Y.; Xiong, Y.; Lim, B.; Skrabalak, S. E. Shape-Controlled Synthesis of Metal Nanocrystals: Simple Chemistry Meets Complex Physics? *Angew. Chem., Int. Ed.* **2008**, *48*, 60–103.

(20) Zhou, Z.; Zhu, X.; Wu, D.; Chen, Q.; Huang, D.; Sun, C.; Xin, J.; Ni, K.; Gao, J. Anisotropic Shaped Iron Oxide Nanostructures: Controlled Synthesis and Proton Relaxation Shortening Effects. *Chem. Mater.* **2015**, *27*, 3505–3515.

(21) Thanh, N. T. K.; Maclean, N.; Mahiddine, S. Mechanisms of Nucleation and Growth of Nanoparticles in Solution. *Chem. Rev.* **2014**, *114*, 7610–7630.

(22) Biacchi, A. J.; Schaak, R. E. The Solvent Matters: Kinetic Versus Thermodynamic Shape Control in the Polyol Synthesis of Rhodium Nanoparticles. *ACS Nano* **2011**, *5*, 8089–8099.

(23) Gilroy, K. D.; Ruditskiy, A.; Peng, H. -C.; Qin, D.; Xia, Y. Bimetallic Nanocrystals: Syntheses, Properties, and Applications. *Chem. Rev.* **2016**, *116*, 10414–10472.

(24) Park, J.; An, K.; Hwang, Y.; Park, J. -G.; Noh, H. -J.; Kim, J. -Y.; Park, J. -H.; Hwang, N. -M.; Hyeon, T. Ultra-Large-Scale Syntheses of Monodisperse Nanocrystals. *Nat. Mater.* **2004**, *3*, 891–895.

(25) Nakamura, T.; Hayashi, H.; Hanaoka, T.; Ebina, T. Preparation of Copper Nitride (Cu_3N) Nanoparticles in Long-Chain Alcohols at 130–200 °C and Nitridation Mechanism. *Inorg. Chem.* **2014**, *53*, 710–715.

(26) Mundy, M. E.; Ung, D.; Lai, N. L.; Jahrman, E. P.; Seidler, G. T.; Cossairt, B. M. Aminophosphines as Versatile Precursors for the Synthesis of Metal Phosphide Nanocrystals. *Chem. Mater.* **2018**, *30*, 5373–5379.

(27) Zhang, A.; Ma, Q.; Lu, M.; Zhou, G.; Li, C.; Wang, Z. Nanocrystalline Metal Chalcogenides Obtained Open to Air: Synthesis, Morphology, Mechanism, and Optical Properties. *J. Phys. Chem. C* **2009**, *113*, 15492–15496.

(28) Shamsi, J.; Urban, A. S.; Imran, M.; De Trizio, L.; Manna, L. Metal Halide Perovskite Nanocrystals: Synthesis, Post-Synthesis Modifications, and Their Optical Properties. *Chem. Rev.* **2019**, *119*, 3296–3348.

(29) Dong, H.; Du, S. -R.; Zheng, X. -Y.; Lyu, G. -M.; Sun, L. -D.; Li, L. -D.; Zhang, P. -Z.; Zhang, C.; Yan, C. -H. Lanthanide Nanoparticles: From Design Toward Bioimaging and Therapy. *Chem. Rev.* **2015**, *115*, 10725–10815.

(30) Banin, U.; Ben-Shahar, Y.; Vinokurov, K. Hybrid Semiconductor–Metal Nanoparticles: From Architecture to Function. *Chem. Mater.* **2014**, *26*, 97–110.

(31) Hodges, J. M.; Schaak, R. E. Controlling Configurational Isomerism in Three-Component Colloidal Hybrid Nanoparticles. *Acc. Chem. Res.* **2017**, *50*, 1433–1440.

(32) Figuerola, A.; Fiore, A.; Di Corato, R.; Falqui, A.; Giannini, C.; Micotti, E.; Lascialfari, A.; Corti, M.; Cingolani, R.; Pellegrino, T.; Cozzoli, P. D.; Manna, L. One-Pot Synthesis and Characterization of Size-Controlled Bimagnetic FePt–Iron Oxide Heterodimer Nanocrystals. *J. Am. Chem. Soc.* **2008**, *130*, 1477–1487.

(33) Buck, M. R.; Bondi, J. F.; Schaak, R. E. A Total Synthesis Framework for the Construction of High-Order Colloidal Hybrid Nanoparticles. *Nat. Chem.* **2012**, *4*, 37–44.

(34) Pellegrino, T.; Fiore, A.; Carlino, E.; Giannini, C.; Cozzoli, P. D.; Ciccarella, G.; Respaud, M.; Palmirotta, L.; Cingolani, R.; Manna, L. Heterodimers Based on $CoPt_3$–Au Nanocrystals with Tunable Domain Size. *J. Am. Chem. Soc*. **2006**, *128*, 6690– 6698.

(35) Wang, C.; Yin, H.; Dai, S.; Sun, S. A General Approach to Noble Metal–Metal Oxide Dumbbell Nanoparticles and Their Catalytic Application for CO Oxidation. *Chem. Mater*. **2010**, *22*, 3277–3282.

(36) Li, X.; Schaak, R. E. Size- and Interface-Modulated Metal–Insulator Transition in Solution-Synthesized Nanoscale VO_2-TiO_2-VO_2 Heterostructures. *Angew. Chem., Int. Ed.* **2017**, *56*, 15550– 15554.

(37) Hernández-Pagán, E. A.; Leach, A. D. P.; Rhodes, J. M.; Sarkar, S.; Macdonald, J. E. A. Synthetic Exploration of Metal–Semiconductor Hybrid Particles of $CuInS_2$. *Chem. Mater.* **2015**, *27*, 7969–7976.

(38) Hernández-Pagán, E. A.; Lord, R. W.; Veglak, J. M.; Schaak, R. E.; Incorporation of Metal Phosphide Domains into Colloidal Hybrid Nanoparticles. *Inorg. Chem.* **2021**, *60*, 4278–4290.

(39) Balakrishnan, S. K.; Kamat, P. V. Au-$CsPbBr_3$ Hybrid Architecture: Anchoring Gold Nanoparticles on Cubic Perovskite Nanocrystals. *ACS Energy Lett.* **2017**, *2*, 88– 93.

(40) Wang, C.; Daimon, H.; Sun, S. Dumbbell-like Pt–Fe_3O_4 Nanoparticles and Their Enhanced Catalysis for Oxygen Reduction Reaction. *Nano Lett.* **2009**, *9*, 1493–1496.

(41) Huang, X.; Neretina, S.; El-Sayed, M. A. Gold Nanorods: From Synthesis and Properties to Biological and Biomedical Applications. *Adv. Mater.* **2009**, *21*, 4880–4910.

(42) Costi, R.; Saunders, A. E.; Elmalem, E.; Salant, A.; Banin, U. Visible Light-Induced Charge Retention and Photocatalysis with Hybrid CdSe–Au Nanodumbbells. *Nano Lett.* **2008**, *8*, 637–641.

(43) Mokari, T.; Rothenberg, E.; Popov, I.; Costi, R.; Banin, U. Selective Growth of Metal Tips onto Semiconductor Quantum Rods and Tetrapods. *Science* **2004**, *304*, 1787–1790.

(44) Hodges, J. M.; Morse, J. R.; Williams, M. E.; Schaak, R. E. Microscopic Investigation of Chemoselectivity in Ag–Pt–Fe_3O_4 Heterotrimer Formation: Mechanistic Insights and Implications for Controlling High-Order Hybrid Nanoparticle Morphology. *J. Am. Chem. Soc.* **2015**, *137*, 15493–15500.

(45) Saunders, A.E.; Popov, I.; Banin, U. Synthesis of Hybrid CdS–Au Colloidal Nanostructures. *J. Phys. Chem. B* **2006**, *110*, 25421–25429.

(46) De. Trizio, L.; Manna, L. Forging Colloidal Nanostructures via Cation Exchange Reactions. *Chem. Rev.* **2016**, *116*, 10852–10887.

(47) Fenton, J. L.; Steimle, B. C.; Schaak, R. E. "Tunable Intraparticle Frameworks for Creating Complex Heterostructured Nanoparticle Libraries," *Science* **2018**, *360*, 513-517.

(48) Pearson, R. G. Absolute Electronegativity and Hardness: Application to Inorganic Chemistry. *Inorg. Chem.* **1988**, *27*, 734–740.

(49) Lesnyak, V.; Brescia, R.; Messina, G. C.; Manna, L. Cu Vacancies Boost Cation Exchange Reactions in Copper Selenide Nanocrystals. *J. Am. Chem. Soc.* **2015**, *137*, 9315–9323.

(50) Bai, B.; Xu, M.; Li, N.; Chen, W.; Liu, J.; Liu, J.; Rong, H.; Fenske, D.; Zhang, J. Semiconductor Nanocrystal Engineering by Applying Thiol- and Solvent-Coordinated Cation Exchange Kinetics. *Angew. Chem., Int. Ed.* **2018**, *58*, 4852–4857.

(51) Fenton, J. L.; Steimle, B. C.; Schaak, R. E. Structure-Selective Synthesis of Wurtzite and Zincblende ZnS, CdS, and $CuInS_2$ Using Nanoparticle Cation Exchange Reactions. *Inorg. Chem.* **2019**, *58*, 672–678.

(52) Gariano, G.; Lesnyak, V.; Brescia, R.; Bertoni, G.; Dang, Z.; Gaspari, R.; De Trizio, L.; Manna, L. Role of the Crystal Structure in Cation Exchange Reactions Involving Colloidal Cu_2Se Nanocrystals. *J. Am. Chem. Soc.* **2017**, *139*, 9583– 9590.

Chapter 2

Seeded Growth of Metal Nitrides on Noble-Metal Nanoparticles to Form Complex Nanoscale Heterostructures

2.1 Introduction

Colloidal heterostructured nanoparticles that integrate multiple materials through solid–solid interfaces are foundational components of applications as diverse as catalysis, plasmonics, solar energy conversion, magnetism, theranostics, and biomedical imaging.[1–12] While each constituent material in a multicomponent nanoparticle has a function, the heterointerfaces permit electronic coupling and enable the emergence of synergistic properties that the individual particles cannot achieve on their own. For example, heterostructured Fe_3O_4–CdS@Au nanoparticles exhibit enhanced photothermic-catalytic activity for water reduction, and core–shell fct-PdFe@Pd nanoparticles supported on graphene function as highly efficient catalysts for the oxygen reduction reaction (ORR).[10,13] The development of methods to synthesize colloidal heterostructured nanoparticles must consider the chemistry needed to form the desired materials, the compatibility of chemical reagents and reaction conditions with other materials that are present, and the ability to form a stable interface. Seeded growth methods, where one material grows off another in solution, have been used to synthesize constructs.[4,5,14,15] Nanoparticle coupling reactions, phase segregation reactions, and partial cation exchange reactions provide additional pathways to colloidal heterostructured nanoparticles.[4,16–18] However, despite these and other approaches, the diversity of materials that can be incorporated into colloidal heterostructured nanoparticles remains limited predominantly to metals, metal alloys, metal oxides, metal chalcogenides, and metal halide perovskites.[5,7,12,13,19–21] Other important classes of materials remain inconspicuously absent.

Among the classes of materials that have not yet been incorporated into colloidal heterostructured nanoparticles are metal nitrides, which are important for a variety of applications that include catalysis, electrooptics, and energy conversion and storage.[22–25] Metal nitrides are notoriously difficult to synthesize as colloidal nanoparticles because the most readily available nitrogen sources, including ammonia, amides, and N_2, are not generally reactive at the maximum temperatures that can be achieved in the solvents that are typically used in nanoparticle synthesis.[23,26–28] Of the few metal nitride nanoparticles that have been made colloidally, Cu_3N and Cu_3PdN are ideal material components to incorporate into heterostructured nanoparticles. Both of these materials are readily accessible at moderate temperatures in solution.[28] It has been reported that the use of nitrate salts helps to facilitate the formation of the metal nitrides when synthesized in the presence of alkylamines[29] and also that ammonia may be evolved through the reduction of an alkyl imine formed insitu.[30] Additionally, key reagents used to synthesize these materials, including oleylamine and 1-octadecene, are common to other nanoparticle systems, which ensures chemical compatibility with other nanoparticles already present in solution and allows seeded growth to occur. Cu_3N and Cu_3PdN, which have been identified as useful nonplatinum catalysts for the ORR in alkaline media, are also valuable targets to incorporate into heterostructured nanoparticles, which contain interfaces that can modulate catalytic properties.[22,28]

Here, we show that the colloidal metal nitrides Cu_3N and Cu_3PdN can be grown on Pt and Au nanoparticle seeds to form a diverse range of nanoscale heterostructures. Cu_3PdN grows on faceted Pt seed through the in situ deposition of a Cu-rich intermediate followed by the incorporation of Pd and N at the corners. In contrast, the growth of Cu_3n on Pt appears more sluggish and indiscriminate. These observations reveal a synthetic pathway for achieving the regioselective deposition of metal nitrides onto noble-metal nanoparticle seeds. These insights can be applied to the rational design of more complex multicomponent heterostructures such as Fe_3O_4–Pt–Cu_3PdN. In addition to serving as instructive metal nitride–noble-metal model systems that

provide important insights into the seeded growth pathway, these heterostructures integrate various catalytic and plasmonic nanomaterials and therefore may serve as future platforms for constructing multifunctional hybrid constructs.

2.2 Experimental Section

2.2.1 Chemicals and Materials

Copper(II) nitrate trihydrate [$Cu(NO_3)_3 \cdot 3H_2O$, >99%], gold(III) chloride hydrate [$HAuCl_4 \cdot xH_2O$, 99.995%], platinum(II) acetylacetonate [$Pt(acac)_2$, 97%], iron(0) pentacarbonyl [$Fe(CO)_5$, >99.99%], iron(III) acetylacetonate [$Fe(acac)_3$ 99.7%], borane *tert*-butylamine complex (BTB, 97%), benzyl ether (98%), oleic acid (OLAC, 90%, technical grade), oleylamine (OLAM, 70%, technical grade_, and 1-octadecene (ODE, 90%, technical grade) were purchased from Sigma-Aldrich. Palladium(II) acetylacetonate [$Pd(acac)_2$, 99%] was purchased from Strem Chemicals. Solvents (hexanes, toluene, ethanol, and acetone) were of analytical grade. All chemicals were used as received without further purification.

2.2.2 General Safety Considerations

It should be noted that as with all metal nanoparticle reactions synthesized at elevated temperatures in high boiling point solvents, it is important to ensure safety through proper training and chemical handling, implementation of procedures and techniques, and careful monitoring of in-progress reactions. These reactions involve corrosive chemicals, heated flammable liquids that must be kept under air-free conditions, various redox reactions, and gas evolution that can cause bumping, including water vapor and CO from $Fe(CO)_5$.

2.2.3 Synthesis of 8 nm Cube-Shaped Pt Nanoparticles

Using a modification of a reported procedure, 100 mg (0.25 mmol) of $Pt(acac)_2$, 10 mL of ODE, 1 mL of OLAM, and 1 mL of OLAC were added to a three-necked, 50 mL round-bottom flask equipped with a magnetic stir bar, a reflux condenser, a thermometer, and a rubber septum.[31]

The mixture was placed under vacuum and degassed at 120 °C for 30 min. the reaction mixture was then placed under an Ar blanket. In an Ar-filled glovebox, a solution of 15 μL of $Fe(CO)_5$ in 1 mL of benzyl ether was added to a 20 mL septum-capped vial. The Fe precursor solution was then injected by syringe into the main reaction mixture. The reaction vessel was then heated to 190 °C (at a rate of 5–10 °C/min). The reaction mixture was aged at 190 °C for 1 h, and then the reaction vessel was removed from the heating mantle and allowed to cool down to room temperature. The formed particles were precipitated by ethanol and collected by centrifugation. The particles were redispersed in hexanes, precipitated by adding ethanol, and centrifuged again. The collected particles were dispersed in hexanes, precipitated by adding ethanol, and centrifuged again. The collected particles were dispersed in hexanes and stored for further use.

2.2.4 Synthesis of 6 nm Multifaceted Pt Nanoparticles

The procedure to synthesize the 6 nm multifaceted Pt particles was the same as that described above to synthesize the 8 nm cube-shaped Pt nanoparticles, except that after degassing at 120 °C for 30 min and placing the reaction mixture under an Ar blanket, the reaction mixture was additionally heated to 180 °C before injecting $Fe(CO)_5$.

2.2.5 Synthesis of 7 nm Au Nanoparticles

Using a modification of a reported procedure, 100 mg (0.29 mmol) of $HAuCl_4 \cdot xH_2O$, 10 mL of OLAM, and 10 mL of toluene were loaded into a 40 mL vial with a magnetic stir bar.[32] The mixture was stirred, open to air, for approx. 5 min. A solution of 50 mg (0.57 mmol) of BTB in 2 mL of a 1:1 (v/v) mixture of OLAM and toluene was added to the gold solution. The reaction mixture was aged at room temperature for 1 h. The formed particles were precipitated by ethanol and collected by centrifugation. The particles were dispersed in hexanes, precipitated by adding ethanol, and centrifuged again. The collected particles were dispersed in hexanes and stored for further use.

2.2.6 Synthesis of M–Cu_3PdN (M = Pt, Au) Heterostructured Nanoparticles

Using a modification of a reported procedure, 60 mg (0.25 mmol) of $Cu(NO_3)_2 \cdot 3H_2O$, 25 mg of $Pd(acac)_2$, 7.5 mL of ODE, 2.5 mL of OLAM, and 10 mg of metal nanoparticles were added to a three-necked, 50 mL round-bottom flask equipped with a reflux condenser, a thermometer adapter, a thermometer, a rubber septum, and a magnetic stir bar.[28] The reaction mixture was placed under vacuum and degassed at 120 °C for 1 h. The solution was then placed under an Ar blanket and heated to 190 °C (at a rate of 5–10 °C/min). The solution was aged at 190 °C for 30 min, and then the reaction vessel was removed from the heating mantle and allowed to cool down to room temperature. The formed particles were precipitated with ethanol and then collected by centrifugation. The particles were redispersed in hexanes, precipitated by adding ethanol, and centrifuged again. The collected particles were dispersed in hexanes and stored for further characterization.

2.2.7 Synthesis of Pt–Fe_3O_4 Hybrid Nanoparticles

Using a modification of a reported procedure, 50 mg (0.14 mmol) of $Fe(acac)_3$, 4 mL of OLAC, 6 mL of OLAM, and 5 mg of Pt nanoparticle seeds were added to a three-necked, 50 mL round-bottom flask equipped with a reflux condenser, a thermometer adapter, a thermocouple, a rubber septum, and a magnetic stir bar.[33] The reaction mixture was placed under vacuum and degassed at 120 °C for 30 min. The solution was then placed under an Ar blanket, heated to 310 °C, and reacted at this temperature for 30 min. The reaction vessel was removed from the heating mantle and allowed to cool to 60 °C. The formed particles were precipitated with ethanol and then collected by centrifugation. The particles were redispersed in hexanes, precipitated by adding ethanol, and centrifuged again. The collected particles were dispersed in hexanes and stored for further characterization.

2.2.8 Synthesis of Cu_3PdN–Pt–Fe_3O_4 Heterotrimer Nanoparticles

The reaction conditions were the same as for the synthesis of Pt–Cu_3PdN heterostructured nanoparticles except for using 12 mg of the Pt–Fe_3O_4 hybrid nanoparticles as seeds and reaction time and temperature of 15 min at 170 °C.

2.2.9 Material Characterization

Transmission electron microscopy (TEM) images were collected on a JEOL 1200 EX II microscope operating at 80 kV. High-resolution transmission electron microscopy (HRTEM) images, unless otherwise stated, were collected on an FEI Titan G2 S/TEM equipped with spherical aberration correctors on the image and probe-forming lenses at an accelerating voltage of 200 kV. Unless otherwise indicated, high-angle annular dark-field scanning transmission electron microscopy (STEM-EDS) maps, and selected area electron diffraction (SAED) patterns were collected on an FEI Talos F200X S/TEM at an accelerating voltage of 200 kV. Image J software was used to analyze the SAED and HRTEM images. Bruker ESPIRIT 2 software was used to interpret the STEM-EDS element map data. Powder X-ray diffraction (XRD) data were collected on a Bruker D-8 Advance X-ray diffractometer using Cu Kα radiation. X-ray photoelectron spectra (XPS) were collected on a PHI VersaProbe II spectrometer, equipped with a scanning monochromatic AL Kα X-ray source (hυ = 1486.6 eV) and a concentric hemispherical analyzer. Charge neutralization was performed using both low-energy electrons (<5 eV) and argon ions. The binding energy axis was calibrated using a sputter-cleaned Cu foil (Cu $2p_{3/2}$ = 932.7 eV, Cu $3p_{3/2}$ = 75.1 eV). Survey and high-resolution scans were acquired at pass energies of 117.4 and 29.4 eV, respectively. Peaks were charge-referenced to C 1s at 284.8 eV. Measurements were made at a takeoff angle of 45° with respect to the sample surface plane. This resulted in a typical sampling depth of 3-6 nm (95% of the signal originated from this depth or shallower). Quantification was done using instrumental relative sensitivity factors (RSFs) that account for the X-ray cross section and inelastic mean free path of the electrons.

2.3 Results and Discussion

2.3.1 Deposition of Cu_3N and Cu_3PdN on Pt and Au Nanoparticles

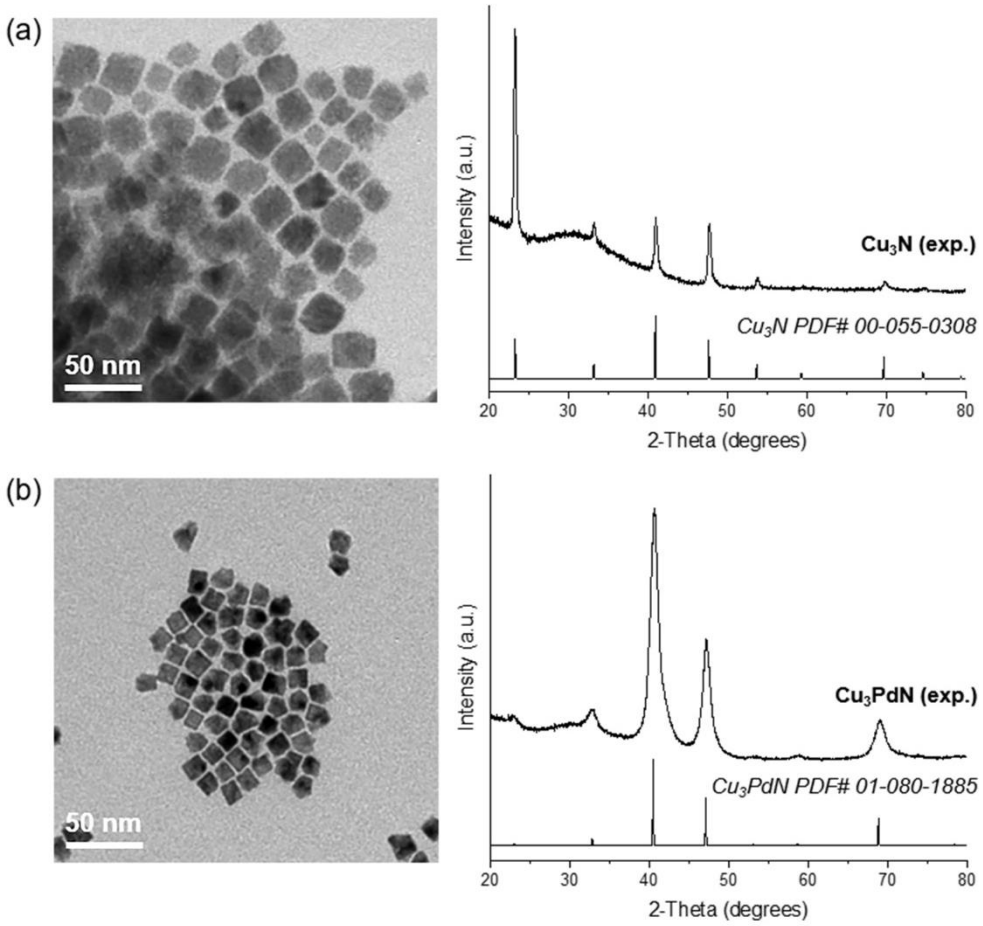

Figure 2.1: TEM images and XRD patterns (experimental and reference) for the synthesis of (a) Cu_3N and (b) Cu_3PdN under the established conditions described in the Experimental Section.

Cu_3N nanoparticles were synthesized by reacting $Cu(NO_3)_2$ in 1-octadecene and oleylamine at 210 °C, and Cu_3PdN nanoparticles were synthesized by reacting $Cu(NO_3)_2$ and $Pd(acac)_2$ in 1-octadecene and oleylamine at 190 °C, as described in detail in the Experimental Section and as confirmed by the TEM and XRD data in Figures 2.1 and 2.2. We then used these same reagents and reaction conditions to attempt to grow Cu_3N and Cu_3PdN in the presence of various types of Pt and Au nanoparticle seeds to produce heterostructured nanoparticles having

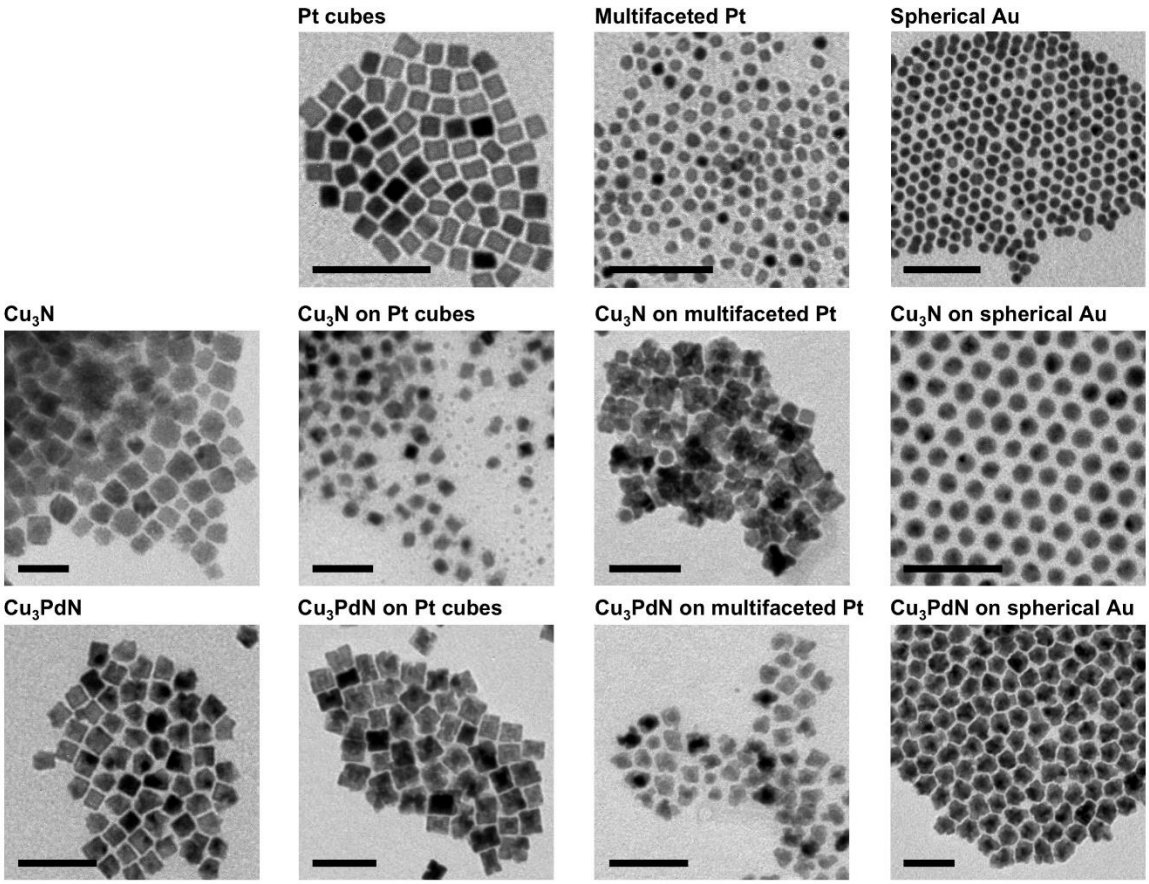

Figure 2.2: TEM image grid showing (top) the various Pt and Au nanoparticle seeds, (left) Cu_3N and Cu_3PdN nanoparticles synthesized directly without noble-metal seeds present, and (other panels) heterostructured nanoparticles formed by growing Cu_3N and Cu_3PdN on the various Pt and Au seeds. All scale bars correspond to 50 nm.

metal nitride–noble-metal interfaces. Figure 2.2 shows TEM images of the three types of Pt and Au nanoparticle seeds: 8 nm cube-shaped Pt particles, 6 nm multifaceted Pt particles, and 7 nm spherical Au particles. Figure 2.2 also shows TEM images of the particles formed after the attempted growth of Cu_3N and Cu_3PdN, using the established conditions mentioned above. The observed morphologies reveal interesting similarities and differences among the various systems. For the spherical Au seeds, Cu_3PdN uniformly covers the Au particle to form core–shell particles. For the multifaceted Pt seeds, a range of heterostructures are observed, including core–shell particles for more spherical Pt seeds and particles having Cu_3PdN localized on the more faceted regions. For the cube-shaped Pt particles, the Cu_3PdN appears to be localized exclusively on the

corners of the Pt nanocubes. The growth behavior of Cu_3N on the various Pt and Au seeds is quite different from that for Cu_3PdN. For all types of Pt seeds, there appears to be little preference to where the Cu_3N grows under established conditions, forming predominantly core–shell structures. Cu_3N was not observed to grow on Au seeds under established conditions. In contrast, XRD data indicate the formation of a AuCu alloy instead of discreet Au and Cu_3N domains (Figures 2.2 and 2.3).

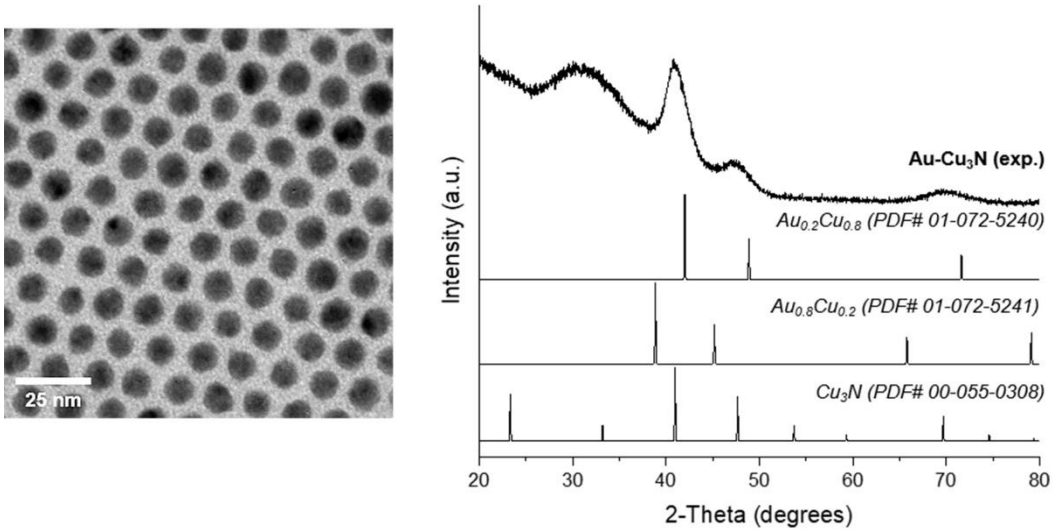

Figure 2.3: (left) TEM image and (right) XRD patterns characterizing the synthesis of Cu_3N on spherical Au seeds under the established conditions described in the Experimental section.

Based on the data in Figure 2.2, where attempts to seed the growth of Cu_3N and Cu_3PdN on various Pt and Au nanoparticles used the reaction conditions that were already established for the synthesis of Cu_3N and Cu_3PdN nanoparticles, two sets of observations are especially notable. First, Cu_3N does not grow on Au seeds under these reaction conditions, favoring alloy formation instead of seeded growth, while Cu_3N growth on Pt occurs indiscriminately to form core–shell particles rather than regioselectively on certain facets. Second, while Cu_3PdN does indeed grow on both the Pt and Au seeds, the morphology of the seeds, and, in particular, the faceting, influences the regions of the particle surface where nitride growth occurs. These results point to differences in the growth pathways for the various systems, as well as the possibility of achieving

regioselectivity during seeded growth and therefore motivate a deeper study of the pathways by which the metal nitrides grow on noble-metal seeds.

2.3.2 Growth Pathway of Cu_3PdN on Pt Nanocubes

The growth of Cu_3PdN on Pt nanocubes provides an instructive model system for elucidating the pathway by which metal nitrides grow regioselectively on noble-metal seeds. To monitor the growth process, samples from three individual reactions, run in parallel under identical conditions, were obtained by quenching (1) when the reaction reached 170 °C (the point at which the solution was observed to darken), (2) when the reaction reached 190 °C (the temperature at

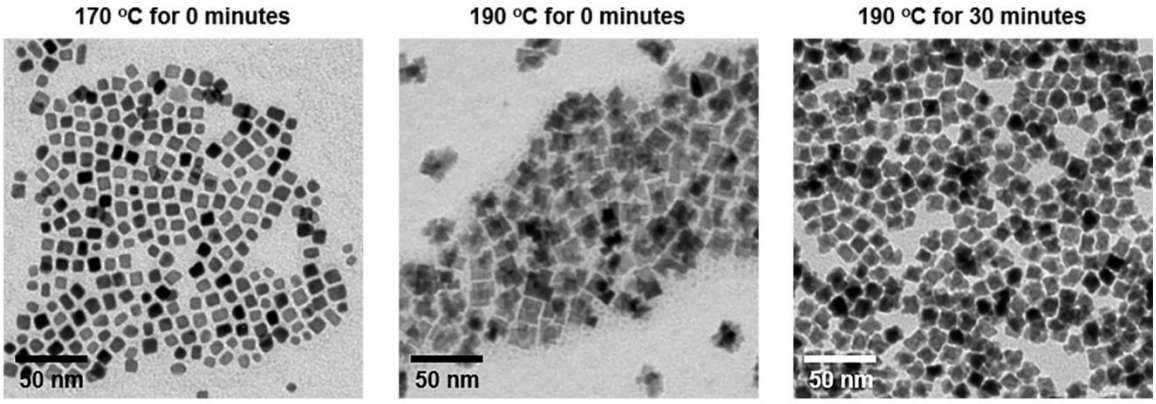

Figure 2.4: TEM images characterizing the growth of Cu_3PdN on Pt nanocubes at different temperatures and reaction times.

which Cu_3PdN forms), and (3) after the reaction was held for 30 min at 190 °C (complete reaction). Figure 2.4 shows TEM images for each sample. At 170 °C, the Pt seeds appear unchanged by TEM, suggesting that seeded growth has not yet occurred. However, at 190 °C, both initially and after 30 min, there is evidence of significant seeded growth, with cube-shaped particles growing off the corners of the Pt nanocubes. This indicates that growth occurs rapidly in the range of 170–190 °C.

To better probe the early stages of growth between 170 and 190 °C, we generated five additional samples by holding the reactions at 170 °C and quenching after 5, 10, 15, 60, and 120 min. Figure 2.5 shows HRTEM, HAADF-STEM, and STEM-EDS data for the 5, 10, and 15 min samples; HAADF-STEM and STEM-EDS data for the 60 and 120 min samples are shown in Figure

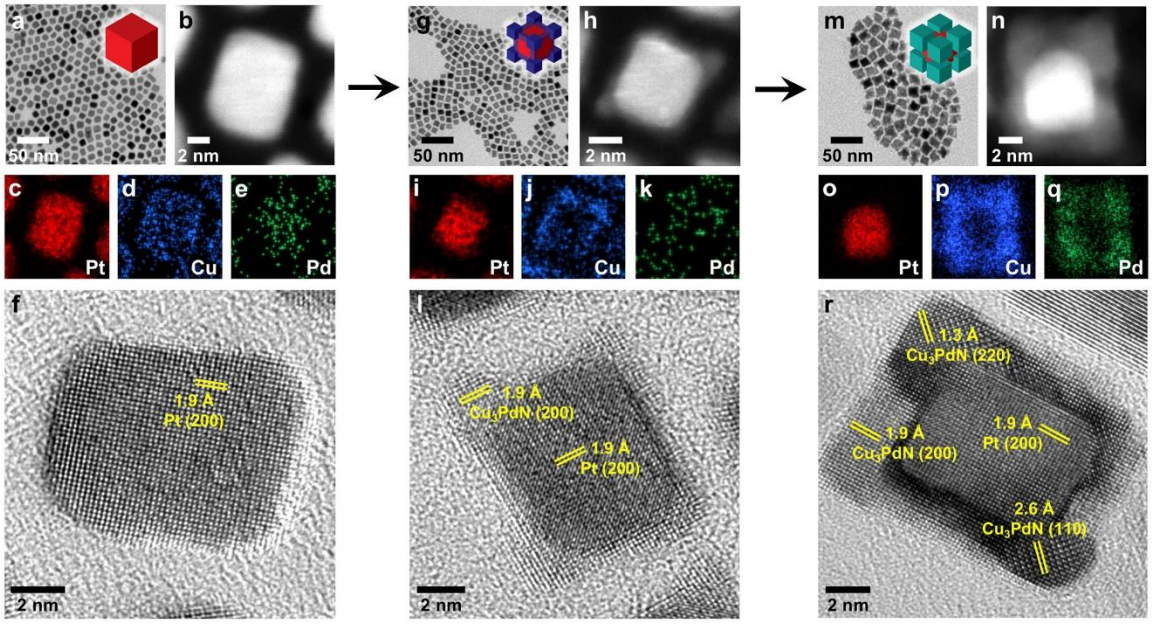

Figure 2.5: Time-dependent growth studies of Cu_3PdN on Pt nanocubes at 170 °C for (a–f) 5 min, (g–l) 10 min, and (m–r) 15 min. The data for each time point include (a, g, and m) TEM images, (b, h, and n) HAADF-STEM images, (c–e, i–k, and o–q) STEM-EDS element maps for Pt (red), Cu (blue), and Pd (green), and (f, l, and r) HRTEM images of individual particles. The STEM-EDS maps correspond to Pt L*α*, Cu K*α*, and Pd L*α*. HAADF-STEM and EDS maps were collected on an FEI Titan G2 S/TEM.

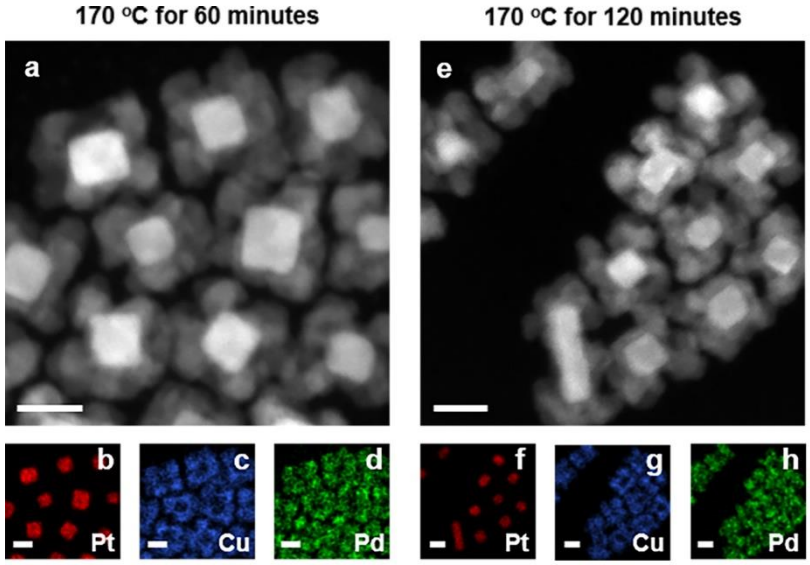

Figure 2.6: Solution annealing of Pt–Cu_3PdN heterostructured nanoparticles at 170 °C for (a–d) 60 minutes and (e–h) 120 minutes. The data for each system include (a,e) HAADF-STEM images and (b–d, f–h) corresponding STEM-EDS maps. The STEM-EDS maps correspond to Pt L*α*, Cu K*α*, and Pd L*α*. All scale bars correspond to 5 nm.

2.6. After 5 min at 170 °C (Figure 2.5a–f), no visible surface deposits are observable

microscopically. However, STEM-EDS element maps indicate that the surface is covered with Cu, which is consistent with the darkening of the solution. No Pd is present in the particles at this stage; the observed signals are near background levels. After 10 min at 170 °C (Figure 2.5g–l), the HRTEM and HAADF-STEM images reveal a lighter-contrast shell surrounding the darker-contrast Pt seeds, and the shell correlates with the Cu signal in the STEM-EDS maps. Interestingly, the Cu is colocalized with a small amount of Pd, in a 9:1 Cu/Pd ratio, although the Pd is predominantly present at the corners of the Pt nanocube seeds while the Cu appears more localized on the edges and corners of the cubes. At this point, Cu has deposited on the Pt seeds and Pd begins localizing at the corners, which are the most reactive regions of the Pt nanocubes where growth apparently is favored. Additionally, Cu is beginning to coalesce on the edges, which is also a highly reactive region of the seed particle surface. After 15 min at 170 °C (Figure 2.5m–r), growth at the corners has increased to a point where an incomplete shell decorates the Pt nanocube seeds. The corresponding STEM-EDS maps show colocalization of Cu and Pd in the 3:1 ratio expected for Cu_3PdN. XRD confirms the presence of both Pt and Cu_3PdN (Figure 2.7). Furthermore, the

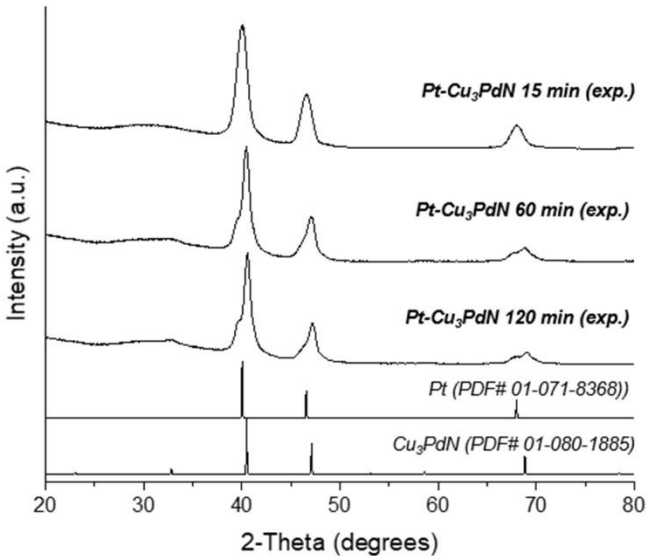

Figure 2.7: XRD patterns for Pt–Cu_3PdN heterostructures annealed for various times in 1-octadecene and oleylamine at 170 °C.

HRTEM image in Figure 2.5r shows lattice fringes on the corner domains with *d*-spacings corresponding to the (110) plane in Cu_3PdN. This *d*-spacing value, which is diagnostic of Cu_3PdN, matches well with the *d*-spacing of Cu_3PdN obtained from the Pt–Cu_3PdN XRD pattern, Figure 2.8. The HRTEM images show that Cu_3PdN and Pt are crystallographically aligned and epitaxial, which is consistent with the closely related lattice constants of Cu_3PdN (a = 3.85 Å) and Pt (a = 3.90 Å). While the presence of an amorphous Cu or CuO_x shell cannot be ruled out, the data are most consistent with the formation of Cu_3PdN.

The 60 and 120 min samples, shown in Figure 2.6, appear to be morphologically indistinguishable from the 15 min samples, indicating that significant additional growth of Cu_3PdN on the Pt seeds does not occur and that the terminal size is reached within 15 min of growth at 170 °C. However, XRD data show an increase in the relative peak intensity, implying an increased

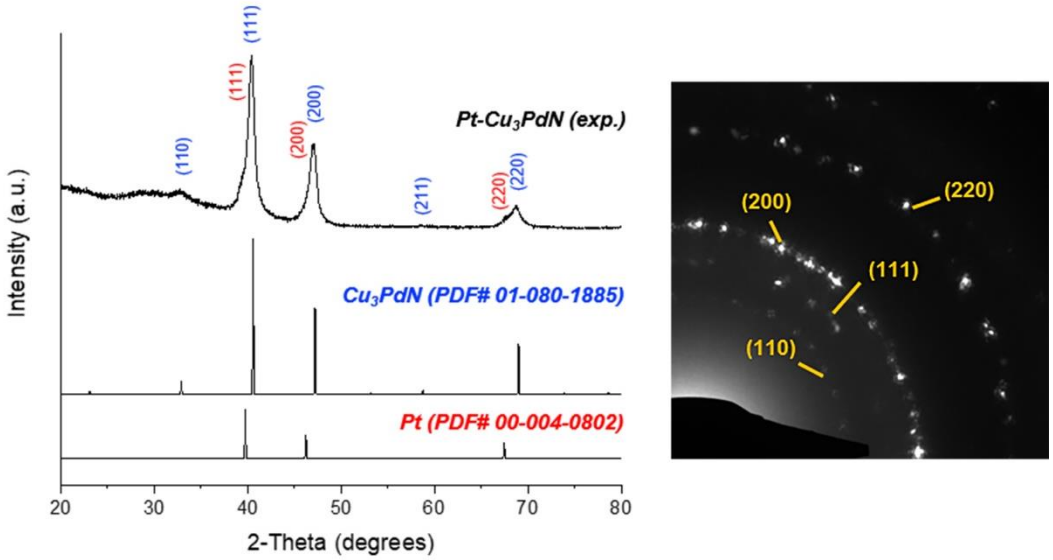

Figure 2.8: XRD and SAED data characterizing the Pt–Cu_3PdN heterostructures formed at 190 °C for 30 minutes. Both Pt and Cu_3PdN are observed in the XRD pattern, and SAED shows a diffraction ring corresponding to the characteristic (110) plane of Cu_3PdN. (Labels on the SAED pattern correspond to Cu_3PdN.)

crystallinity of the Cu_3PdN domains with increasing reaction time (Figure 2.7). This indicates that solution-phase annealing occurs with prolonged heating.

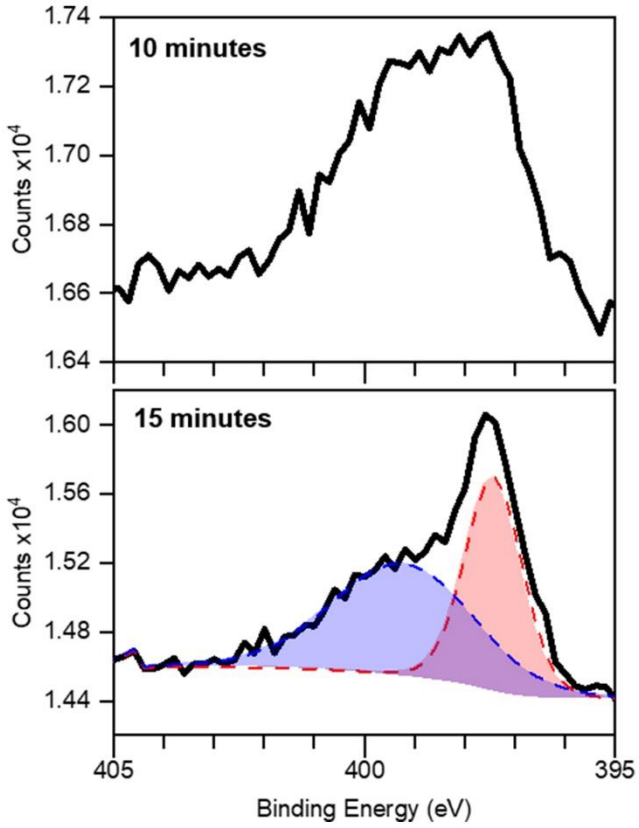

Figure 2.9: XPS spectra for the N 1s region characterizing the growth of Cu_3PdN on Pt nanocubes at 10 and 15 min time points. The deconvolutions in the 15 min sample represent the emission from surface-bound oleylamine (blue) and N bonded to Cu in the Cu_3PdN crystal (red).

XPS provides additional insights into the evolution of the surface species during the seeded growth process. Figure 2.9 and 2.10 show high-resolution XPS spectra of the Pt 4f, Cu 2p, Pd 3d, and N 1s regions for samples where Cu_3PdN growth on Pt was allowed to proceed at 170 °C for 10 and 15 min. Quantification using instrumental relative sensitivity factors (RSFs) reveal 9:1 and 3:1 Cu/Pd ratios for the 10 and 15 min samples, respectively, which matches the Cu/Pd ratios observed by EDS and is also consistent with the microscopic observation that Cu deposits before Pd.

For both the 10 and 15 min samples, the XPS spectra of the N 1s region contain two distinct binding energies (Figure 2.9). The peak at ~397 eV corresponds to the N in Cu_3PdN and the peak at ~399.5 eV corresponds to the N in oleylamine that is adsorbed to the surfaces of the particles.[34]

The N 1s signal for the 15 min sample is more intense than that for the 10 min sample, with a significantly larger signal-to-noise ratio, and this is consistent with a larger amount of nitrogen incorporated into the product, consistent with the formation of Cu_3PdN, as the reaction proceeds. XPS spectra for the Pt 4f region (Figure 2.10) show the expected $4f_{5/2}$ and $4f_{7/2}$ binding energies of 74.5 and 71.2 eV, respectively, which are consistent with metallic Pt.[35] XPS spectra for the Cu 2p region show the $2p_{1/2}$ and the $2p_{3/2}$ binding energies at 952.5 and 932.7 eV, respectively. The Cu 2p

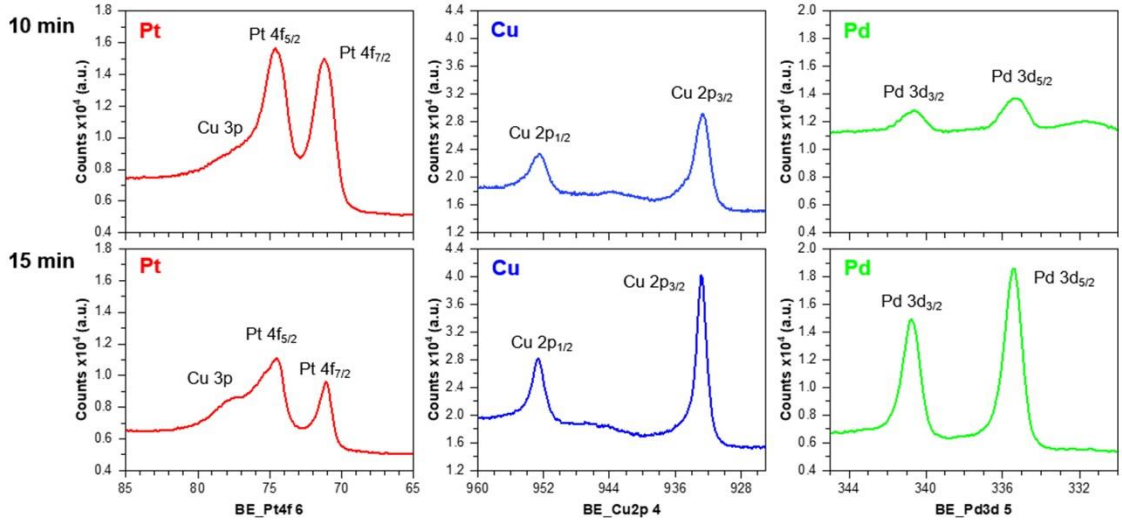

Figure 2.10: XPS analysis of Pt–Cu_3PdN heterostructures synthesized at 170 °C for 10 and 15 min time points, showing the Pt 4f, Cu 2p, and Pd 3d regions. In the Pt 4f region the shoulder centered around ~77 eV corresponds to an overlapping Cu 3p binding energy. The loss of Pt peak intensity and increase in Cu and Pd peak intensities when going from the 10 to 15 min sample is consistent with the overgrowth of Cu_3PdN on the Pt cubes.

binding energies are in good agreement with those expected for Cu–N– bonding in the Cu_3N substructure of Cu_3PdN.[32] The Pd 3d regions for both the 10 and 15 min samples show $3d_{3/2}$ and $3d_{5/2}$ binding energies of 340.7 and 335.4 eV, respectively. The peak at 335.4 eV corresponds well with the Pd–N binding energy that would be expected for the formation of Cu_3PdN, rather than a binding energy of 335.1 eV that would indicate metallic Pd.[34] Taken together, the experiments and data described above provide important insights into the pathway by which Cu_3PdN grows on Pt nanoparticle seeds. Initially, a Cu-containing species deposits on the surface of the Pt seeds. As the reaction proceeds, more Cu is deposited, followed by a slower deposition and incorporation of Pd

onto higher-energy regions of the Pt nanoparticle surface, i.e., corners of cubes or edges of multifaceted particles. Further heating results in the coalescence of the Cu species with concomitant incorporation of deposited Pd, ultimately resulting in the formation and crystallization of Cu_3PdN. For the Pt cubes, this results in the regioselective growth of Cu_3PdN on the corners. Continued heating beyond this point results in solution-phase annealing of the Cu_3PdN domains, which increases their crystallinity but does not result in further growth. The pathway by which Cu_3PdN grows on cube-shaped Pt seeds involves nonselective deposition followed by surface migration and coalescence to a preferred interface. A similar pathway was identified during the growth of Ag on Pt–Fe_3O_4 hybrid nanoparticles.[36] Here, Ag initially deposited on both the Fe_3O_4 and Pt domains. Further heating resulted in the surface migration of the Ag from the Fe_3O_4 domains to the Pt domains followed by coalescence into a larger Ag domain anchored to the Pt surface. It is also known that the morphology of a seed nanocrystal influences the morphology of the resulting heterostructure after seeded growth, due to differences in surface diffusion of deposited atoms, as well as the nature of the particle–particle interface.[37,38]

2.3.3 Growth Pathway of Cu_3N and Pd on Pt Nanocubes

To better understand the role of Pd in facilitating the growth of Cu_3PdN on Pt, and also because Cu_3N and Cu_3PdN were observed to grow differently on Pt (Figure 2.2), we carried out analogous experiments growing Cu_3N and Pd. Figure 2.11 shows TEM images of the particles obtained during the attempted growth of Cu_3N (without Pd) on Pt nanocubes for 30, 60, and 120 min at 170 °C. No surface-seeded growth is observed at 30 and 60 min, but by 120 min, there is evidence of growth. The HAADF-STEM image and STEM-EDS element maps in Figure 2.11 show that the Pt nanocubes are surrounded by a Cu-containing shell, and XRD and SAED data confirm

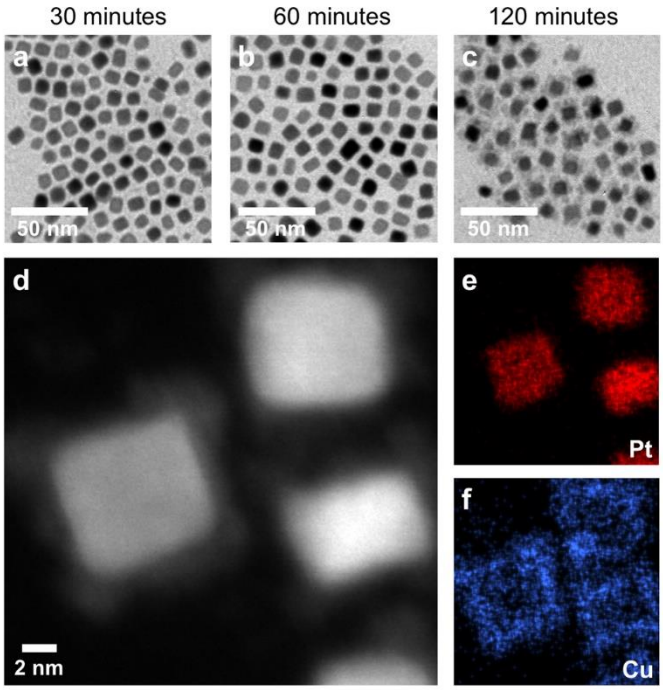

Figure 2.11: (a–c) TEM images characterizing the time-dependent growth of Cu_3N on Pt nanocubes at 170 °C. (d) HAADF-STEM image and corresponding EDS maps for (e) Pt and (f) Cu for the 120 min sample. The STEM-EDS maps correspond to Pt Lα and Cu Kα.

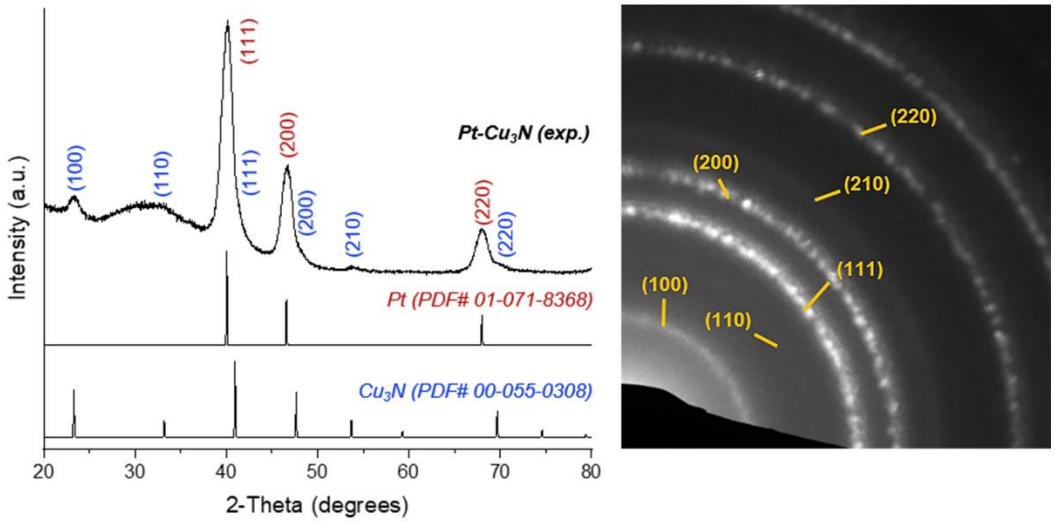

Figure 2.12: XRD and SAED for Pt–Cu_3N heterostructures formed at 170 °C for 120 min. Both Pt and Cu_3N are observed in the XRD pattern, and SAED shows a diffraction ring corresponding to the characteristic (100) plane of Cu_3N. (Labels on the SAED pattern correspond to Cu_3N.)

the presence of both Pt and Cu_3N (Figure 2.12). The data in Figure 2.11 indicate that Cu_3N grows

on both the corners and faces of the Pt nanocubes. This contrasts with the growth of Cu_3PdN, which was almost exclusively localized to the corners of the Pt nanocubes. However, a Cu-rich shell was observed to surround the Pt nanocubes at early time points during the growth of Cu_3PdN (Figure 2.5). This suggests that at early stages of the seeded growth reactions, both Cu_3N and Cu_3PdN grow through a similar pathway, but that Pd plays a role in localizing further growth of Cu_3PdN to the corners of the Pt nanocubes, whereas, for Cu_3N, the growth remains indiscriminate.

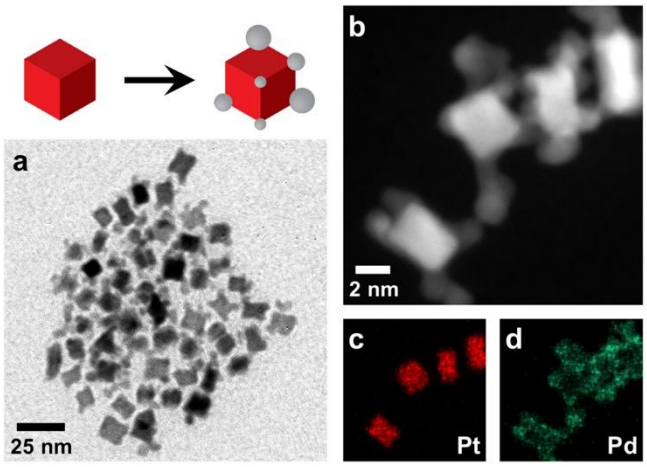

Figure 2.13: (a) TEM image, (b) HAADF-STEM image, and STEM-EDS maps for (c) Pt and (d) Pd corresponding to the growth of Pd on Pt nanocubes. The STEM-EDS maps correspond to Pt Lα and Pd Lα.

TEM, HAADF-STEM, and STEM-EDS images for similar experiments involving the growth of Pd (without Cu_3N) on Pt are shown in Figure 2.13. The growth was carried out for 15 min at 170 °C. The data revealed that Pd grows almost exclusively on the corners of the Pt nanocubes. This further validates the hypothesis that the seeded growth of Cu_3PdN on Pt nanocubes occurs first through Cu_3N growth on the entire Pt surface followed by the selective deposition of Pd at the Pt nanocube corners and finally the incorporation of the Cu_3N into the Pd to form Cu_3PdN.

2.3.4 Growth of Cu_3PdN on Multifaceted Pt and Spherical Au

The studies described above indicate that Cu_3PdN grows predominantly on the corners of Pt nanocubes, driven by the preference of Pd to deposit selectively at the corners during an intermediate step. This suggests that Cu_3PdN deposition on metal nanoparticle seeds that are more faceted or spherical, which do not have well-defined edges or corners, may not occur regioselectively but rather form core–shell structures. To examine this behavior, 6 nm multifaceted Pt nanoparticles were subjected to the same Cu_3PdN growth conditions, as outlined previously. Here, the only difference in the reaction is the initial morphology of the Pt seed particles. As shown in the TEM, HRTEM, HAADF-STEM, and STEM-EDS data in Figure 2.14, the dominant product

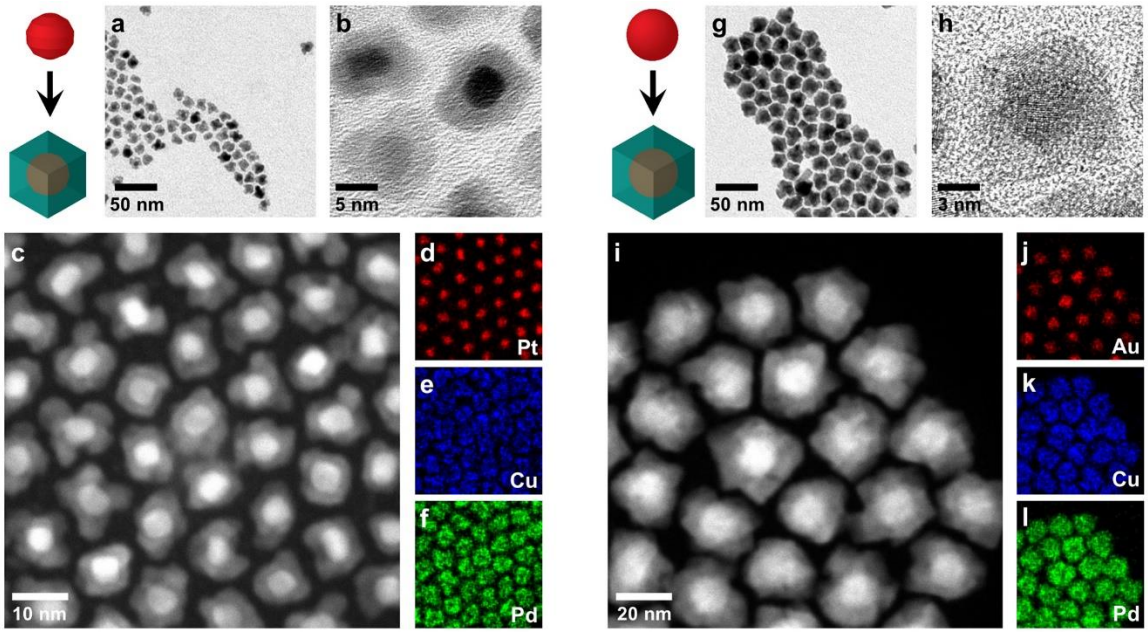

Figure 2.14: Growth studies of Cu_3PdN on (a–f) multifaceted Pt and (g–l) spherical Au. The date for each system includes (a–b, g–h) TEM images, (c, i) HAADF-STEM images, and (d–f, j–l) STEM-EDS maps. The STEM-EDS maps correspond to Pt Lα, Cu Kα, and Pd Lα.

is Pt@Cu_3PdN core@shell particles, with Cu_3PdN completely surrounding the multi-faceted Pt nanoparticle seeds. However, a closer look reveals that the multifaceted Pt seeds span a range of morphologies, including nanocubes, multifaceted particles, and spherical particles, allowing us to discern different growth patterns for different seed morphologies in the same sample and therefore

under identical conditions. The nanocube-shaped seeds exhibit the same corner-localized growth of Cu_3PdN that was observed in Figure 2.5, while the spherical seeds have a continuous shell of Cu_3PdN. Interestingly, the multifaceted Pt seeds show a preference for Cu_3PdN growth at the edges that connect different facets.

The results above confirm that the faceting of seed nanoparticles influences subsequent growth and, consequently, that seed particle faceting can be used to tune the type of heterostructure that forms as a result of Cu_3PdN growth. Consistent with this, Figure 2.14 also shows data for Cu_3PdN growth on spherical Au nanoparticles, which do not exhibit significant faceting. Consistent with the role of faceting in growth location, Cu_3PdN completely surrounds the Au nanoparticles in an exclusive Au@Cu_3PdN core@shell morphology.

2.3.5 Growth of Cu_3PdN on Pt–Fe_3O_4 Heterodimers

The studies described above provide important insights into the pathway by which the ternary metal nitride Cu_3PdN can be controllably integrated into nanoparticle heterostructures. To further expand the complexity of such heterostructures, we applied our knowledge of Cu_3PdN seeded growth to Pt–Fe_3O_4, which is amore complex hybrid nanoparticle seed. Here, the same Pt nanocube seeds used as seeds for growing Cu_3PdN were first used to grow Fe_3O_4, as reported previously.[33] Each resulting Pt–Fe_3O_4 heterodimer has a single domain of Fe_3O_4 that grows on one face of the Pt nanocube. The Fe_3O_4 domain protects one half of the Pt nanocube seed, leaving the other half exposed. We hypothesized, based on the studies above, that Cu_3PdN would grow on the corners of the exposed half of the Pt nanocube seed.

As shown in Figure 2.15, Cu_3PdN does indeed grow on the exposed corners of the Pt domain to form an unusual Fe_3O_4–Pt–Cu_3PdN heterotrimer. The TEM image in Figure 2.15a shows that the majority of the product is Fe_3O_4–Pt–Cu_3PdN, with small subpopulations of Pt-Fe_3O_4 and

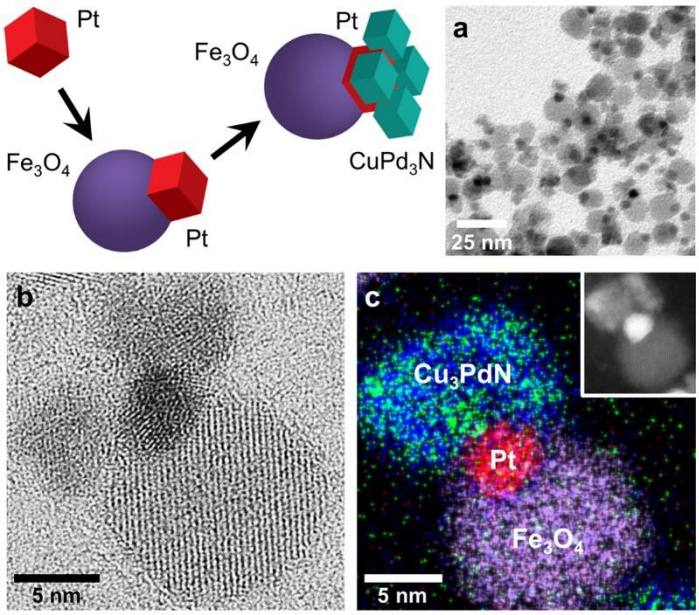

Figure 2.15: (a) TEM image, (b) HRTEM image, and (c) combined STEM-EDS map with corresponding HAADF-STEM image (inset), characterizing the Cu_3PdN–Pt–Fe_3O_4 heterotrimer product formed from growing Cu_3PdN on Pt–Fe_3O_4 heterodimers. The STEM-EDS maps include Pt Lα (red), Cu Kα (blue), Pd Lα (green), and Fe Kα (purple). HAADF-STEM and EDS were collected on an FEI Titan G2 S/TEM.

Pt–Cu_3PdN, which we anticipate could be separated through magnetic and/or thermal fractionation techniques if desired.[39] A representative HRTEM image, shown in Figure 2.15b, indicates that Cu_3PdN grows epitaxially on the corners and edges of the faceted Pt nanoparticle seeds, as expected based on the growth pathway and crystallographic relationships described in the preceding sections. Because of this pathway that favors growth at the corners and edges, multiple distinct Cu_3PdN domains grow on the Pt seeds. The HAADF-STEM image in Figure 2.15c (inset) and corresponding STEM-EDS map in Figures 2.15d and Figure 2.16 further confirms the identities of the Fe_3O_4, Pt, and Cu_3PdN domains. The XRD data in Figure 2.16 confirms that all three components are present and crystalline throughout the bulk sample. Fe_3O_4 is the dominant phase by XRD, which is consistent with its crystallinity, size, and relative phase fraction in the Fe_3O_4–Pt–Cu_3PdN heterotrimers. The peaks for Pt and Cu_3PdN are close together but distinguishable, even within the significantly broadened peaks, based on the peak asymmetry.

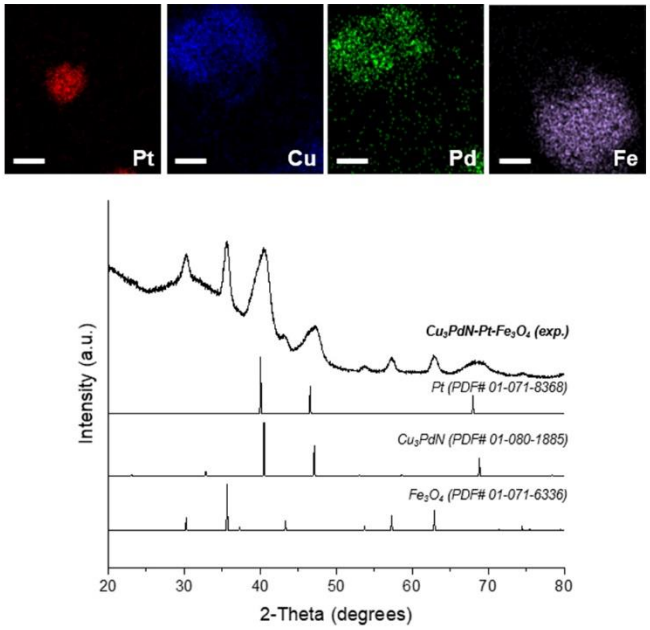

Figure 2.16: (top) STEM-EDS maps and (bottom) XRD pattern for the Fe_3O_4–Pt–Cu_3PdN heterotrimers formed by growing Cu_3PdN on Pt–Fe_3O_4 seeds. The STEM-EDS maps include Pt Lα (red), Cu Kα (blue), Pd Lα (green), and Fe Kα (purple). STEM-EDS maps were collected on an FEI Titan G2 S/TEM.

2.4 Conclusions

We have shown that transition-metal nitrides can be incorporated into colloidal nanoscale heterostructures through seeded growth on noble-metal nanoparticles. We elucidated the pathways by which the model systems Cu_3N and Cu_3PdN grow on Pt and Au seeds and found that the types of nanostructures that form depend on both the morphology of the seed particle and the material being deposited. We found that Cu first deposits indiscriminately over the entire surface of the seed particles. For Cu_3PdN, Pd then deposits at the corners or edges of faceted seed particles, followed by coalescence, growth, and crystallization that ultimately results in the localization of Cu_3PdN to these higher-energy regions of the seed particle surface. When spherical Pt or Au seeds are used instead of cube-shaped or multifaceted particles, Cu_3PdN instead deposits on the entire surface rather than localized in certain regions. For Cu_3N on Pt, nonselective growth occurs as well, as Pd

is not present to localize deposition to corners or facets. For Cu_3N on Au, Cu deposition competes with alloy formation, and we observe that AuCu forms instead of any heterogeneous growth product. Cu_3PdN can also be deposited on multicomponent seeds such as Fe_3O_4–Pt, forming complex Fe_3O_4–Pt–Cu_3PdN heterotrimers. Collectively, these insights provide guidelines for growing transition-metal nitride nanoparticles on noble-metal seeds, for tuning between core@shell and hybrid morphologies and for using secondary metal deposition (e.g., Pd on Pt) to localize metal nitride growth at certain regions of the seed particle surface to achieve regioselective deposition. We anticipate that these pathways may be generalizable to other metal–metal nitride systems and also be useful for developing multifunctional nanostructures that exploit the catalytic and plasmonic properties of the various components.

* This chapter was adapted from Lord, R.W.; Holder, C.F.; Fenton, J.L.; Schaak, R.E. "Seeded Growth of Metal Nitrides on Noble-Metal Nanoparticles to Form Complex Nanoscale Heterostructures," *Chem. Mater.* **2019**, *31*, 4605-4613, with permission.

2.5 Acknowledgements

This work was supported by the U.S. National Science Foundation under grant CH-1707830. TEM imaging was performed in the Penn State Microscopy and Cytometry facility. HRTEM imaging, S/TEM imaging, and EDS mapping were performed at the Materials Characterization Lab of the Penn State Materials Research Institute. The authors thank Dr. Jamie Chen for helpful discussions.

2.6 References

(1) Zhou, M.; Wang, H.; Elnabawy, A. O.; Hood, Z. D.; Chi, M.; Xiao, P.; Zhang, Y.; Mavrikakis, M.; Xia, Y. Facile One-Pot Synthesis of Pd@Pt_{1L} Octahedra with Enhanced Activity and Durability toward Oxygen Reduction. *Chem. Mater.* **2019**, *31*, 1370– 1380.

(2) Xia, X.; Xie, S.; Liu, M.; Peng, H.-C.; Lu, N.; Wang, J.; Kim, M. J.; Xia, Y. On the Role of Surface Diffusion in Determining the Shape or Morphology of Noble-Metal Nanocrystals. *Proc. Natl. Acad. Sci. U.S.A.* **2013**, *110*, 6669– 6673.

(3) Yang, X.; Roling, L. T.; Vara, M.; Elnabawy, A. O.; Zhao, M.; Hood, Z. D.; Bao, S.; Mavrikakis, M.; Xia, Y. Synthesis and Characterization of Pt–Ag Alloy Nanocages with Enhanced Activity and Durability toward Oxygen Reduction. *Nano Lett.* **2016**, *16*, 6644– 6649.

(4) Buck, M. R.; Schaak, R. E. Emerging Strategies for the Total Synthesis of Inorganic Nanostructures. *Angew. Chem., Int. Ed.* **2013**, *52*, 6154– 6178.

(5) Banin, U.; Ben-Shahar, Y.; Vinokurov, K. Hybrid Semiconductor–Metal Nanoparticles: From Architecture to Function. *Chem. Mater.* **2014**, *26*, 97– 110.

(6) Amirav, L.; Alivisatos, A. P. Photocatalytic Hydrogen Production with Tunable Nanorod Heterostructures. *J. Phys. Chem. Lett.* **2010**, *1*, 1051– 1054.

(7) Cathcart, N.; Murshid, N.; Campbell, P.; Kitaev, V. Selective Plasmonic Sensing and Highly Ordered Metallodielectrics via Encapsulation of Plasmonic Metal Nanoparticles with Metal Oxides. *ACS Appl. Nano Mater.* **2018**, *1*, 6514– 6524.

(8) Deka, K.; Guleria, A.; Kumar, D.; Biswas, J.; Lodha, S.; Kaushik, S. D.; Choudhary, S. A.; Dasgupta, S.; Deb, P. Janus Nanoparticles for Contrast Enhancement of T_1–T_2 Dual Mode Magnetic Resonance Imaging. *Dalton Trans.* **2019**, *48*, 1075– 1083.

(9) Fernando, J. F. S.; Shortell, M. P.; Firestein, K. L.; Zhang, C.; Larionov, K. V.; Popov, Z. I.; Sorokin, P. B.; Bourgeois, L.; Waclawik, E. R.; Golberg, D. V. Photocatalysis with Pt–Au–ZnO and Au–ZnO Hybrids: Effect of Charge Accumulation and Discharge Properties of Metal Nanoparticles. *Langmuir* **2018**, *34*, 7334– 7345.

(10) Pang, F.; Zhang, R.; Lan, D.; Ge, J. Synthesis of Magnetite–Semiconductor–Metal Trimer Nanoparticles through Functional Modular Assembly: A Magnetically Separable Photocatalyst with Photothermic Enhancement for Water Reduction. *ACS Appl. Mater. Interfaces* **2018**, *10*, 4929– 4936.

(11) Oh, N.; Kim, B. H.; Cho, S.-Y.; Nam, S.; Rogers, S. P.; Jiang, Y.; Flanagan, J. C.; Zhai, Y.; Kim, J.-H.; Lee, J. Yu, Y.; Cho, Y.H.; Hur, G.; Zhang, J.; Trefonas, P.; Rogers, J.A.; Shim, M. Double-Heterojunction Nanorod Light-Responsive LEDs for Display Applications. *Science* **2017**, *355*, 616– 619.

(12) Gordon, T. R.; Schaak, R. E. Synthesis of Hybrid Au-In_2O_3 Nanoparticles Exhibiting Dual Plasmonic Resonance. *Chem. Mater.* **2014**, *26*, 5900– 5904.

(13) Maiti, K.; Balamurugan, J.; Peera, S. G.; Kim, N. H.; Lee, J. H. Highly Active and Durable Core–Shell Fct-PdFe@Pd Nanoparticles Encapsulated NG as an Efficient Catalyst for Oxygen Reduction Reaction. *ACS Appl. Mater. Interfaces* **2018**, *10*, 18734– 18745.

(14) Gilroy, K. D.; Ruditskiy, A.; Peng, H.-C.; Qin, D.; Xia, Y. Bimetallic Nanocrystals: Syntheses, Properties, and Applications. *Chem. Rev.* **2016**, *116*, 10414– 10472.

(15) Habas, S. E.; Lee, H.; Radmilovic, V.; Somorjai, G. A.; Yang, P. Shaping Binary Metal Nanocrystals through Epitaxial Seeded Growth. *Nat. Mater.* **2007**, *6*, 692– 697.

(16) Motl, N. E.; Bondi, J. F.; Schaak, R. E. Synthesis of Colloidal Au–Cu_2S Heterodimers via Chemically Triggered Phase Segregation of AuCu Nanoparticles. *Chem. Mater.* **2012**, *24*, 1552– 1554.

(17) Fenton, J. L.; Steimle, B. C.; Schaak, R. E. Tunable Intraparticle Frameworks for Creating Complex Heterostructured Nanoparticle Libraries. *Science* **2018**, *360*, 513– 517.

(18) Fenton, J. L.; Hodges, J. M.; Schaak, R. E. Synthetic Deconvolution of Interfaces and Materials Components in Hybrid Nanoparticles. *Chem. Mater.* **2017**, *29*, 6168– 6177.

(19) Buck, M. R.; Bondi, J. F.; Schaak, R. E. A Total-Synthesis Framework for the Construction of High-Order Colloidal Hybrid Nanoparticles. *Nat. Chem.* **2012**, *4*, 37– 44.

(20) Roman, B. J.; Otto, J.; Galik, C.; Downing, R.; Sheldon, M. Au Exchange or Au Deposition: Dual Reaction Pathways in Au–$CsPbBr_3$ Heterostructure Nanoparticles. *Nano Lett.* **2017**, *17*, 5561– 5566.

(21) Hernández-Pagán, E. A.; Leach, A. D. P.; Rhodes, J. M.; Sarkar, S.; Macdonald, J. E. A Synthetic Exploration of Metal–Semiconductor Hybrid Particles of $CuInS_2$. *Chem. Mater.* **2015**, *27*, 7969– 7976.

(22) Wu, H.; Chen, W. Copper Nitride Nanocubes: Size-Controlled Synthesis and Application as Cathode Catalyst in Alkaline Fuel Cells. *J. Am. Chem. Soc.* **2011**, *133*, 15236– 15239.

(23) Abeysinghe, D.; Skrabalak, S. E. Toward Shape-Controlled Metal Oxynitride and Nitride Particles for Solar Energy Applications. *ACS Energy Lett.* **2018**, *3*, 1331– 1344.

(24) Balogun, M.-S.; Qiu, W.; Wang, W.; Fang, P.; Lu, X.; Tong, Y. Recent Advances in Metal Nitrides as High-Performance Electrode Materials for Energy Storage Devices. *J. Mater. Chem. A* **2015**, *3*, 1364– 1387.

(25) Chaudhuri, K.; Shaltout, A.; Shah, D.; Guler, U.; Dutta, A.; Shalaev, V. M.; Boltasseva, A. Photonic Spin Hall Effect in Robust Phase Gradient Metasurfaces Utilizing Transition Metal Nitrides. *ACS Photonics* **2019**, *6*, 99– 106.

(26) Chen, Y.; Landes, N. T.; Little, D. J.; Beaulac, R. Conversion Mechanism of Soluble Alkylamide Precursors for the Synthesis of Colloidal Nitride Nanomaterials. *J. Am. Chem. Soc.* **2018**, *140*, 10421– 10424.

(27) Egeberg, A.; Warmuth, L.; Riegsinger, S.; Gerthsen, D.; Feldmann, C. Pyridine-Based Low-Temperature Synthesis of CoN, Ni_3N and Cu_3N Nanoparticles. *Chem. Commun.* **2018**, *54*, 9957– 9960.

(28) Vaughn, D. D., II; Araujo, J.; Meduri, P.; Callejas, J. F.; Hickner, M. A.; Schaak, R. E. Solution Synthesis of Cu_3PdN Nanocrystals as Ternary Metal Nitride Electrocatalysts for the Oxygen Reduction Reaction. *Chem. Mater.* **2014**, *26*, 6226– 6232.

(29) Sithole, R. K.; Machogo, L. F. E.; Airo, M. A.; Gqoba, S. S.; Moloto, M. J.; Shumula, P.; Van Wyk, J.; Moloto, N. Synthesis and Characterization of Cu_3N Nanoparticles Using pyrrole-2-carbaldpropyliminato Cu(II) complex and $Cu(NO_3)_2$ as Single-Source Precursors: the Search for an Ideal Precursor. *New J. Chem.* **2018**, *42*, 3042– 3049.

(30) Deshmukh, R.; Zeng, G.; Tervoort, E.; Staniuk, M.; Wood, D.; Niederberger, M. Ultrasmall Cu_3N Nanoparticles: Surfactant-Free Solution-Phase Synthesis, Nitridation Mechanism, and Application for Lithium Storage. *Chem. Mater.* **2015**, *27*, 8282– 8288.

(31) Wang, C.; Daimon, H.; Onodera, T.; Koda, T.; Sun, S. A General Approach to the Size- and Shape-Controlled Synthesis of Platinum Nanoparticles and Their Catalytic Reduction of Oxygen. *Angew. Chem., Int. Ed.* **2008**, *47*, 3588– 3591.

(32) Peng, S.; Lee, Y.; Wang, C.; Yin, H.; Dai, S.; Sun, S. A Facile Synthesis of Monodisperse Au Nanoparticles and Their Catalysis of CO Oxidation. *Nano Res.* **2008**, *1*, 229– 234.

(33) Hodges, J. M.; Morse, J. R.; Fenton, J. L.; Ackerman, J. D.; Alameda, L. T.; Schaak, R. E. Insights into the Seeded-Growth Synthesis of Colloidal Hybrid Nanoparticles. *Chem. Mater.* **2017**, *29*, 106– 119.

(34) Ji, A. L.; Lu, N. P.; Gao, L.; Zhang, W. B.; Liao, L. G.; Cao, Z. X. Electrical Properties and Thermal Stability of Pd-Doped Copper Nitride Films. *J. Appl. Phys.* **2013**, *113*, 043705.

(35) Shyu, J. Z.; Otto, K. Identification of Platinum Phases on γ-Alumina by XPS. *Appl. Surf. Sci.* **1988**, *32*, 246– 252.

(36) Hodges, J. M.; Morse, J. R.; Williams, M. E.; Schaak, R. E. Microscopic Investigation of Chemoselectivity in Ag-Pt-Fe_3O_4 Heterotrimer Formation: Mechanistic Insights and Implications for Controlling High-Order Hybrid Nanoparticle Morphology. *J. Am. Chem. Soc.* **2015**, *137*, 15493– 15500.

(37) Weiner, R. G.; Kunz, M. R.; Skrabalak, S. E. Seeding a New Kind of Garden: Synthesis of Architecturally Defined Multimetallic Nanostructures by Seed-Mediated Co-Reduction. *Acc. Chem. Res.* **2015**, *48*, 2688– 2695.

(38) Chen, A. N.; Scanlan, M. M.; Skrabalak, S. E. Surface Passivation and Supersaturation: Strategies for Regioselective Deposition in Seeded Synthesis. *ACS Nano* **2017**, *11*, 12624– 12631.

(39) Smith, W. C.; Morse, J. R.; Bria, C. R. M.; Schaak, R. E.; Williams, S. K. R. Composition-Based Separation of Pt–Fe_3O_4 Hybrid Nanoparticles by Thermal Field-Flow Fractionation. *ACS Appl. Nano Mater.* **2018**, *1*, 6435– 6443.

Chapter 3

Colloidal Nanoparticles of a Metastable Copper Selenide Phase with Near-Infrared Plasmon Resonance

3.1 Introduction

Copper selenide nanoparticles have emerged as important materials having numerous applications, including in plasmonics, photovoltaics, batteries, and catalysis.[1–4] Copper selenide phases span a wide range of compositions and crystal systems, including cubic $Cu_{2-x}Se$, tetragonal Cu_3Se_2, orthorhombic $CuSe_2$, hexagonal CuSe, hexagonal Cu_2Se, and monoclinic $Cu_{2-x}Se$.[5–7] The $Cu_{2-x}Se$ phases are particularly interesting as superionic conductors, thermoelectric materials, electrocatalytic materials, and plasmonic materials.[8–11] Cubic $Cu_{2-x}Se$ (berzelianite), which is one of the most studied copper selenide phases, can adopt a range of stoichiometries, with $x = 0$ through 0.25.[12] This variable composition results in tuning of the plasmon absorption band from 1100 to 1700 nm.[13]

Both the compositions and crystal structures of copper selenide nanoparticles influence and control their properties. Because of this, various chemical strategies have been developed to synthesize them. Most solution-based synthetic routes to colloidal copper selenide nanoparticles have required the use of selenium reagents that require high temperatures to decompose, such as the complex formed with trioctylphosphine (TOP-Se).[14–16] The high-temperature decomposition reactions favor the formation of the most thermodynamically stable copper selenide phases.[17] Diorganyl dichalcogenides have emerged as alternative selenium reagents that decompose at lower temperatures and therefore allow for the synthesis of new and metastable copper chalcogenides.[18]

For example, didodecyl diselenide was used to synthesize wurtzite-related $Cu_{2-x}Se$ nanoparticles, and dibenzyl diselenide and diphenyl diselenide were used to tune between the thermodynamically preferred chalcopyrite and the metastable wurtzite $CuInSe_2$ polymorphs, respectively.[17, 19]

Here, we report the synthesis of a previously unobserved phase of $Cu_{2-x}Se$ as colloidal nanoparticles using diphenyl diselenide as the selenium reagent. This metastable phase is structurally related to weissite $Cu_{1.78}Te$, an experimentally known phase of copper telluride that has been computationally shown to adopt a layered structure characterized by alternating Cu-rich and Cu-deficient layers sandwiching distorted hexagonal Se layers. The weissite-like $Cu_{2-x}Se$ nanoparticles exhibit a broad near-infrared plasmon band localized around 1550 nm, which remains relatively unchanged under various oxidizing and reducing conditions. This adds to the growing number of plasmonic copper chalcogenide nanoparticles.

3.2 Experimental Section

3.2.1 Chemicals and Materials

Copper(II) acetylacetonate [$Cu(acac)_2$, 97%], diphenyl diselenide [Ph_2Se_2, 97%], oleylamine (70%, technical grade), oleic acid (90%, technical grade), benzyl ether (98%), and 1-octadecene (90%, technical grade) were purchased from Sigma-Aldrich. Isopropanol, acetone, hexanes, and toluene were purchased from VWR.

3.2.2 General Safety Concerns

The synthetic methods in this report are done under air-free conditions at elevated temperatures using high-boiling-point solvents. As such, care should be taken to ensure proper monitoring and handling. The safety data sheets for all chemicals used in the reactions should be reviewed, and proper personal protective equipment should be used. These reactions have the potential to evolve toxic gases and as such should be handled in a properly functioning fume hood.

3.2.3 Standard Reaction Vessel Setup

Each of the following procedures utilizes a standard Schlenk line setup. Each three-necked, round-bottom flask was equipped with a magnetic stir bar, a reflux condenser, a thermocouple and adapter, and an angled adapter. The temperature was controlled by a JKEM Gemini programmable temperature controller and LabGlass heating mantles.

3.2.4 Typical Synthesis of Copper Selenide Nanoplatelets

Copper selenide nanoparticles were synthesized using a modification to a published procedure.[17] A 50 mL three-necked, round-bottom flask was charged with $Cu(acac)_2$ (65.44 mg, 0.25 mmol), Ph_2Se_2 (40 mg, 0.125 mmol), and oleylamine (10 mL). This gave a green-colored solution from the combination of the $Cu(acac)_2$ (blue) and Ph_2Se_2 (yellow). The reaction mixture was then degassed under vacuum at 70 °C for 30 min and then at 140 °C for an additional 30 min. The reaction vessel was then placed under an Ar blanket. The reaction mixture was then heated to 220 °C causing the reaction solution to turn a light brown color, which darkens upon reaching approximately 180–200 °C. Once the reaction mixture reaches 215 °C, a 3 min timer was started. After 3 min, the solution reached a final temperature of 220 °C. At this point, the reaction vessel was removed from the heating mantle and rapidly cooled using a room-temperature water bath. Once cooled, the particles were collected using centrifugation and a mixture of isopropanol and acetone (1:1) as antisolvent was added to the solution. The particle suspensions were then centrifuged to crash out the particles. The supernatant was discarded, and the particles were resuspended in toluene or hexanes. This process was repeated two more times, and the particles were resuspended in toluene or hexanes for further use. Particle size was determined to be 18 ± 6 nm (2σ, *N*: 250).

3.2.5 Alternative Synthesis of Copper Selenide Nanoplatelets

A 50 mL, three-necked, round-bottom flask was charged with $Cu(acac)_2$ (65.44 mg, 0.25 mmol), Ph_2Se_2 (40 mg, 0.125 mmol), oleylamine (7.5 mL), benzyl ether (2 mL), and oleic acid (0.5

mL). The reaction mixture was then degassed under vacuum at 120 °C for 60 minutes. The reaction vessel was then placed under an Ar blanket. The reaction mixture was then heated to 200 °C and held at that temperature for 30 minutes. After the reaction was completed, the reaction vessel was removed from the heating mantle and rapidly cooled using a room temperature water bath. Once cooled, the particles were collected into centrifuge tubes and a mixture of isopropanol and acetone (1:1) as antisolvents was added to the formed particles. The particle suspensions were then centrifuged to crash out the particles. The supernatant was discarded, and the particles were resuspended in toluene or hexanes. This process was repeated two more times and the particles were resuspended in toluene or hexanes for further use.

3.2.6 Thermal Annealing Studies

A 50 mL three-necked, round-bottom flask was charged with $Cu_{2-x}Se$ nanoparticles (approx. 10 mg) and 1-octadecene (10 mL). The reaction mixture was then degassed under vacuum at 70 °C for 30 min and then at 140 °C for an additional 30 min. The reaction vessel was then placed under an Ar blanket. The reaction mixture was then heated to 250 °C and held at that temperature for 30 min, after which an aliquot was taken using a ground glass syringe and immediately quenched into ice-cold toluene. This aliquot was then worked up in a similar way as the $Cu_{2-x}Se$ synthesis. The remaining reaction mixture was then heated to 280 °C for an additional 30 min. A final aliquot was taken, quenched in ice-cold toluene, and worked up in the same way as the previous aliquot. The collected particles from each aliquot were suspended in hexanes for further characterization.

3.2.7 Materials Characterization

Unless otherwise stated, transmission electron microscopy (TEM) images were collected on an FEI Tecnai G2 20 XTWIN with a LaB_6 filament operating at 200 kV. Unless otherwise stated, high-resolution transmission electron microscopy (HRTEM) images, high-angle annular dark-field scanning transmission electron microscopy (HAADF-STEM) images, STEM energy-dispersive X-

ray spectroscopy (STEM-EDS) element maps, and selected area electron diffraction (SAED) patterns were collected on an FEI Talos F200X Field Emission S/TEM at an accelerating voltage of 200 kV. ImageJ software was used to analyze the SAED and HRTEM images. Bruker ESPIRIT 2 software was used to interpret the STEM-EDS element map data. Powder X-ray diffraction (XRD) data were collected on a Bruker D-8 Advance X-ray diffractometer using Cu Kα radiation and a Lynx Eye detector and a Malvern Panalytical XPert Pro MPD theta–theta diffractometer operating under Cu Kα radiation. Crystal structure and powder diffraction simulations were performed using CrystalMaker and CrystalDiffract from CrystalMaker Software Ltd., Oxford, England. X-ray photoelectron spectra (XPS) were collected on a PHI VersaProbe II spectrometer, equipped with a scanning monochromatic Al Kα X-ray source ($h\nu$ = 1486.6 eV) and a concentric hemispherical analyzer. Charge neutralization was performed using both low-energy electrons (<5 eV) and argon ions. The binding energy axis was calibrated using a sputter-cleaned Cu foil (Cu $2p_{3/2}$ = 932.7 eV, Cu $3p_{3/2}$ = 75.1 eV). Survey and high-resolution scans were acquired at pass energies of 117.4 and 29.4 eV, respectively. Peaks were charge-referenced to C 1s at 284.8 eV. Measurements were made at a takeoff angle of 45° with respect to the sample surface plane. This resulted in a typical sampling depth of 3–6 nm (95% of the signal originated from this depth or shallower). Quantification was done using instrumental relative sensitivity factors (RSFs) that account for the X-ray cross section and inelastic mean free path of the electrons.

3.2.8 Computational Methods

We performed first-principles calculations to investigate the proposed $Cu_{2-x}Se$ structures. The self-consistent field calculations are performed at the Perdew–Burke–Ernzerhof (PBE) semilocal level of density functional theory (DFT) using the projected-augmented wave (PAW) method implemented in the Vienna ab initio simulation package (VASP).[20-23] The kinetic energy cutoff for the plane-wave expansion of the electron density and effective potential was set to 520

eV. Brillouin zones are sampled with a Γ-centered Monkhorst–Pack grid density of 0.04 $Å^{-1}$ using a Gaussian occupation function. The atomic positions and the lattice vectors of the bulk structures were fully optimized to converge the total energy and forces within 10^{-6} eV and 0.01 eV/Å, respectively. Considering the known underestimation of the band gap at the semilocal level due to spurious self-interaction in the effective potential, we also applied the hybrid Heyd–Scuseria–Ernzerhof functional (HSE06) for improved descriptions of the band gaps.[24] The atomic positions and the lattice vectors of the bulk structures were fully optimized to converge the interatomic forces within 0.05 eV/Å.

3.3 Results and Discussion

In a typical synthesis, $Cu(acac)_2$ was reacted with Ph_2Se_2 in oleylamine at 220 °C, as described in detail in the Experimental Section. Figure 3.1a shows a TEM image of the particles that formed during this reaction; the corresponding size distribution histogram is shown in Figure 3.1b. The particles had an average diameter of 18 ± 6 nm, as measured at the widest point. Figure 3.1c shows a HAADF-STEM image of the particles, along with corresponding STEM-EDS maps

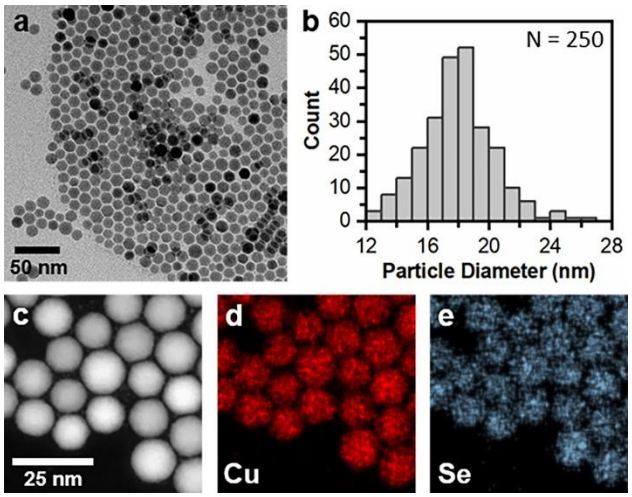

Figure 3.1: (a) TEM image of the as-synthesized copper selenide nanoparticles. (b) Size distribution histogram indicating an average particle diameter of 18 ± 6 nm (N = 250, 2σ). (c) HAADF-STEM image with accompanying STEM-EDS element maps for (d) Cu (Kα) and (e) Se (Kα).

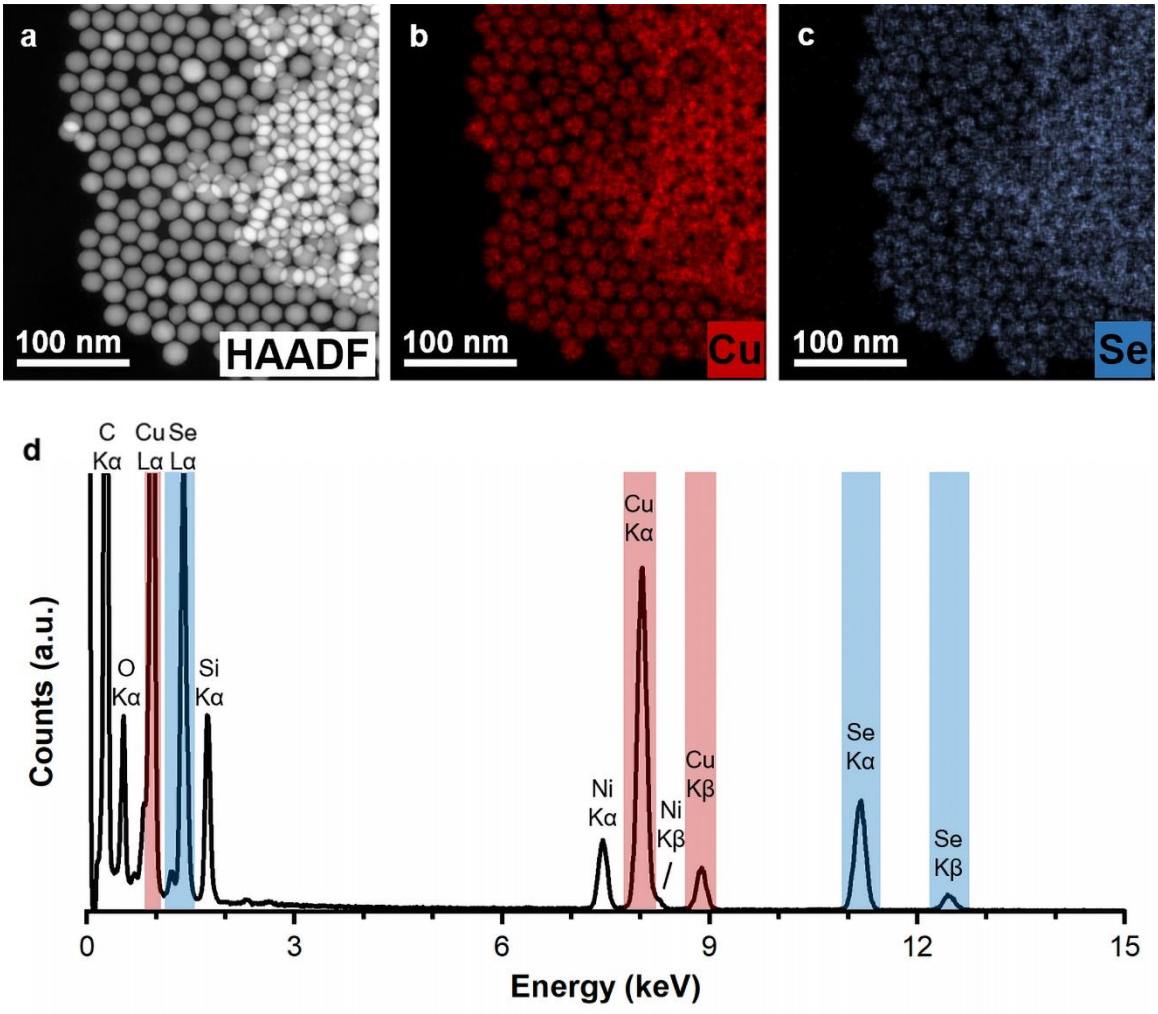

Figure 3.2: (a) HAADF-STEM image of the as-synthesized copper selenide nanoparticles. (b, c) Cu K*α* and Se K*α* STEM-EDS element maps. (d) Ensemble EDS spectrum from the mapping data shown in (b) and (c). The Cu and Se peaks are highlighted; a Ni grid was used. Standardless Cliff-Lorimer quantification gives a nominal 2:1 stoichiometry (Cu to Se).

in Figure 3.1d,e that show a uniform colocalization of Cu and Se throughout the particles. Ensemble EDS data, shown in Figure 3.2, indicate an ~2:1 ratio of Cu/Se, which is consistent with a formula of $Cu_{2-x}Se$, within typical experimental error.

The nominal composition was further confirmed by XPS analysis. Quantitative analysis of the Cu 2p and Se 3d regions indicated a 2.15:1 Cu/Se ratio, which is consistent with the $Cu_{2-x}Se$ stoichiometry and a surface that is Cu-rich and/or that contains a thin copper oxide layer. Figure 3.3a shows high-resolution spectra of the Cu 2p and Se 3d regions. The Cu 2p spectrum showed

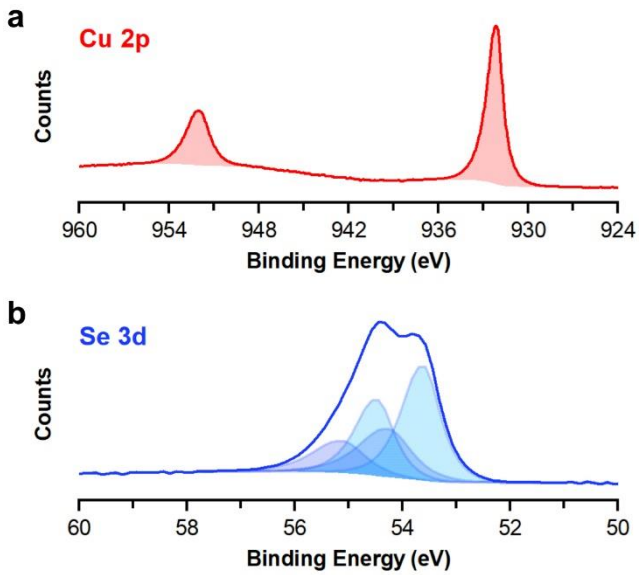

Figure 3.3: High-resolution XPS spectra of the (a) Cu 2p and (b) Se 3d regions. The Cu 2p region shows two peaks corresponding to the Cu $2p_{1/2}$ and Cu $2p_{3/2}$ photoelectrons with binding energies of 952.0 and 932.1 eV, respectively. The model fit for these peaks is shown in red. The Se 3d region shows two peaks corresponding to the deconvolution (highlighted in two shades of blue) of two separate sets of Se $3d_{3/2}$ and $3d_{5/2}$ peaks. The corresponding $3d_{5/2}$ peaks are centered at 54.3 and 53.6 eV. The distance between the $3d_{3/2}$ and $3d_{5/2}$ was fixed at 0.86 eV.

two peaks corresponding to $2p_{1/2}$ and $2p_{3/2}$ photoelectrons with binding energies of 952.0 and 932.1 eV, respectively. These binding energy values agree with literature reports for other $Cu_{2-x}Se$ phases.[7, 25] The peaks were fitted with a single curve corresponding to either Cu^0 or Cu^+; there are no observed satellite peaks, which would be associated with Cu^{2+} from either surface oxidation or from within the sample. However, finer features from a small amount of oxidized copper may not be resolvable, so the presence of a thin oxide shell cannot be ruled out.[26] Further analysis of the Cu $L_3M_{4,5}M_{4,5}$ Auger peak from the survey scan Figure 3.4, which was used to determine if the $2p_{3/2}$ peak was due to Cu^0 or Cu^+, showed a peak maximum with an associated kinetic energy of 917.8 eV. This is in good agreement with the expected Auger peak for a Cu^+ species.[27]

The Se 3d spectrum (Figure 3.3b) showed two overlapping peaks with binding energies of 54.4 and 53.8 eV, which are associated with the $3d_{3/2}$ and $3d_{5/2}$ photoelectrons, respectively. However, the ratio of peak intensities differs from that expected for a single Se species.[28] The 3d region was therefore fitted with two doublets having $3d_{5/2}$ peaks centered at 54.3 and 53.6 eV,

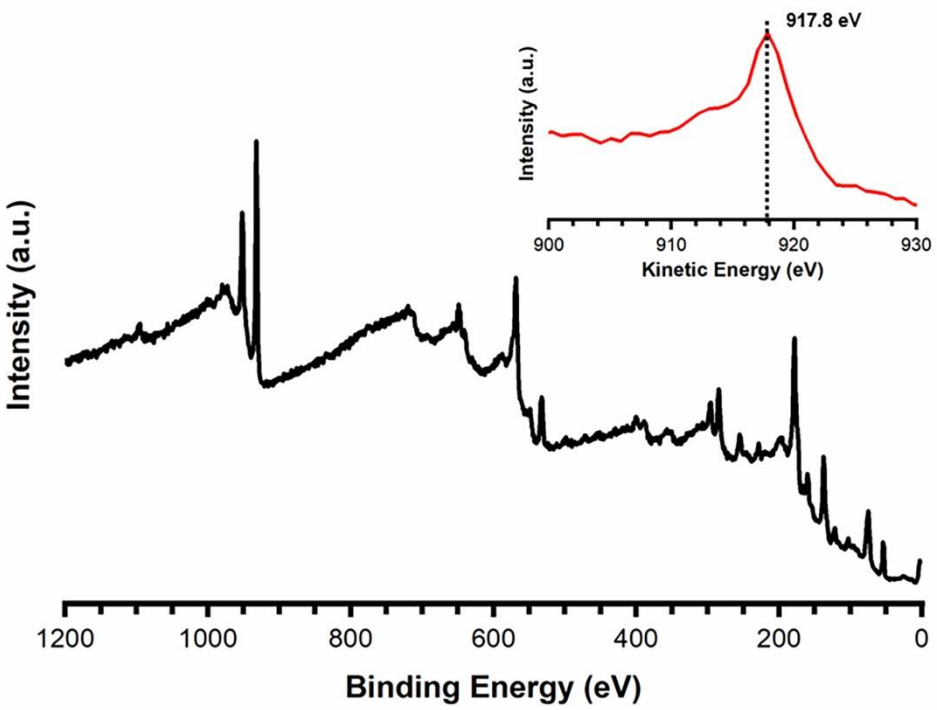

Figure 3.4: XPS survey scan of the $Cu_{2-x}Se$ nanoparticles. The Cu $L_3M_{4,5}M_{4,5}$ region (inset) shows a singular peak with a kinectic energy of 917.8 eV.

respectively, and with peak separations between the $3d_{3/2}$ and $3d_{5/2}$ fixed at 0.86 eV. The presence of the two doublets could possibly be due to differences in Se coordination environment.[28] A pair of doublets has also been attributed to potential breakdown products of the Se precursor and formation of polymeric Se intermediates, which could be left over after washing the particles.[29]

The preceding data confirmed the nominal 2:1 composition of the nanoparticles and that the chemical environment was consistent with a $Cu_{2-x}Se$ phase. Moving to structural characterization, the XRD pattern for the $Cu_{2-x}Se$ nanoparticles is shown in Figure 3.5. This XRD pattern does not match with any previously reported XRD patterns for known cubic, tetragonal, orthorhombic, or monoclinic phases of $Cu_{2-x}Se$ nor for the other known copper selenide phases, which include tetragonal Cu_3Se_2, hexagonal CuSe, and orthorhombic $CuSe_2$. The experimental XRD pattern bears some resemblance to the recently reported wurtzite-related $Cu_{2-x}Se$ phase, which captures several of the most intense reflections.[6] However, the XRD pattern for the wurtzite-

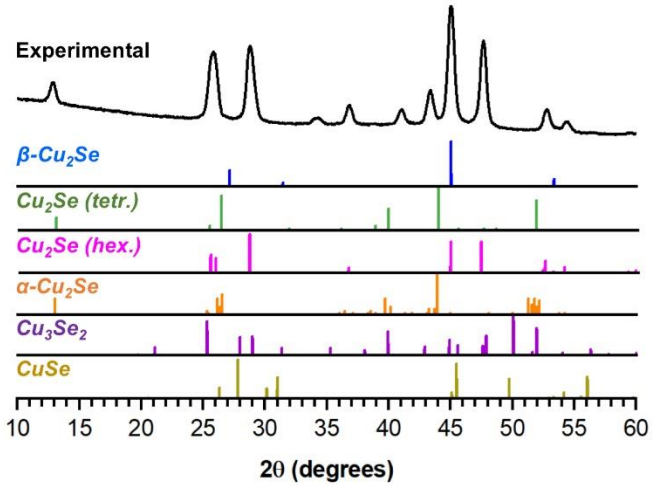

Figure 3.5: (Top) experimental powder XRD pattern of the as-synthesized $Cu_{2-x}Se$ nanoparticles. Bottom: reference patterns for cubic β-Cu_2Se (ICSD: 00-018-1661), tetragonal Cu_2Se (ICSD: 00-029-0575), hexagonal wurtzite-like Cu_2Se (simulated from ref 6), monoclinic α-Cu_2Se (ICSD: 00-027-1131), umangite Cu_3Se_2 (simulated from ref 5), and klockmannite CuSe (simulated from ref 5). None of these reference XRD patterns, corresponding to known Cu–Se phases, capture all of the peaks in the experimental XRD pattern.

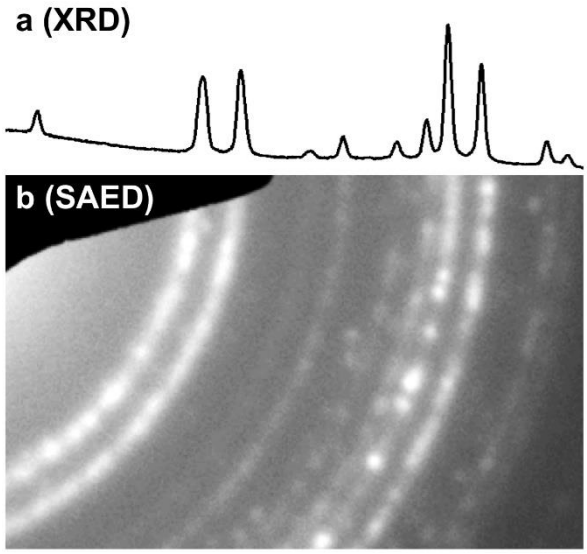

Figure 3.6: (a) Experimental powder XRD pattern of the $Cu_{2-x}Se$ nanoparticles, reproduced from Figure 3.5. (b) SAED pattern corresponding to an ensemble of $Cu_{2-x}Se$ nanoparticles.

like $Cu_{2-x}Se$ phase does not include the low-angle reflection near 13° 2θ nor any of the weaker reflections that are present in our XRD pattern.

Both single-particle and ensemble EDS spectra, as well as XPS data, indicate a nominal 2:1 Cu/Se ratio, without evidence for secondary phases or impurities. We therefore assume that the

XRD peaks that do not match known phases do indeed correspond to the $Cu_{2-x}Se$ nanoparticles and, accordingly, must be accounted for in any structural model. Further evidence that these peaks are intrinsic to the $Cu_{2-x}Se$ phase is provided by analysis of the SAED pattern shown in Figure 3.6. All of the diffraction rings expected based on the XRD pattern are present in the SAED pattern, which was collected on a small sample of $Cu_{2-x}Se$ nanoparticles.

Based on the good agreement between the SAED and XRD data, as well as between the EDS data and the XPS data, we are confident that the nanoparticles are largely phase-pure with a nominal $Cu_{2-x}Se$ composition and without evidence for crystalline minority subpopulations or amorphous components. We can now begin to decipher the crystal structure of the $Cu_{2-x}Se$ nanoparticles. Because the XRD pattern in Figure 3.5 did not match with any known Cu–Se phase of which we are aware, we expanded our search to other known nonselenide copper chalcogenide phases to look for a potential structural match. Our rationale was that structures known to form for the $Cu_{2-x}S$ and $Cu_{2-x}Te$ systems may be among the most plausible metastable phases in the $Cu_{2-x}Se$ system.

The closest match, based on known phases with experimentally determined XRD patterns, was weissite $Cu_{1.78}Te$ (PDF 00-010-0421) (Figure 3.7). The XRD pattern for weissite $Cu_{1.78}Te$ is

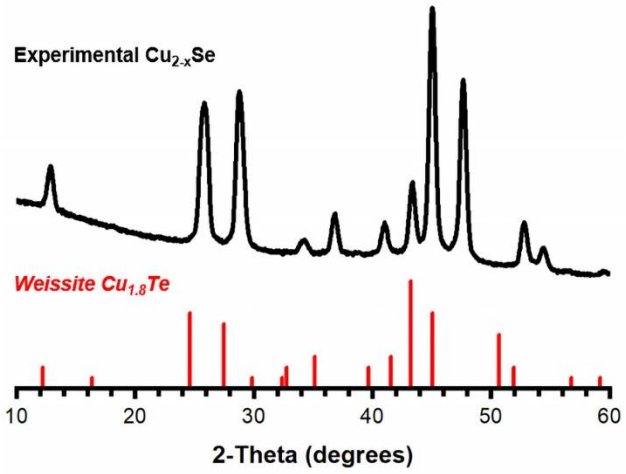

Figure 3.7: Experimental XRD pattern of the weissite-like $Cu_{2-x}Se$ nanoparticles and reference pattern for weissite $Cu_{1.8}Te$ (ICSD: 00-010-0421).

remarkably similar to that in Figure 3.5 for $Cu_{2-x}Se$, after the lattice parameters are empirically adjusted to match those experimentally determined for $Cu_{2-x}Se$. However, the exact structure of weissite $Cu_{2-x}Te$ is not well understood and is still debated in the literature. Recently, Yu et al. reported a computational study of potential Cu-deficient structures of $Cu_{2-x}Te$, which sought to better represent weissite $Cu_{2-x}Te$ compared to previously proposed structures.[30] Of the potential structures proposed in this report, a trigonal structure previously proposed by Matar and co-workers showed the greatest match to the weissite phase.[31] We constructed a model structure for our observed $Cu_{2-x}Se$ nanoparticles using the atomic coordinates of weissite $Cu_{2-x}Te$ from Yu et al. and

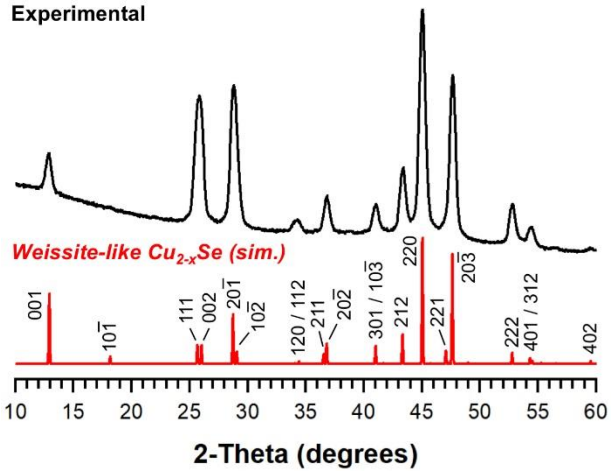

Figure 3.8: Experimental powder XRD pattern for the weissite-like $Cu_{2-x}Se$ nanoparticles with a simulated pattern created using the space group and atomic coordinates from ref (30) and the experimentally determined lattice parameters for $Cu_{2-x}Se$.

our experimentally determined lattice parameters for our $Cu_{2-x}Se$ nanoparticle sample, using a nominal 2:1 stoichiometry. When compared to the experimental XRD pattern in Figure 3.5, the structural model for weissite-like $Cu_{2-x}Se$ agrees reasonably well, as confirmed in Figure 3.8, acknowledging that the broadened XRD peaks that are inherent for nanoparticles preclude absolute, unambiguous structural determination, as do the same challenges associated with the weissite $Cu_{2-x}Te$ structure noted above and in refs (30 and 31). The structural model captures the 001 peak at 13° 2θ in addition to the weaker peaks between 30 and 45° 2θ (112, 022$\bar{}$, 031, and 122).

To help refine our structural model, an optimized structural geometry was obtained using density functional calculations. The XRD reference pattern (Figure 3.5) obtained from the optimized structure calculated using the PBE functional shows only a marginal (1.6%) lattice

Table 3.1: Comparison between experimentally determined lattice parameters and DFT calculations (PBE and HSE06) for current work and antifluorite β-Cu_2Se (berzelianite).

	Exp. Lattice Parameters (Å)		Theor. Lattice Parameters, PBE (Å)		Theor. Lattice Parameters, HSE (Å)	
Material	a	c	a	c	a	c
Current Work	8.03	6.89	8.13	6.99	8.16	6.93
B-Cu_2Se	5.694[§]	-	5.81	-	5.80	-

[§]ICSD: 01-088-2043

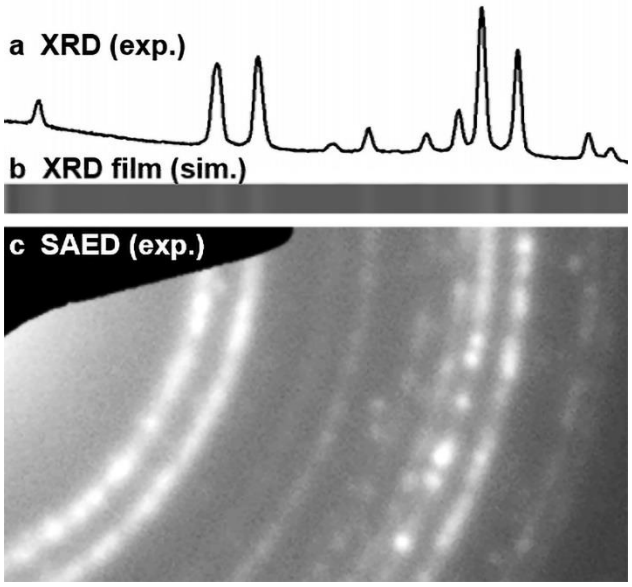

Figure 3.9: Comparisons of the experimental XRD pattern, a simulated XRD film from the weissite-like structural model for $Cu_{2-x}Se$, and experimental SAED pattern. All three are in good agreement.

expansion from the one experimentally determined; complementary calculations using the HSE06 functional produce a similarly small (1.4%) deviation in the lattice parameter. The calculated structural parameters are shown in Table 3.1. By examining the SAED image and experimental XRD pattern in Figure 3.6, and by comparing these data with Figure 3.9, it is clear that the structural model can account for all of the observed diffraction rings.

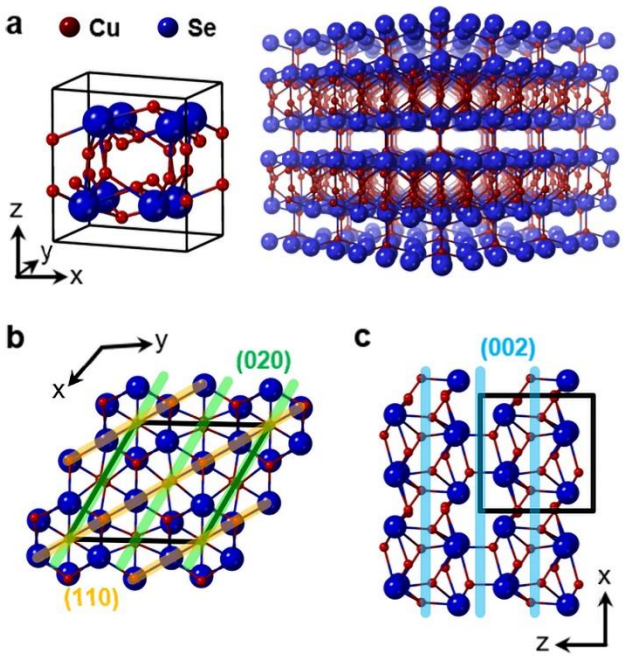

Figure 3.10: Crystallographic projections of weissite-like $Cu_{2-x}Se$ (a). Panels (b) and (c) correspond to the particle orientations in Figure 3.11.

Figure 3.10 shows the crystal structure of weissite-like $Cu_{2-x}Se$ (space group $P\bar{3}m1$). In this structure, Cu occupies trigonal and tetrahedral interstices in a slightly distorted hexagonal Se sublattice. The Cu atoms are distributed such that there are four crystallographically unique sites with Cu being either 3- or 4-coordinate. Se occupies two distinct crystallographic sites. This structure has Cu-rich and Cu-deficient layers sandwiching a distorted hexagonal layer of Se. The Cu-rich layers are held together by Se–Cu–Se bonds across the Cu-deficient layers. Additional crystallographic projections can be observed in Figure 3.11. For comparison, klockmannite CuSe, the other known layered phase of copper selenide, has bridging Se–Se bonds.[32] There have been a

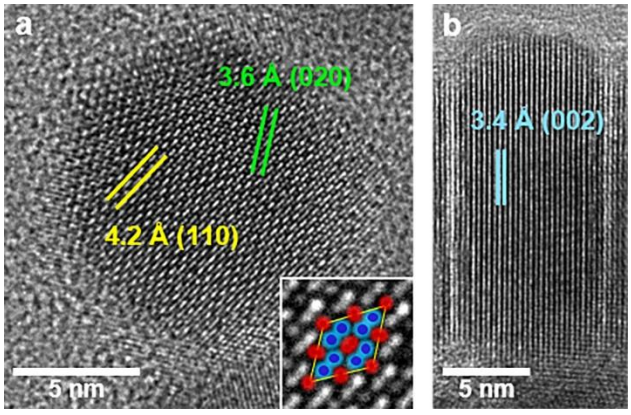

Figure 3.11: High-resolution TEM images of weissite-like $Cu_{2-x}Se$ nanoparticles (a) lying on their faces and (b) lying on their sides. The labeled lattice spacings and angles correlate well with the crystal structure of weissite-like $Cu_{2-x}Se$ shown in Figure 3.10 (Inset) The labeled crystallographic projection corresponds to the projection in Figure 3.10b. Cu atoms are red and Se atoms are blue.

few other computational studies that predict additional layered structures of $Cu_{2-x}Se$, but at present, they have not been synthesized to the best of our knowledge.[33, 34]

To probe the stability of our weissite-like $Cu_{2-x}Se$ particles, we took preformed particles and subjected them to solution-phase annealing at elevated temperatures. Here, the weissite-like $Cu_{2-x}Se$ particles were annealed at 250 °C in 1-octadecene with an aliquot taken after 30 min. The temperature then was ramped to 280 °C and held for an additional 30 min. These temperatures were chosen as they matched similar synthetic conditions reported for berzelianite $Cu_{2-x}Se$ nanoparticles. 1-Octadecene was chosen for annealing studies as it is a noncoordinating solvent and should have minimal reactivity toward the particles. No additional ligands were added to the reaction. XRD analysis of the annealed particles showed that the particles underwent a phase change to berzelianite (Figure 3.12a), which suggests that the weissite-like $Cu_{2-x}Se$ phase is not thermodynamically stable.

To further probe the stability of the weissite-like $Cu_{2-x}Se$ nanoparticles, a series of aliquots were taken from the standard reaction conditions, where the particles were held for increasingly longer times at 220 °C. The resulting XRD analysis of the particles (Figure 3.12b) shows that the weissite-like $Cu_{2-x}Se$ phase persists at longer times than were used in the original synthesis, which

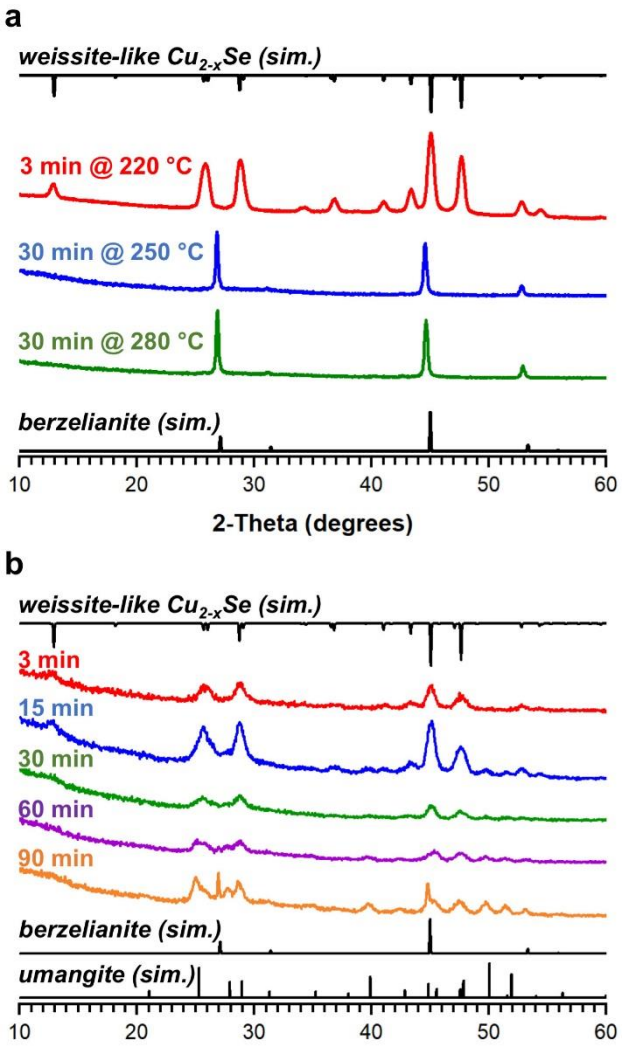

Figure 3.12: (a) Experimental XRD patterns for weissite-like $Cu_{2-x}Se$ and nanoparticles as-synthesized and thermally annealed in solution at 250 °C for 30 min and at 280 °C for an additional 30 min. Particles were observed to decompose from the metastable weissite-like $Cu_{2-x}Se$ phase to the high-temperature, berzelianite $Cu_{2-x}Se$ phase. (b) Experimental XRD patterns for weissite-like $Cu_{2-x}Se$ nanoparticles as-synthesized and after heated for extended reaction times at 220 °C for 3, 15, 30, 60, and 90 min. Extended reaction times allowed for the conversion from weissite-like $Cu_{2-x}Se$ to umangite Cu_3Se_2 and then to berzelianite $Cu_{2-x}Se$. Reference patterns: berzelianite (ICSD: 00-018-1661) and umangite (ref 5).

was just 3 min. However, at 15 min, additional peaks at 27 and 40° 2θ emerge. At 30 min, a noticeable loss in crystallinity is observed. At 60 min, there is a further loss of crystallinity with an emergence of an umangite Cu_3Se_2 impurity, presumably formed through a decomposition pathway. At 90 min, sharp peaks corresponding to berzelianite $Cu_{2-x}Se$ are present along with broad peaks associated with the umangite impurity and the remaining weissite-like $Cu_{2-x}Se$. Taken together, the

thermal stability data suggest that weissite-like $Cu_{2-x}Se$ is metastable and therefore is a kinetically trapped product that forms at lower temperatures, facilitated by the use of the reactive Ph_2Se_2 selenium reagent.

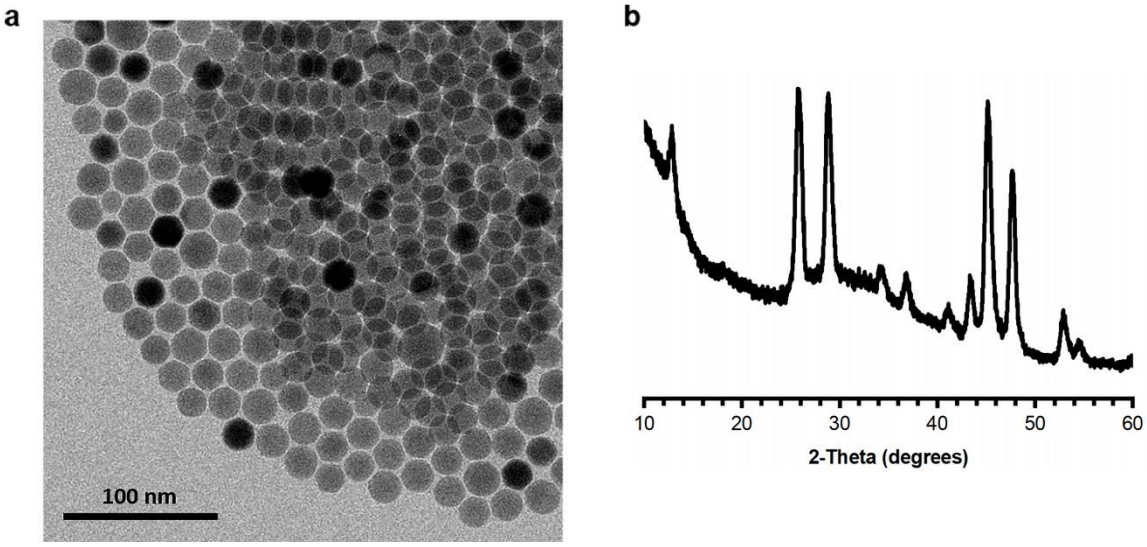

Figure 3.13: (a) TEM imagen and (b) XRD pattern of weissite-like $Cu_{2-x}Se$ nanoparticles synthesized by the alternative method.

Slight modifications to the reaction time, temperature, and reagents also produce similar nanoparticles of weissite-like $Cu_{2-x}Se$ (Figure 3.13), indicating that the formation of this metastable phase is fairly robust. It is interesting to consider how the differences between our synthesis—which used $Cu(acac)_2$, Ph_2Se_2, and oleylamine at 200–220 °C—and previously reported syntheses of various $Cu_{2-x}Se$ phases lead to different products. When copper oleate was used with Ph_2Se_2, umangite Cu_3Se_2 formed, suggesting different reactivity and/or element availability when the acac vs oleate reagents were used, given the otherwise very similar conditions.[17] In this example, the color progression was different from ours (blue to yellow to brown vs green to brown), also suggesting a different pathway in which active copper and selenium species were temporally separated. When CuCl was used (with Ph_2Se_2, 1-octadecene, and oleylamine) at a higher temperature (270 °C), the more stable berzelianite $Cu_{2-x}Se$ phase formed; lower temperatures introduced an umangite Cu_3Se_2 impurity, suggesting that temperature correlated with selenium

availability in solution.[35] These examples provide additional insights into how phase targeting can be achieved in the Cu–Se nanoparticle system, although it is clear that subtle differences can have significant impact on product formation in this complex system.

Many cation-deficient copper chalcogenides are known to be degenerately doped semiconductors, as they can tolerate a relatively large number of ion vacancies, which increases their overall charge carrier concentrations.[36] This increase in charge carrier concentration allows for the material to sustain localized surface plasmon resonances, particularly in the NIR.[37] Since the plasmon resonance frequency is heavily influenced by the charge carrier concentration, cation-deficient copper chalcogenides have received intense interest for their potential use as tunable absorbers for applications in sensing, bioimaging, and theranostics.[38–40] For example, berzelianite $Cu_{2-x}Se$ nanoparticles exhibit an intense NIR plasmon band that blue-shifts from 1700 to 1100 nm, while also narrowing, upon gradual oxidation over the course of 60 min under ambient conditions.[13] Wurtzite-like $Cu_{2-x}Se$ nanoparticles undergo a similar oxidation process under ambient conditions, although they appear to be more resistant to oxidation, showing no NIR plasmon band until a week after exposure to ambient conditions.[19]

We analyzed a dispersion of our weissite-like $Cu_{2-x}Se$ nanoparticles in tetrachloroethylene by UV–vis–NIR to identify and characterize its plasmonic properties. A broad plasmon band centered around 1550 nm was observed in a freshly prepared sample that had been worked up under ambient conditions (Figure 3.14a). When this sample was analyzed again after 2 weeks of storage under ambient conditions, there was only a very slight ~50 nm shift and narrowing of the plasmon band, which was now centered around 1500 nm (Figure 3.14a). Like wurtzite-like $Cu_{2-x}Se$, our weissite-like $Cu_{2-x}Se$ phase appears to be relatively stable to oxidation beyond any that may have occurred during sample preparation and isolation.

To test whether the plasmon band is inherent to weissite-like $Cu_{2-x}Se$ or due to surface oxidation, we also ran a series of control experiments where small quantities of a Cu^{+} solution were

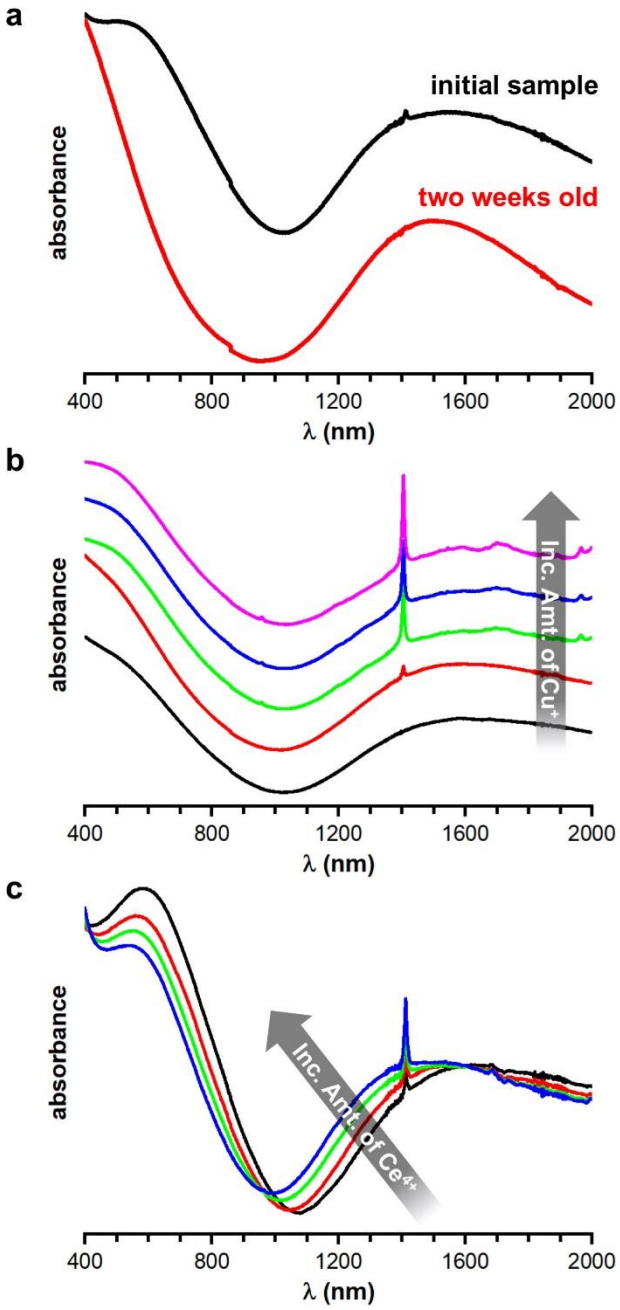

Figure 3.14: (a) UV–vis–NIR spectra of the weissite-like $Cu_{2-x}Se$ nanoparticles. The initial sample was analyzed after working up under ambient conditions, and the 2 week old sample was analyzed after 2 weeks stored under ambient conditions. UV–vis–NIR spectra for the weissite-like $Cu_{2-x}Se$ nanoparticles treated under (b) reducing and (c) oxidizing conditions. The spectra for the reduction studies in (b) were offset to better show the plasmon peak position. For the oxidation study in (c), each addition was of 2 μL of a 0.1 M $(NH_4)_2Ce(NO_3)_6$ solution in ethanol. All samples were analyzed under ambient conditions.

added to the nanoparticle suspensions and then analyzed (Figure 3.14b), as was done previously to

test for similar behavior.[13, 41] In this prior work, introducing Cu^+ cations to cation-deficient $Cu_{1.1}S$ nanoparticles initiated a spontaneous cation-exchange reaction to form Cu_2S. This resulted in the plasmon band red-shifting from approximately 1100 to 1300 nm. In our analogous experiment on weissite-like $Cu_{2-x}Se$, it was observed that even with incrementally increasing amounts of Cu^+ in solution, the plasmon band did not shift. This suggests that the material is already in its most reduced state, which is consistent with the XPS analysis in Figures 3.3 and 3.4, which only showed Cu^+ (and not Cu^{2+}) present in our material. To further probe the NIR plasmon band, we subjected our weissite-like $Cu_{2-x}Se$ particles to oxidative conditions using $(NH_4)_2Ce(NO_3)_6$, as also was done previously to probe stability and reactivity.[13] With stepwise additions of Ce^{4+}, we observed that the plasmon band blue-shifted from approximately 1550 to 1475 nm (Figure 3.14c). This contrasts with berzelianite $Cu_{2-x}Se$, where a larger blue shift in the NIR plasmon band was observed when the particles were placed under similar conditions.[13] Taken together, these results suggest that the plasmonic properties of weissite-like $Cu_{2-x}Se$ are inherent to the material and not susceptible to significant changes in the plasmonic band due to chemical manipulation. Since the plasmonic properties of these classes of materials depend strongly on the concentration of charge carriers, it can be postulated that weissite-like $Cu_{2-x}Se$ has an inherently high carrier concentration. This could be due to the differences between the two layers of the material, with the Cu^+-deficient layer being the potential source of Cu^+ vacancies in the structures.

3.4 Conclusion

We have shown the direct synthesis of a previously unreported metastable phase of copper selenide as colloidal nanoparticles. The $Cu_{2-x}Se$ nanoparticles adopt a structure similar to that of weissite $Cu_{1.8}Te$, which has alternating copper-rich and copper-deficient layers sandwiching a distorted hexagonal layer of selenium. The weissite-like $Cu_{2-x}Se$ nanoparticles exhibit an NIR plasmon band centered around 1550 nm. Ambient storage, as well as oxidizing and reducing

conditions, does not significantly change the plasmon band, confirming its relative stability. Copper selenides are important materials for a variety of applications, and the weissite-like $Cu_{2-x}Se$ nanoparticles add to the library of available materials. Cation-deficient copper selenides are also useful templates for postsynthetic modification, including through topotactic cation exchange that can change the composition and produce heterostructured nanoparticles having complex internal interfaces. The weissite-type $Cu_{2-x}Se$ nanoparticles could provide a cation-exchange template that is structurally distinct from existing systems.

* This chapter was adapted from Lord, R.W.; Fanghanel, J.; Holder, C.F.; Dabo, I.; Schaak, R.E. "Colloidal Nanoparticles of a Metastable Copper Selenide Phase with Near-Infrared Plasmon Resonance," *Chem. Mater.* **2020**, *32*, 10227-10234, with permission. Copyright 2020, American Chemical Society.

3.5 Acknowledgements

This work was supported by the U.S. National Science Foundation under Grant DMR-1904122. J.F. and I.D. acknowledge support by the DMREF and INFEWS programs of the U.S. National Science Foundation under Grant DMREF-1729338. TEM/STEM imaging, EDS mapping, XPS, and X-ray diffraction were performed at the Materials Characterization Lab of the Penn State Materials Research Institute. The authors thank Dr. Lucas T. Alameda and Benjamin C. Steimle for their helpful discussions.

3.6 References

(1) Hessel, C. M.; Pattani, V. P.; Rasch, M.; Panthani, M. G.; Koo, B.; Tunnell, J. W.; Korgel, B. A. Copper Selenide Nanocrystals for Photothermal Therapy. *Nano Lett.* **2011**, *11*, 2560–256.

(2) Zhou, R.; Huang, Y.; Zhou, J.; Niu, H.; Wan, L.; Li, Y.; Xu, J.; Xu, J. Copper Selenide (Cu_3Se_2 and $Cu_{2-x}Se$) Thin Films: Electrochemical Deposition and Electrocatalytic Application in Quantum Dot-Sensitized Solar Cells. *Dalton Trans.* **2018**, *47*, 16587– 16595.

(3) Yue, J.-L.; Sun, Q.; Fu, Z.-W. Cu_2Se with Facile Synthesis as a Cathode Material for Rechargeable Sodium Batteries. *Chem. Commun.* **2013**, *49*, 5868– 5870.

(4) Liu, S.; Zhang, Z.; Bao, J.; Lan, Y.; Tu, W.; Han, M.; Dai, Z. Controllable Synthesis of Tetragonal and Cubic Phase Cu_2Se Nanowires Assembled by Small Nanocubes and Their Electrocatalytic Performance for Oxygen Reduction Reaction. *J. Phys. Chem. C* **2013**, *117*, 15164– 15173.

(5) Murray, R. M.; Heyding, R. D. The Copper-Selenium System at Temperatures to 850 K and Pressures to 50 Kbar. *Can. J. Chem.* **1975**, *53*, 878– 887.

(6) Gariano, G.; Lesnyak, V.; Brescia, R.; Bertoni, G.; Dang, Z.; Gaspari, R.; de Trizio, L.; Manna, L. Role of Crystal Structure in Cation Exchange Reactions Involving Colloidal Cu_2Se Nanocrystals. *J. Am. Chem. Soc.* **2017**, *139*, 9583– 9590.

(7) Riha, S. C.; Jonson, D. C.; Prieto, A. L. Cu_2Se Nanoparticles with Tunable Electronic Properties Due to a Controlled Solid-State Phase Transition Driven by Copper Oxidation and Cationic Conduction. *J. Am. Chem. Soc.* **2011**, *133*, 1383– 1390.

(8) Danilkin, S. A.; Skomorokhov, A. N.; Hoser, A.; Fuess, H.; Rajevac, V.; Bickulova, N. N. Crystal Structure and Lattice Dynamics of Superionic Copper Selenide $Cu_{2-\delta}Se$. *J. Alloys Compd.* **2003**, *361*, 57– 61.

(9) Liu, H.; Shi, X.; Xu, F.; Zhang, L.; Zhang, W.; Chen, L.; Li, Q.; Uher, C.; Day, T.; Snyder, G. J. Copper Ion Liquid-like Thermoelectrics. *Nat. Mater.* **2012**, *11*, 422– 425.

(10) Masud, J.; Liyanage, W. P. R.; Cao, X.; Saxena, A.; Nath, M. Copper Selenides as High-Efficiency Electrocatalysts for Oxygen Evolution Reaction. *ACS Appl. Energy Mater.* **2018**, *1*, 4075– 4083.

(11) Liu, X.; Wang, X.; Zhou, B.; Law, W. C.; Cartwright, A. N.; Swihart, M. T. Size-Controlled Synthesis of $Cu_{2-x}E$ (E=S, Se) Nanocrystals with Strong Tunable Near-Infrared Localized Surface Plasmon Resonance and High Conductivity in Thin Films. *Adv. Funct. Mater.* **2013**, *23*, 1256– 1264.

(12) Kriegel, I.; Jiang, C.; Rodríquez-Fernández, J.; Schaller, R. D.; Talapin, D. V.; da Como, E.; Feldmann, J. Tuning the Excitonic and Plasmonic Properties of Copper Chalcogenide Nanocrystals. *J. Am. Chem. Soc.* **2012**, *134*, 1583– 1590.

(13) Dorfs, D.; Härtling, T.; Miszta, K.; Bigall, N. C.; Kim, M. R.; Genovese, A.; Falqui, A.; Povia, M.; Manna, L. Reversible Tunability of the Near-Infrared Valence Band Plasmon Resonance in $Cu_{2-x}Se$ Nanocrystals. *J. Am. Chem. Soc.* **2011**, *133*, 11175– 11180.

(14) Zingaro, R. A.; McGlothlin, R. E. Some Phosphines, Phosphine Sulfides, and Phosphine Selenides. *J. Chem. Eng. Data* **1963**, *8*, 226– 229.

(15) Murray, C. B.; Norris, D. J.; Bawendi, M. G. Synthesis and Characterization of Nearly Monodisperse CdE (E = Sulfur, Selenium, Tellurium) Semiconductor Nanocrystallites. *J. Am. Chem. Soc.* **1993**, *115*, 8706– 8715.

(16) Qu, L.; Peng, Z. A.; Peng, X. Alternative Routes Toward High Quality CdSe Nanocrystals. *Nano Lett.* **2001**, *1*, 333– 337.

(17) Tappan, B. A.; Barim, G.; Kwok, J. C.; Brutchey, R. L. Utilizing Diselenide Precursors toward Rationally Controlled Synthesis of Metastable $CuInSe_2$ Nanocrystals. *Chem. Mater.* **2018**, *30*, 5704– 5713.

(18) Brutchey, R. L. Diorganyl Dichalcogenides as Useful Synthons for Colloidal Semiconductor Nanocrystals. *Acc. Chem. Res.* **2015**, *48*, 2918– 2926.

(19) Hernández-Pagán, E. A.; Robinson, E. H.; La Croix, A. D.; Macdonald, J. E. Direct Synthesis of Novel $Cu_{2-x}Se$ Wurtzite Phase. *Chem. Mater.* **2019**, *31*, 4619– 4624.

(20) Perdew, J. P.; Burke, K.; Ernzerhof, M. Generalized Gradient Approximation Made Simple. *Phys. Rev. Lett.* **1996**, *77*, 3865.

(21) Kresse, G.; Joubert, D. From Ultrasoft Pseudopotentials to the Projector Augmented-Wave Method. *Phys. Rev. B* **1999**, *59*, 1758.

(22) Blöchl, P. E. Projector Augmented-Wave Method. *Phys. Rev. B* **1994**, *50*, 17953.

(23) Kresse, G.; Furthmüller, J. Efficient Iterative Schemes for Ab Initio Total-Energy Calculations Using a Plane-Wave Basis Set. *Phys. Rev. B* **1996**, *54*, 11169.

(24) Krukau, A. V.; Vydrov, O. A.; Izmaylov, A. F.; Scuseria, G. E. Influence of the Exchange Screening Parameter on the Performance of Screened Hybrid Functionals. *J. Chem. Phys.* **2006**, *125*, 224106.

(25) Cahen, D.; Ireland, P. J.; Kazmerski, L. L.; Thiel, F. A. X-ray Photoelectron and Auger Electron Spectroscopic Analysis of Surface Treatments and Electrochemical Decomposition of $CuInSe_2$ Photoelectrodes. *J. Appl. Phys.* **1985**, *57*, 4761– 4771.

(26) Biesinger, M. C.; Lau, L. W. M.; Gerson, A. R.; Smart, R. S. C. Resolving Surface Chemical States in XPS Analysis of First Row Transition Metals, Oxides and Hydroxides: Sc, Ti, V, Cu, and Zn. *Appl. Surf. Sci.* **2010**, *257*, 887– 898.

(27) Biesinger, M. C. Advanced Analysis of Copper X-ray Photoelectron Spectra. *Surf. Interface Anal.* **2017**, *49*, 1325– 1334.

(28) Moulder, J. F.; Stickle, W. F.; Sobol, P. E.; Bomben, K. D. *Handbook of X-ray Photoelectron Spectroscopy: A Reference Book of Standard Spectra for Identification and Interpretation of XPS Data*; Physical Electronics, Inc.: Chanhassen, MN, 1995.

(29) Bullen, C.; van Embden, J.; Jasieniak, J.; Cosgriff, J. E.; Mulder, R. J.; Rizzardo, E.; Gu, M.; Raston, C. L. High Activity Phosphine-Free Selenium Precursor Solution for Semiconductor Nanocrystal Growth. *Chem. Mater.* **2010**, *22*, 4135– 4143.

(30) Yu, L.; Luo, K.; Chen, S.; Duan, C.-G. Cu-Deficiency Induced Structural Transition of $Cu_{2-x}Te$. *CrystEngComm* **2015**, *17*, 2878– 2885.

(31) Matar, S. F.; Weihrich, R.; Kurowski, D.; Pfitzner, A. DFT Calculations on the Electronic Structure of $CuTe_2$ and Cu_7Te_4. *Solid State Sci.* **2004**, *6*, 15– 20.

(32) Liu, Y.-Q.; Wang, F.-X.; Xiao, Y.; Peng, H.-D.; Zhong, H.-J.; Liu, Z.-H.; Pan, G.-B. Facile-Microwave-Assisted Synthesis of Klockmannite CuSe Nanosheets and Their Exceptional Electrical Properties. *Sci. Rep.* **2015**, *4*, 5998.

(33) Nguyen, M. C.; Choi, J.-H.; Zhao, X.; Wang, C.-Z.; Zhang, Z.; Ho, K.-M. New Layered Structures of Cuprous Chalcogenides as Thin Film Solar Cell Materials: Cu_2Te and Cu_2Se. *Phys. Rev. Lett.* **2013**, *111*, 165502.

(34) Chi, H.; Kim, H.; Thomas, J. C.; Shi, G.; Sun, K.; Abeykoon, M.; Bozin, E. S.; Shi, X.; Li, Q.; Shi, X.; Kioupakis, E.; Van; der Ven, A.; Kaviany, M.; Uher, C. Low-Temperature Structural and Transport Anomalies in Cu_2Se. *Phys. Rev. B* **2014**, *89*, 195209.

(35) Wang, W.; Zhang, Li.; Chen, G.; Jiang, J.; Ding, T.; Zuo, J.; Yang, Q. $Cu_{2-x}Se$ Nanooctahedra: Controllable Synthesis and Optoelectronic Properties. *CrystEngComm* **2015**, *17*, 1975– 1981.

(36) Wolf, A.; Kodanek, T.; Dorfs, D. Tuning the LSPR in Copper Chalcogenide Nanoparticles by Cation Intercalation, Cation Exchange and Metal Growth. *Nanoscale* **2015**, *7*, 19519– 19527.

(37) Luther, J. M.; Jain, P. K.; Ewers, T.; Alivisatos, A. P. Localized Surface Plasmon Resonances Arising from Free Carriers in Doped Quantum Dots. *Nat. Mater.* **2011**, *10*, 361– 366.

(38) Coughlan, C.; Ibáñez, M.; Dobrozhan, O.; Singh, A.; Cabot, A.; Ryan, K. M. Compound Copper Chalcogenide Nanocrystals. *Chem. Rev.* **2017**, *117*, 5865– 6109.

(39) Yun, B.; Zhu, H.; Yuan, J.; Sun, Q.; Li, Z. Synthesis, Modification and Bioapplications of Nanoscale Copper Chalcogenides. *J. Mater. Chem. B* **2020**, *8*, 4778– 4812.

(40) Zhao, Y.; Chen, B.-Q.; Kankala, R. K.; Wang, S.-B.; Chen, A.-Z. Recent Advances in Combination of Copper Chalcogenide-Based Photothermal and Reactive Oxygen Species-Related Therapies. *ACS Biomater. Sci. Eng.* **2020**, *6*, 4799– 4815.

(41) Xie, Y.; Riedinger, A.; Prato, M.; Casu, A.; Genovese, A.; Guardia, P.; Sottini, S.; Sangregorio, C.; Miszta, K.; Ghosh, S.; Pellegrino, T.; Manna, L. Copper Sulfide Nanocrystals with Tunable Composition by Reduction of Covellite Nanocrystals with Cu^{+} Ions. *J. Am. Chem. Soc.* **2013**, *135*, 17630– 17637.

Chapter 4

Insights into the Synthesis of Pt–$CuMSe_2$ (M = Fe, In) Hybrid Nanoparticles

4.1 Introduction

Hybrid nanoparticles are multifunctional materials characterized by the solid-state interfacing of multiple disparate nanocrystals in a single particle framework. They have been utilized for a diverse array of applications such as catalysis,[1] plasmonics,[2] bioimaging,[3] and optoelectronics.[4] Two-component hybrid nanoparticles, heterodimers, are the most commonly studied class of hybrid nanoparticles and include a larger array of material components such as metals,[5-7] metal oxides,[8-10] metal nitrides,[11] metal phosphides,[12] and metal halide perovskites.[13] There have also been strides in synthesizing more complex hybrid nanoparticles incorporating three or more distinct materials.[11, 14-16] These more sophisticated materials offer greater functionality over similar two-component systems and are necessary for some applications. For example, Oh et al. reported the use of double heterojunction CdS-CdSe-ZnSe nanorods in light-responsive light-emitting diodes.[4] The three component system was necessary for the function of their device due to the necessary band edge alignments. Another example is the proposed three-component, overall water splitting photocatalyst Pt-TiO_2-IrO_2 where TiO_2 acts as the photoabsorber with the Pt and IrO_2 domains acting as the hydrogen evolution catalyst and oxygen evolution catalyst, respectively.[17]

An attractive class of materials to be utilized in hybrid nanoparticles are copper-based I–III–VI_2 semiconductors. These materials and their quaternary analogues offer less toxic and electronically tunable alternatives to the more commonly utilized lead and cadmium-based chalcogenides.[18-20] There have been several reports of copper-based ternary and quaternary chalcogenides incorporated into metal-semiconducting hybrids including Pt–$CuInS_2$, Au–$CuInS_2$,

Au–$CuInGaSe_2$, Au–Cu_2ZnSnS_4, Pt–Cu_2ZnSnS_4, and Au–Cu_2FeSnS_4.[21–26] $CuInSe_2$ is a thermally stable, direct bandgap semiconductor with a high absorption coefficient.[27, 28] $CuFeSe_2$ is by far the least studied of the I–III–VI_2 chalcogenides, mostly due to its narrow bandgap; 0.16 eV in bulk.[29] $CuFeSe_2$ nanoparticle have gained recent attention for their interesting magnetic and optoelectronic properties.[30–32] Both of these materials are interesting candidates to be incorporated into hybrid nanoparticle structures. To date, there have been no reports of Pt–$CuInSe_2$ or Pt–$CuFeSe_2$ hybrid nanoparticles, although Zhang et al. reported the formation of core–shell Au@$CuInSe_2$ heterostructures although by alloying Cu with Au first then by chemically induced phase segregation.[33]

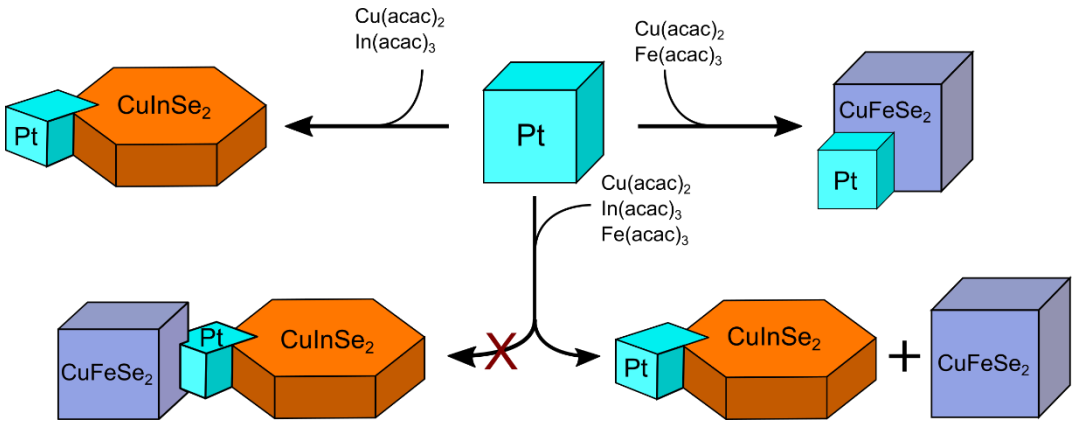

Figure 4.1: Schematic of the synthetic pathway of the synthesis of Pt–$CuMSe_2$ (M = Fe, In) hybrid nanoparticles by seeded growth.

Herein, we report the synthesis of Pt–$CuMSe_2$ (M = Fe, In) hybrid nanoparticles by seeded growth. The dimer nanoparticles, Pt–$CuFeSe_2$ and Pt–$CuInSe_2$, are individually shown to form, however when $CuFeSe_2$ and $CuInSe_2$ were attempted to grow simultaneously in solution, only the Pt–$CuInSe_2$ hybrid particles formed with single component $CuFeSe_2$ particles, Figure 4.1. Pt–$Cu_{2-x}Se$ hybrid particles were shown to form when neither Fe^{3+} nor In^{3+} precursor solutions were used. $CuInSe_2$ nanoparticles have been shown to form through an *in situ* cation exchange reaction from intermediate $Cu_{2-x}Se$ nanoparticles.[34] Cation exchange reactions using Cd and Fe were utilized to

verify the feasibility of the formed particles at higher temperatures. This was also the first demonstration of moderate temperature iron exchange reactions on preformed $Cu_{2-x}Se$ nanoparticles. Time-dependent aliquots of the $CuFeSe_2$ domain growth show that the formation of $CuFeSe_2$ does not occur through an *in situ* cation exchange reaction. Additionally, when oleic acid is used in the reaction, the rate of In^{3+} exchange is slowed down and the resulting particles show incomplete In^{3+} incorporation. This implied a reaction where the *in situ* cation exchange reaction is observationally faster than spontaneous nucleation. These synthetic insights have implications for understanding multiple domain growth in complex hybrid nanoparticle systems in addition to the formation of other ternary copper chalcogenides.

4.2 Experimental Section

4.2.1 Chemicals and Materials

Platinum(II) acetylacetonate [$Pt(acac)_2$, 97%], iron(0) pentacarbonyl [$Fe(CO)_5$, 99.99+%], copper(II) acetylacetonate [$Cu(acac)_2$, 97%], iron(III) acetylacetonate [$Fe(acac)_3$, 97%], indium(III) acetylacetonate [$In(acac)_3$, ≥99.99%], cadmium(II) chloride [$CdCl_2$, anhydrous, 99.99%], diphenyl diselenide [Ph_2Se_2, 97%], 1-octadecene [ODE, technical grade (90%)], oleylamine [OLAM, technical grade (≥70% primary amines)], and oleic acid [OLAC, technical grade (90%)] were purchased from Sigma-Aldrich. Solvents (hexanes and ethanol) were of analytical grade and purchased from Avantor-VWR. All chemicals were used as received without further purification.

4.2.2 General Safety Concerns

The synthetic methods in this report are done under air-free conditions at elevated temperatures using high boiling point solvents. As such care should be taken to ensure proper monitoring and handling. The safety data sheets for all chemicals used in the reactions should be

reviewed and proper personal protective equipment should be used. These reactions have the potential to evolve toxic gases and as such should be handled in a properly functioning fume hood.

4.2.3 Standard Reaction Vessel Setup

Each of the following procedures utilize a standard Schlenk line setup. Each three-necked, round-bottom was equipped with a magnetic, Teflon-coated stir bar, reflux condenser, angled adapter, and thermocouple and adapter. The temperature was controlled by a JKEM Gemini programmable temperature controller and LabGlass heating mantles.

4.2.4 Synthesis of 8 nm Pt Nanoparticle Seeds

Using a modification of a reported procedure,[35] 100 mg (0.25 mmol) of $Pt(acac)_2$, 10 mL of 1-octadecene, 1 mL OLAM, and 1 mL OLAC were added to the main reaction flask. The mixture was placed under vacuum and degassed at 120 °C for 30 minutes. While the Pt–precursor solution was degassing, to a 20 mL scintillating vial was charged 1.8 mL of ODE. This mixture was placed under vacuum and degassed at room temperature for 30 minutes. The main reaction vessel and the scintillating vial were then placed under Ar. 200 µL of $Fe(CO)_5$ was added by needle and syringe under Ar to the scintillating vial. The vial was then briefly sonicated in a bath sonicator to mix the solution. 100 µL of the Fe–precursor was then injected into the main reaction flask. The reaction mixture was then heated to 200 °C and held at this temperature for 1 hr. The flask was then removed from the heating mantle and cooled to <60 °C then the formed particles were precipitated by adding isopropanol. The precipitated particles were poured into two centrifuge tubes and then centrifuged at 15921 RCF for 3 minutes. The supernatant was decanted then the particles were suspended in approximately 5 mL of hexanes. 30 mL of isopropanol was added to each of the centrifuge tubes then the centrifugation process was repeated. The washed particles were suspended in hexanes and stored for later.

4.2.5 Synthesis of Pt–$CuMSe_2$ Hybrid Nanoparticles (M = Fe, In)

Using modifications of reported procedures,[34] 20 mg of Pt nanoparticle seeds suspended in hexanes, 65 mg (0.25 mmol) of $Cu(acac)_2$, 80 mg (0.25 mmol) Ph_2Se_2, and 8 mL OLAM were charged to the main reaction flask. A second flask was charged with 0.25 mmol of the appropriate metal acetylacetonate (88, or 103 mg for iron, or indium salt, respectively) and 4 mL of OLAM. The reaction mixtures were degassed at 70 °C for 30 minutes then at 140 °C for an additional 30 minutes all under vacuum. After degassing, the reaction mixtures were placed under an argon blanket, the main reaction flask was heated to 250 °C. When the main reaction flask reached 200 °C, the contents of the second flask were quickly injected into the main reaction mixture. After reaching 250 °C, the reaction mixture was held at that temperature for 60 minutes. After the reaction was done, the flask was removed from the heating mantle and allowed to cool to room temperature naturally. Upon reaching 80 °C, 2 mL of OLAC was injected into the main reaction flask to better ligate the synthesized particles. The particles were precipitated by addition of isopropanol then poured into centrifuge tubes. The particles were centrifuged at 15921 RCF for 3 minutes. The supernatant was decanted then the particles were suspended in approximately 5 mL of hexanes and 30 mL of isopropanol was added. The particles were centrifuged again at 15921 RCF for 3 minutes. The supernatant was again discarded then the particles were suspended in approximately 5 mL of hexanes and stored for further characterization.

4.2.6 Synthesis of Pt–$Cu_{2-x}Se$ Nanoparticle Seeds

Using our previously reported procedure,[36] 65.4 mg (0.25 mmol) of $Cu(acac)_2$, 40 mg (0.25 mmol) of Ph_2Se_2, 10 mL of OLAM, and 20 mg of Pt nanoparticles suspended in hexanes were added to the main reaction flask. This flask was heated to 60 °C under vacuum for 30 minutes then 140 °C for an additional 30 minutes. The reaction mixture was placed under an Ar blanket then heated to 215 °C and held at that temperature for 3 minutes. After the reaction was completed, the reaction vessel was removed from the heating mantle and rapidly cooled using air flow. Once the

temperature reached 100 °C, the flask was placed in a room temperature water bath to quickly cool the reaction to room temperature. The particles were then collected into centrifuge tubes and precipitated with isopropanol. The particles were then centrifuged at 15921 RCF for 3 minutes. The supernatant was discarded and the particles were suspended in approximately 5 mL of hexanes. The particles were precipitated again with isopropanol and centrifuged at 15921 RCF for 3 minutes. The supernatant was discarded again. The particles were suspended in approximately 5 mL of hexanes and stored for further use.

4.2.7 Cation Exchange Reaction with Cadmium

Using previously established procedures,[37] 0.5 mmol of a cadmium (II) chloride salt (90 mg $CdCl_2$), 3 mL OLAM, and 7 mL of ODE were added to the main reaction flask. The reaction mixture was placed under vacuum and heated to 120 °C for 30 minutes. The reaction mixture was then placed under Ar flow and heated to 180 °C. The reaction mixture was held under flow for 30 minutes. The reaction solution was then cooled to 150 °C and placed under an Ar blanket. 10 mg of Cu_2Se nanoparticle seeds and 3 mL of TOP were added to a 20 mL scintillating vial under Ar. The vial was quickly cycled between vacuum and Ar three times. The particles were sonicated briefly to resuspend then quickly injected into the main reaction flask. The particles were left to react for 30 minutes. After the reaction was completed the reaction flask was placed in a room temperature water bath to rapidly cool. The reaction solution was quickly added to centrifuge tubes and precipitated with chilled isopropanol. The particles were centrifuged at 15921 RCF for 3 minutes, then the supernatant was discarded. The precipitated particles were then suspended in approximately 5 mL of hexanes. The particles were precipitated with isopropanol and centrifuged again. The supernatant was then discarded and the particles were suspended in approximately 5 mL of hexanes for further characterization.

4.2.8 Cation Exchange Reaction with Iron

To synthesis the iron precursor solution, 25 mg (0.15 mmol) of $FeCl_3$, 3 mL OLAM, and 7 mL of ODE were added to the main reaction flask. The reaction mixture was placed under vacuum and heated to 120 °C for 30 minutes. The reaction mixture was then placed under Ar flow and heated to 200 °C. The reaction was kept under flow until the dark orange solution turned colorless and transparent (1-2 hr). Once the solution cleared, the temperature was cooled to 150 °C and placed under an Ar blanket. 10 mg of Cu_2Se nanoparticle seeds and 3 mL of TOP were added to a 20 mL scintillating vial under Ar. The vial was quickly cycled between vacuum and Ar three times. The particles were sonicated briefly to resuspend then quickly injected into the main reaction flask. The particles were left to react for 30 minutes. After the reaction was completed the reaction flask was placed in a room temperature water bath to rapidly cool. The reaction solution was quickly added to centrifuge tubes and precipitated with chilled isopropanol. The particles were centrifuged at 15921 RCF for 3 minutes, then the supernatant was discarded. The precipitated particles were then suspended in approximately 5 mL of hexanes. The particles were precipitated with isopropanol and centrifuged again. The supernatant was then discarded and the particles were suspended in approximately 5 mL of hexanes for further characterization.

4.2.9 Materials Characterization

Transmission electron microscopy (TEM) images were collected on a FEI Tecnai G2 20 XTWIN with a LaB_6 filament operating at 200 kV. High-angle annular dark field scanning transmission electron microscopy (HAADF-STEM) images, STEM energy dispersive X-ray spectroscopy (STEM-EDS) element maps, and selected area electron diffraction (SAED) patters were collected on a FEI Talos F200x Field Emission S/TEM at an accelerating voltage of 200 kV. ImageJ software was used to analyze the SAED images. Bruker ESPIRIT 2 software was used to interpret the STEM-EDS element map data. Powder X-ray diffraction (XRD) data were collected on a Malvern Panalytical Empyrean III theta-theta diffractometer equipped with a PIXcel3D

detector operated under Cu Kα radiation. Crystal structure and powder diffraction simulations were performed using CrystalMaker and CrystalDiffract from CrystalMaker Software Ltd., Oxford, England.

4.3 Results and Discussion

4.3.1 Seeded Growth of $CuInSe_2$ and $CuFeSe_2$ on Pt Nanoparticles

Platinum nanoparticle seeds were synthesized by reacting $Pt(acac)_2$ with $Fe(CO)_5$ in ODE, OLAM, and OLAC at 200 °C, as described in detail in the Experimental Section. These preformed nanoparticles, Figure 4.2, were then introduced for the growth conditions for $CuInSe_2$ and $CuFeSe_2$ domains. Briefly, 10 mg of Pt nanoparticles were added to a solution of $Cu(acac)_2$ and OLAM. This solution was degassed under vacuum then heated to 250 °C. When the reaction reached 210 °C, a precursor solution containing stoichiometric quantities of either $Fe(acac)_3$ or $In(acac)_3$ dissolved in OLAM. The reaction was then held at 250 °C for 60 minutes. XRD of the resulting particles, seen in Figure 4.3, show patterns which are a match for wurtzite $CuInSe_2$ and eskebornite $CuFeSe_2$. The lack of peaks associated with Pt may be due to low numbers of Pt seeds relative to the formed ternary chalcogenides. High-angle annular darkfield–STEM (HAADF-STEM) images of the Pt–$CuInSe_2$ hybrid nanoparticles, seen in Figure 4.4a, shows the higher contrast Pt seeds surrounded

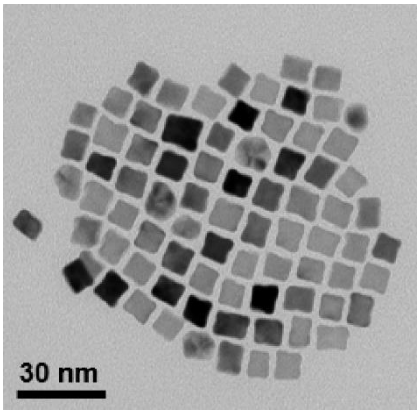

Figure 4.2: TEM image of Pt nanoparticle seeds utilized in the synthesis of ternary copper chalcogenide hybrid nanoparticles.

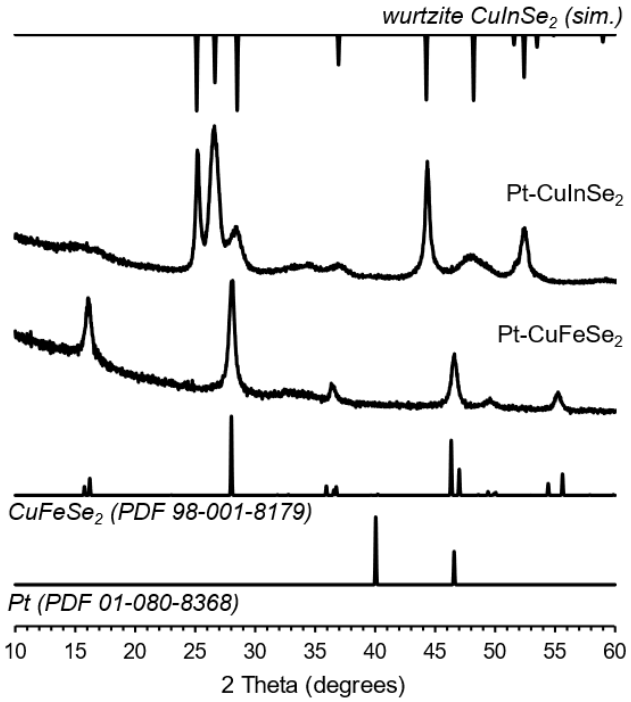

Figure 4.3: XRD patterns of synthesized Pt–$CuInSe_2$ and Pt–$CuFeSe_2$ nanoparticles. The simulated pattern for wurtzite $CuInSe_2$ was created using lattice parameters from ref 38.

by lower contrast domains corresponding to $CuInSe_2$. The EDS maps of the Pt–$CuInSe_2$ particles, Figure 4.4b–f, show colocalization of Cu, In, and Se signal corresponding to the lower contrast regions in the HAADF image. Standardless quantification of the EDS spectrum, Figure 4.4g, shows that these particles have a Cu:In ratio of 1.07 which is within instrumental error of the nominal 1:1 stoichiometry. These particles appear to take on a core-shell structure versus the more commonly observed dumbbell morphology of heterodimer nanoparticles, though this could be a consequence of the imaging method. Knowing whether or not the Pt domain is exposed is important if utilizing similar heterostructures for catalytic applications.[39, 40] To verify this observation, a line scan (indicated pathway shown in Figure 4.4a) was done on the collected EDS maps with the results seen in Figure 4.4h. If the particles had a core–shell morphology, there would be a dip in the number of Cu and In counts corresponding to a rise in Pt counts.[41] The line scan of one of the Pt–$CuInSe_2$ nanoparticles showed an independent relationship between Pt counts and Cu/In counts, with Cu/In

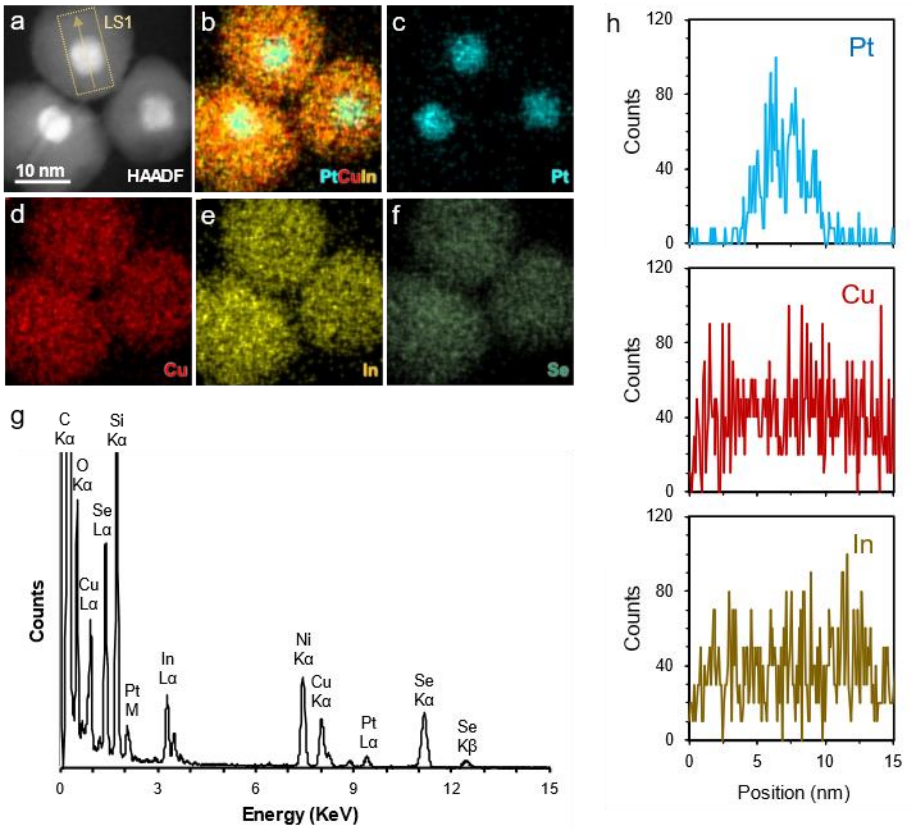

Figure 4.4: HAADAF-STEM images and accompaning EDS maps of Pt–$CuInSe_2$ (a–f) heterodimer nanoparticles. The STEM-EDS maps correspond to Pt Mα (cyan), Cu Kα (red), In Lα (yellow), and Se Kα (green). EDS spectrum of synthesized nanoparticles (g), with assigned X-ray emission lines. Ni signal comes from the grid material. The line scan depicted in panel a can be observed in panel h.

counts remaining consistent despite the sharp increase in Pt counts. This result would imply a typical hybrid morphology instead of the observed core–shell geometry.

A similar analysis was done for the synthesized Pt–$CuFeSe_2$ nanoparticles. HAADF–STEM images show a similar morphology to that of the $CuInSe_2$ hybrids, though they appear comparably more faceted, seen in Figure 4.5a. EDS maps (Figure 4.5b–f, h) show coincidence of Cu, Fe, and Se. However, the EDS showed excess Fe signal not coincident with the hybrid particles, but is coincident with greater oxygen signal indicating the formation of amorphous FeO_x. Since this oxide impurity would bias the quantification, another nanoparticle was chosen to determine the stoichiometry. Quantification of the spectrum, seen in Figure 4.5g, indicates a Cu:Fe ratio of 1.18.

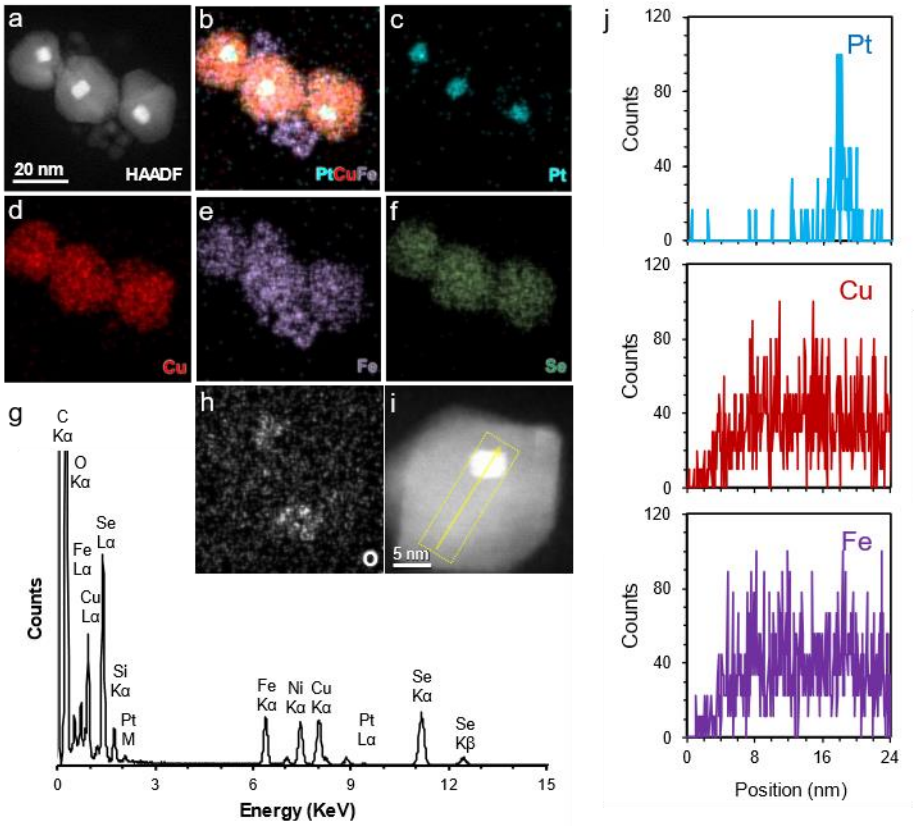

Figure 4.5: HAADAF-STEM images and accompaning EDS maps of Pt–$CuFeSe_2$ (a–f, h) heterodimer nanoparticles. The STEM-EDS maps correspond to Pt Mα (cyan), Cu Kα (red), Fe Kα (violet), Se Kα (green), and O Kα (grey). (g) EDS spectrum of hybrid nanoparticle depicted in panel i, with assigned X-ray emission lines. It should be noted that the Ni signal comes from the grid material. Due to iron oxide contamination, another hybrid particle was chosen for the line scan (i). The line scan depicted in panel i can be observed in panel j.

Though this enrichment in Cu could be due to instrumental error, the observation of nonincorporated Fe lends weight to the observed Cu enrichment being real. A similar line scan analysis was done on a Pt–$CuFeSe_2$ heterodimer, seen in Figure 4.5j. Again, the Pt and Cu/Fe counts appear to be independent with no apparent indicators of core–shell geometry. Taken all together, we have demonstrated the formation of $CuInSe_2$ and $CuFeSe_2$ heterodimers by seeded growth on Pt nanoparticles. To better understand how we utilize these nanoparticles into more complex systems, it would be prudent to understand how these particles form in solution.

4.3.2 Insights into the Formation of $CuInSe_2$ and $CuFeSe_2$ Domains

In order to predictably incorporate new materials into the single particle domains it imperative to understand how these materials nucleate and grow. In synthesizing $CuInSe_2$, Tappan et al. showed that the reaction proceeds through a multistep pathway with the initial nucleation of $Cu_{2-x}Se$ nanoparticles which undergo an *in situ* cation exchange reaction.[34] Similarly, Park et al. rationalized the formation of Cu_5FeS_4 nanosandwiches from $Cu_{2-x}S$ sheet by an *in situ* cation exchange reaction.[42] However, Wang et al. concluded that the formation of $CuFeSe_2$ nanocubes occurred through spontaneous formation without an intermediate step.[30] They rationalized that reagent reactivity needed to be compatible for $CuFeSe_2$ synthesis. These competing hypotheses highlight the complexity of nanoparticle synthesis and the difficulty of probing these reaction mechanisms. In the case of $CuInSe_2$, Tappan et al. showed that the pseudo hexagonal anion sublattice in their isolated intermediates directed the formation of wurtzite $CuInSe_2$.[34] We have reported a similar synthesis for the formation of $Cu_{2-x}Se$ nanoparticles which have a hexagonal sublattice.[36] We hypothesized that cation exchange on these particles would also produce wurtzite metal chalcogenides. Nanoparticles of weissite $Cu_{2-x}Se$ were synthesized by the method from Chapter 3 and then subjected to a cadmium exchange. Analysis by XRD shows that the weissite $Cu_{2-x}Se$ nanoparticles were transformed into the wurtzite CdSe polytype, seen in Figure 4.6a, which is the metastable phase of CdSe. The related crystal structures of the weissite starting material and wurtzite exchange product, seen in Figure 4.6b. The crystallographic features such as the hexagonal Se sublattice. The Cu cations in weissite occupy the tetrahedral and trigonal interstitial sites while the cations in wurtzite occupy the tetrahedral sites. This result confirms that weissite phase can

template wurtzite making the logical extension to $CuInSe_2$ and Pt–$Cu_{2-x}Se$ heterodimers formed during the synthesis of Pt–$CuInSe_2$.

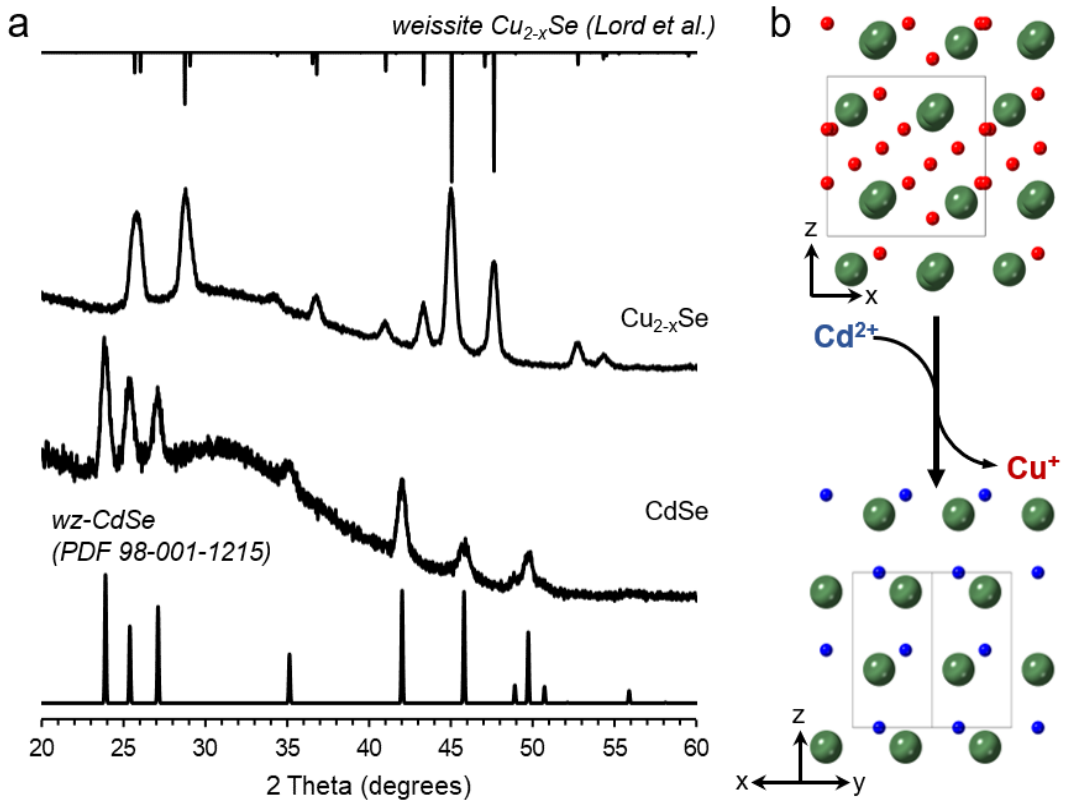

Figure 4.6: (a) XRD patterns of synthesized weissite-like $Cu_{2-x}Se$ nanoparticles and wurtzite CdSe nanoparticles synthesized by post-synthetic cadmium cation exchange. Simulated pattern for weissite-like $Cu_{2-x}Se$ was created using lattice parameters and atomic coordinates in ref. 36. (b) Crystal structures of the starting $Cu_{2-x}Se$ nanoparticles and the wurtzite exchange product.

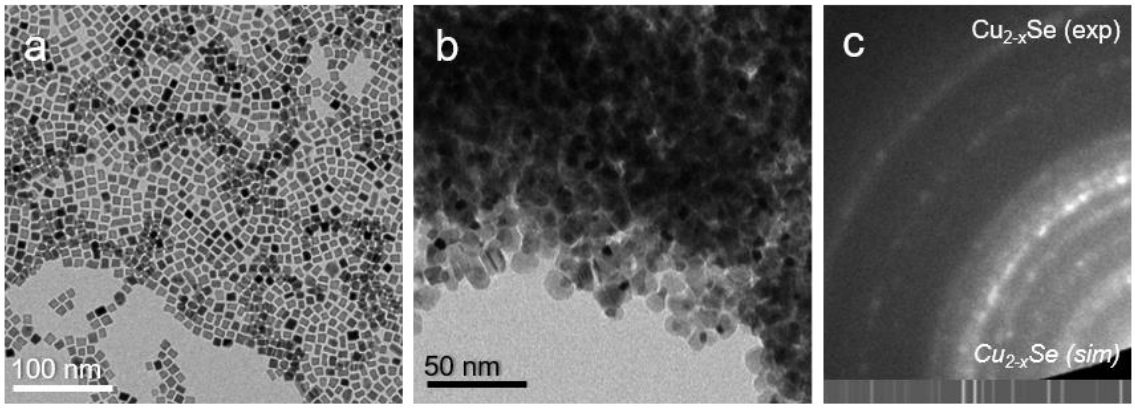

Figure 4.7: TEM images of Pt seeds (a) and Pt–$Cu_{2-x}Se$ heterodimers (b). Selected area electron diffraction pattern (c) of the Pt–$Cu_{2-x}Se$ heterodimers with simulated pattern.

To test whether or not these particles would nucleate onto Pt seeds, we exposed preformed Pt nanoparticles to the growth conditions for our synthesis of weissite-like $Cu_{2-x}Se$ nanoparticles. The reaction formed Pt–$Cu_{2-x}Se$ heterodimers as observed in the TEM images with lighter contrast regions corresponding to $Cu_{2-x}Se$ and darker contrast with the Pt seeds, Figure 4.7b. Additionally, the electron diffraction pattern, Figure 4.7c, matches that of simulated weissite-like $Cu_{2-x}Se$. Taken together, we can infer that the likely intermediate $Cu_{2-x}Se$ would nucleate and grow on Pt seeds and retain the trigonal crystal structure. This would be important for validating the formation of wurtzite $CuInSe_2$ by an *in situ* cation exchange reaction.

To test the formation of $CuFeSe_2$ by cation exchange, we put our $Cu_{2-x}Se$ nanoparticles through a post-synthetic iron exchange reaction. Recently, Sharp et al. reported an exchange protocol for iron exchange on $Cu_{2-x}S$ nanoparticles .[44] However, since their protocol is done at room temperature using different neocuproine instead of TOP to drive the reaction. We chose to modify

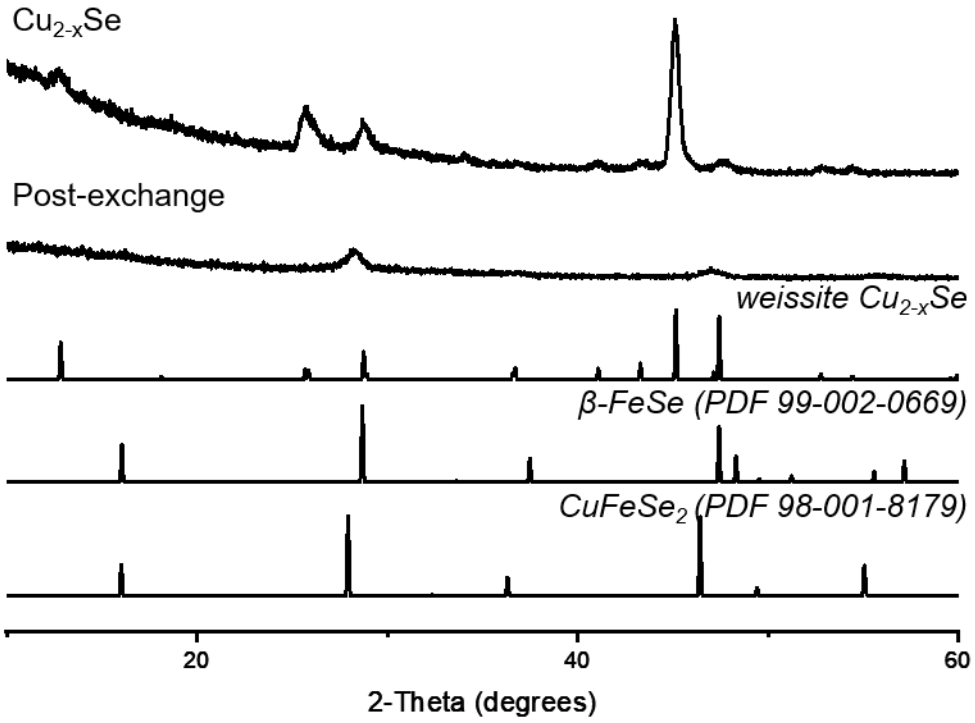

Figure 4.8: XRD patterns of the weissite-like $Cu_{2-x}Se$ nanoparticle and the post-exchanged particles. Parameters for the simulated pattern of weissite-like $Cu_{2-x}Se$ were taken from ref 36.

the cation exchange procedure used for the cadmium exchange as a closer approximation of the conditions we used for $CuFeSe_2$ synthesis. During the formation of the iron exchange solution, we observed a color change in the exchange solution from dark orange to clear and colorless during extended time under flow at elevated temperatures. When we injected our $Cu_{2-x}Se$ nanoparticles into this exchange solution, we observed the successful exchange with iron to form the β-FeSe phase as characterized by XRD, seen in Figure 4.8. While the patterns for $CuFeSe_2$ and β–FeSe appear similar, the peak at 48 degrees better matches the peaks in the FeSe reference pattern. Crystal structure diagrams of the starting weissite-like $Cu_{2-x}Se$ and the resulting β–FeSe post-exchange product, Figure 4.9a. We can see the distorted hexagonal anion sublattice is preserved from $Cu_{2-x}Se$ to the β–FeSe. The β–FeSe is structurally related to the $CuFeSe_2$ phase, Figure 4.9b, where $CuFeSe_2$ can be approximated by two FeSe unit cells. TEM images, seen in Figure 4.10a and b, of

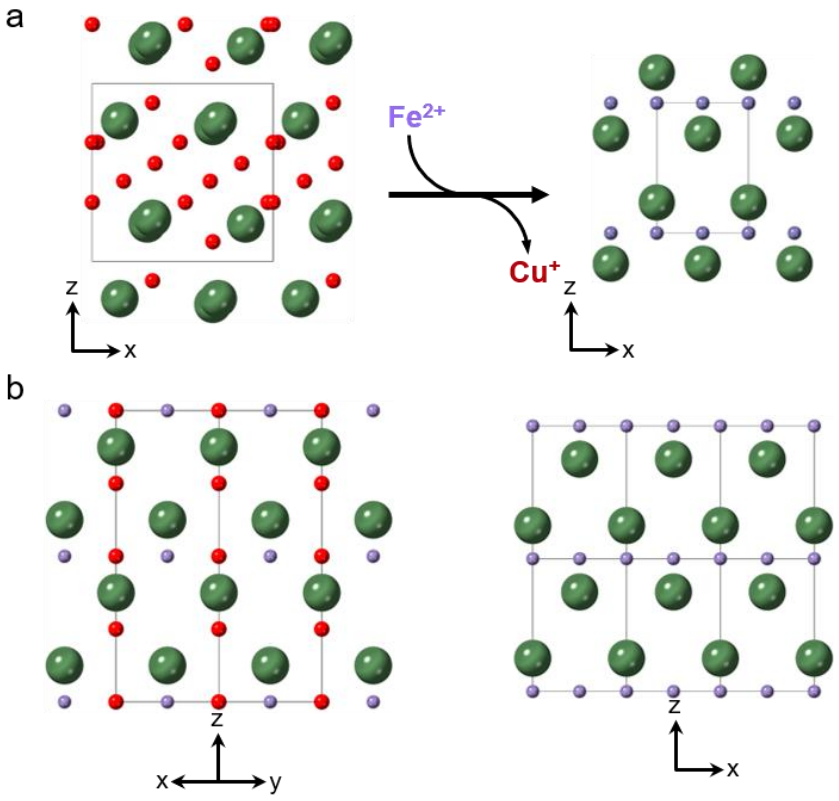

Figure 4.9: (a) Crystal structures of the starting weissite $Cu_{2-x}Se$ material and β–FeSe post-exchange product. (b) Crystal structures of eskebornite $CuFeSe_2$ and β–FeSe.

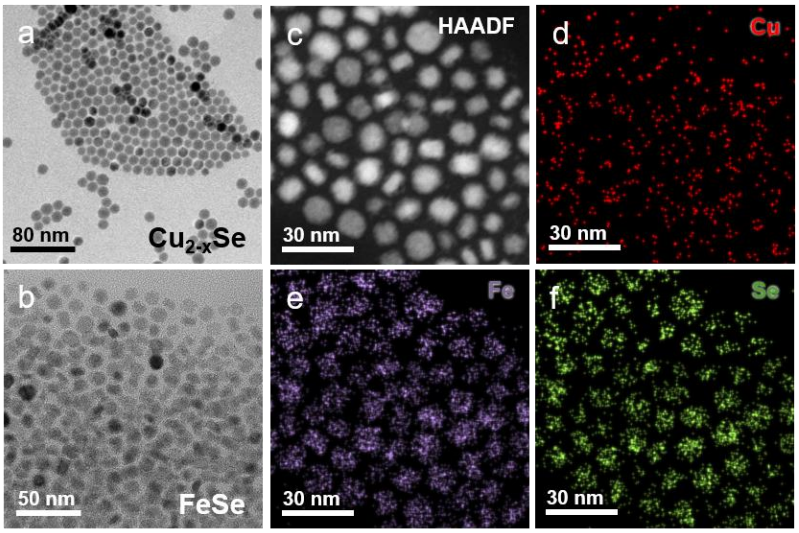

Figure 4.10: TEM images of the (a) pre-exchanged $Cu_{2-x}Se$ particles and the (b) post-exchanged FeSe nanoparticles. HAADF-STEM image (c) and accompanying EDS maps (d–f) of the FeSe nanoparticles formed by post-synthetic cation exchange with Fe. The EDS maps correspond to Cu Kα (red), Fe Kα (purple), and Se Kα (green).

the pre- and post-exchanged particles show some small amounts of particle etching most likely from TOP and adventitious oxygen introduced during particle injection.[43] EDS maps of the particles post exchange show colocalization of Fe and Se signals corresponding to a Fe:Se ratio of 1.36 and a Cu:Fe ratio of 0.08. This enhancement of Fe beyond the nominal stoichiometry could be due to excess Fe precursor which did not wash off in the reaction or an oxide shell. By tuning the Fe to Cu stoichiometry used in the exchange reaction it may be possible to obtain $CuFeSe_2$ this way. Williams et al. showed that Cu is soluble up 20–30% in bulk FeSe and at higher Cu concentrations a phase change to the ternary $CuFeSe_2$.[45] While this reaction is far from optimized, it demonstrates that $Cu_{2-x}Se$ particles can undergo a cation exchange reaction to form an iron selenide phase. Additionally, this is the first demonstration of a moderate temperature cation exchange reaction on $Cu_{2-x}Se$ nanoparticles using iron though more experiments are needed to refine this chemistry to enable tuning between FeSe and $CuFeSe_2$.

To probe whether $CuFeSe_2$ forms by an *in situ* cation exchange reaction, we took preformed $Cu_{2-x}Se$ nanoparticles and subjected them to the conditions by which we normally grew

Pt–$CuFeSe_2$ heterodimers except without $Cu(acac)_2$. An aliquot series of the reaction, Figure 4.11, showed that at no step in the reaction was there an obvious transition from weissite $Cu_{2-x}Se$ to $CuFeSe_2$. There was no obvious overlapping signal between Cu, Fe, and Se. Instead, we only observed iron signal corresponding to the individual iron containing particles which are most likely

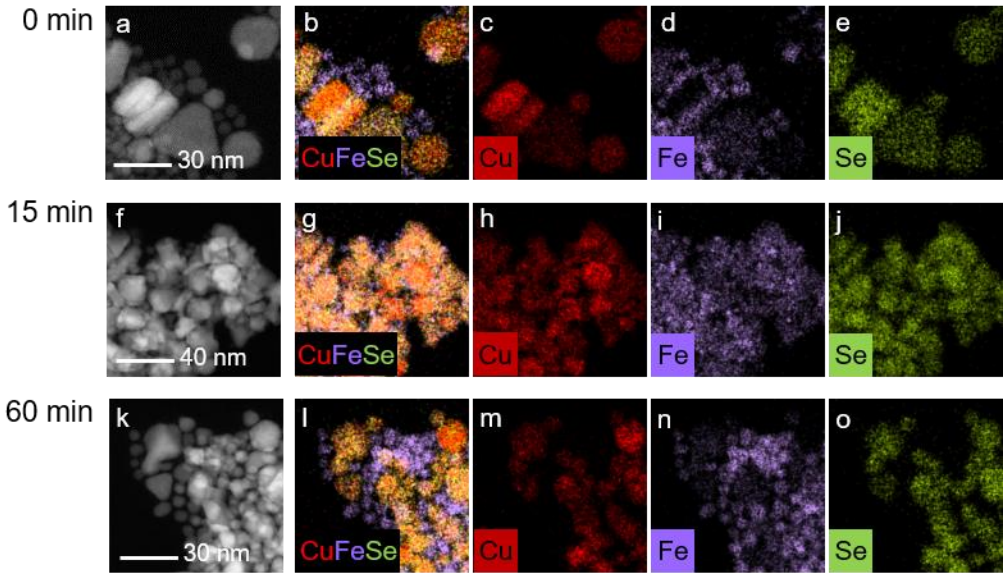

Figure 4.11: HAADF-STEM images (a, f, k) and accompanying EDS maps (b–e, g–j, l–o) of aliquot series taken during the attempted *in situ* cation exchange reaction of $Cu_{2-x}Se$ nanoparticles with iron.

iron oxide which formed when aliquots were taken. This doesn't necessarily rule out an *in situ* cation exchange reaction as the synthetic pathway for $CuFeSe_2$ formation, just that under these reaction conditions there is not the same thermodynamic driving force as the traditional cation exchange reaction when the particles are already formed. When the particles are forming as incomplete intermediates, the interplay between temperature and reagent reactivity may allow for an *in situ* cation exchange process though the complicated nature of probing particle formation at these temperatures pose a significant challenge.

4.3.3 Simultaneous Nucleation of $CuInSe_2$ and $CuFeSe_2$ Nanocrystals on Pt

The synthesis of heterostructured nanoparticles of increasing complexity has largely been done by means of successive growth reactions with formed hybrid nanoparticles being isolated and

cleaned between each reaction. This process is similar to the multistep synthetic reactions observed in organic synthesis.[46, 47] While this methodology is effective, it does not readily lend itself to the rapid discovery of new heterostructures. Combining the growth reactions of multiple synthetically compatible materials in a single pot has the potential of pushing the field forward and providing another avenue for synthetic discovery. Another advantage of this approach to hybrid nanoparticle synthesis is morphological purity and yield is not necessary. The observation of multiple different hybrid subpopulations can provide greater insight than single heterostructure formation alone. Since the methods we used to synthesize $CuInSe_2$ and $CuFeSe_2$ are identical and thus chemically

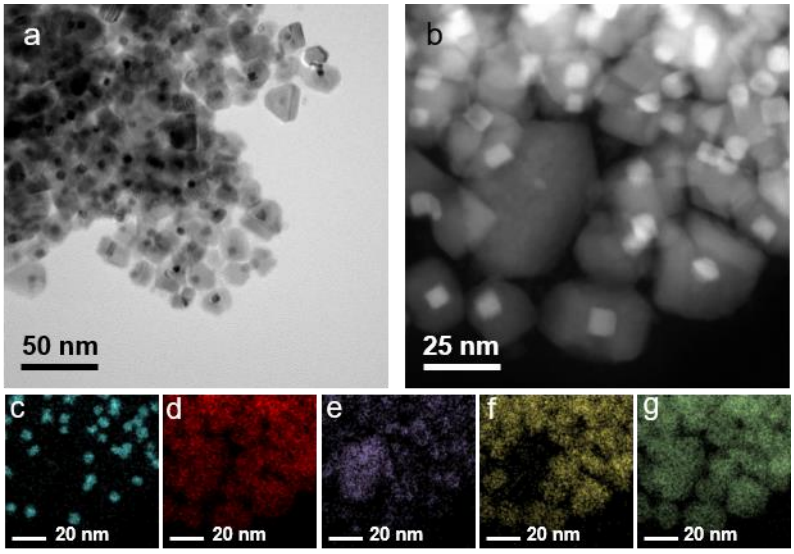

Figure 4.12: TEM image (a), HAADF-STEM image (b), and corresponding EDS maps (c–g) for the simultaneous nucleation of $CuInSe_2$ and $CuFeSe_2$. The EDS maps correspond to Pt M (cyan), Cu Kα (red), Fe Kα (violet), In Lα (yellow), and Se Kα (green).

compatible, they represent a useful model system to attempt the one-pot synthesis of heterostructured $CuInSe_2$–Pt–$CuFeSe_2$ nanoparticles. Briefly, we utilized the same method for synthesizing the individual ternary selenide domains but instead injected a precursor solution containing equivalent molar amounts of $Fe(acac)_3$ and $In(acac)_3$. The resulting heterostructures, seen in Figure 4.12, were not what we expected. Instead of co-nucleating $CuInSe_2$ and $CuFeSe_2$ domains on Pt, we only observed Pt–$CuInSe_2$ heterodimer formation alongside some $CuFeSe_2$ formation. The TEM image, Figure 4.12a, shows a number of hybrid nanoparticles which have

agglomerated, either during the reaction or during particle cleaning. In spite of the aggregation, heterodimer formation is clear with particles resembling those observed during the regular heterodimer formation. EDS maps, Figure 4.12c–g, show overlapping Cu, In, and Se signal coincident with Pt signals. There is a fair amount of Fe signal, though particle aggregation obfuscates the assignment of this signal to the heterodimers. The lone non-heterostructured particle observed in the HAADF image, Figure 4.12b, does show a distinct lack of coincident In signal only possessing overlapping Cu, Fe, and Se signal. Quantification of the EDS signal from the few lone heterodimers gives an average Cu:In ratio of 1.31 and an average Fe:Cu ratio of 0.12. This rather large deviation from the previously observed stoichiometry could be attributable to the relatively low signal used in the quantification or coincidence with other particles. To better deconvolute this result, it would be advantageous to synthesize particles which are better dispersed such as using a more strongly binding ligand such as oleic acid.

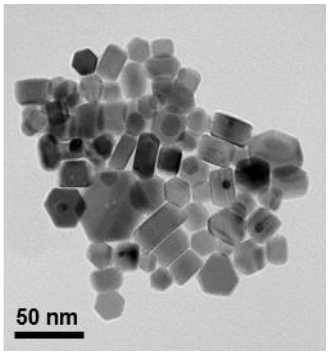

Figure 4.13: TEM image of the simultaneous synthesis of $CuInSe_2$ and $CuFeSe_2$ in the presence of Pt nanoparticles and oleic acid.

Utilizing oleic acid in the simultaneous synthesis of $CuInSe_2$ and $CuFeSe_2$ allowed for more regular particle formation, as seen in Figure 4.13. Most of the observed particles take on hexagonal platelet morphologies. There is less heterodimer formation during this synthesis though this could be due to insufficient seed crystals in solution. Analysis by STEM-EDS, Figure 4.14, shows particles which are primarily Cu, In, and Se containing giving reasonable evidence to $CuInSe_2$ formation. Interestingly, there doesn't appear to be any obvious $CuFeSe_2$ heterodimer or

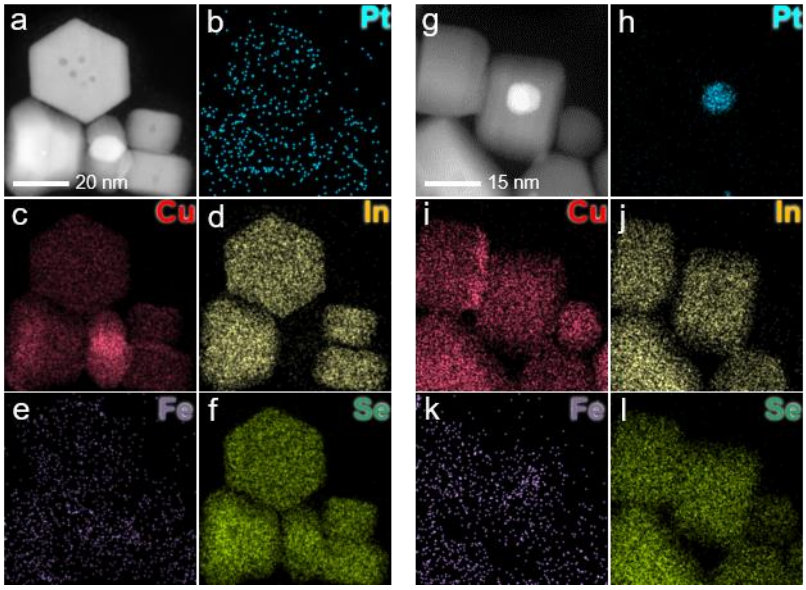

Figure 4.14: HAADF-STEM images (a, g) and accompanying EDS maps (b–f, h–l) corresponding to the simultaneous nucleation and growth of $CuInSe_2$ and $CuFeSe_2$ on Pt nanoparticle seeds. The EDS maps correspond to Pt M (cyan), Cu Kα (red), In Lα (yellow), Fe Kα (violet), and Se Kα (green).

$CuFeSe_2$ particles. Oleic acid may have affected the reactivities of the $CuFeSe_2$ precursors arresting particle formation under the prescribed conditions. An additional observation was a residual $Cu_{2-x}Se$ particles, Figure 4.14c,f, i, and l, which did not react with either the indium nor iron precursors. Interestingly, on some of the $CuInSe_2$ particles, there are regions which do not have overlapping Cu and In signals. This could imply that the oleic acid slowed the rate of indium exchange in the preformed particles. While somewhat circumstantial, this observation could validate the synthetic pathway for $CuInSe_2$ formation. Further experiments may show an exchange front progressing through the particles during their formation. Taken together, these observations point to competing processes in simultaneous domain formation in multicomponent hybrid nanoparticles synthesis. $CuInSe_2$ undergoes a stepwise nucleation and *in situ* cation exchange reaction while $CuFeSe_2$ undergoes a direct seeded nucleation. Though $CuInSe_2$ forms through a multistep process, the rate at which is forms appears faster than the nucleation of $CuFeSe_2$. The faster process dominates heterodimer formation as the Pt seeds are used up in $CuInSe_2$ formation before $CuFeSe_2$ can form.

4.4 Conclusions

In this chapter, I have shown the synthesis of Pt–$CuInSe_2$ and Pt–$CuFeSe_2$ hybrid nanoparticles. Using weissite-like $Cu_{2-x}Se$ nanoparticles, I have validated the formation of wurtzite type metal chalcogenides by cation exchange and demonstrated a low temperature cation exchange reaction on weissite-like $Cu_{2-x}Se$ to give β-FeSe. Using preformed Pt–$Cu_{2-x}Se$ nanoparticles as seeds for $CuFeSe_2$ syntheses, we found that iron does not undergo an *in situ* cation exchange reaction instead most likely favoring a spontaneous nucleation reaction. When attempting the simultaneous nucleation of $CuInSe_2$ and $CuFeSe_2$, we did not observe heterotrimer particle formation as only Pt–$CuInSe_2$ heterodimers were observed. When utilizing oleic acid in the reaction, we observed no $CuFeSe_2$ formation and the partial formation of $CuInSe_2$ showing incomplete transformation from $Cu_{2-x}Se$ to $CuInSe_2$. We concluded that there were competitive reaction pathways during the simultaneous synthesis, *in situ* cation exchange and direct nucleation, of which the *in situ* cation exchange being faster. Insights such as these are crucial to understanding the competitive processes involved in hybrid nanoparticle formation and the formation of other ternary metal chalcogenide nanoparticles.

4.5 Acknowledgements

This work was supported by the U.S. National Science Foundation under Grant 1707830. TEM/STEM imaging, EDS mapping, X-ray diffraction were performed at the Materials Characterization Lab of the Penn State Materials Research Institute.

4.6 References

(1) Zhou, M.; Wang, H.; Elnabawy, A. O.; Hood, Z. D.; Chi, M.; Xiao, P.; Zhang, Y.; Mavrikakis, M.; Xia, Y. Facile One-Pot Synthesis of Pd@Pt_{1L} Octahedra with Enhanced Activity and Durability toward Oxygen Reduction. *Chem. Mater.* **2019**, *31*, 1370–1380.

(2) Cathcart, N.; Murshid, N.; Campbell, P.; Kitaev, V. Selective Plasmonic Sensing and Highly Ordered Metallodielectrics via Encapsulation of Plasmonic Metal Nanoparticles with Metal Oxides. *ACS Appl. Nano Mater.* **2018**, *1*, 6514–6524.

(3) Deka, K.; Guleria, A.; Kumar, D.; Biswas, J.; Lodha, S.; Kaushik, S. D.; Choudhary, S. A.; Dasgupta, S.; Deb, P. Janus Nanoparticles for Contrast Enhancement of T_1–T_2 Dual Mode Magnetic Resonance Imaging. *Dalton Trans.* **2019**, *48*, 1075–1083.

(4) Oh, N.; Kim, B. H.; Cho, S.-Y.; Nam, S.; Rogers, S. P.; Jiang, Y.; Flanagan, J. C.; Zhai, Y.; Kim, J.-H.; Lee, J. Yu, Y.; Cho, Y.H.; Hur, G.; Zhang, J.; Trefonas, P.; Rogers, J.A.; Shim, M. Double-Heterojunction Nanorod Light-Responsive LEDs for Display Applications. *Science* **2017**, *355*, 616–619.

(5) Fagan, A.M.; Jeffries, W.R.; Knappenberger Jr, K.L.; Schaak, R.E. Synthetic Control of Hot-Electron Thermalization Efficiency in Size-Tunable Au–Pt Hybrid Nanoparticles. *ACS Nano* **2021**, *15*, 1378–1387.

(6) Pellegrino, T.; Fiore, A.; Carlino, E.; Giannini, C.; Cozzoli, P. D.; Ciccarella, G.; Respaud, M.; Palmirotta, L.; Cingolani, R.; Manna, L. Heterodimers Based on $CoPt_3$-Au Nanocrystals with Tunable Domain Size. *J. Am. Chem. Soc.* **2006**, *128*, 6690–6698.

(7) Huang, J.; Mensi, M.; Oveisi, E.; Mantella, V.; Buonsanti, R. Structural Sensitivities in Bimetallic Catalysts for Electrochemical CO_2 Reduction Revealed by Ag-Cu Nanodimers. *J. Am. Chem. Soc.* **2019**, *141*, 2490–2499.

(8) Wang, C.; Yin, H.; Dai, S.; Sun, S. A General Approach to Noble Metal-Metal Oxide Dumbbell Nanoparticles and Their Catalytic Application for CO Oxidation. *Chem. Mater.* **2010**, *22*, 3277–3282.

(9) Gordon, T. R.; Schaak, R. E. Synthesis of Hybrid Au-In_2O_3 Nanoparticles Exhibiting Dual Plasmonic Resonance. *Chem. Mater.* **2014**, *26*, 5900–5904.

(10) Varandili, S. B.; Huang, J.; Oveisi, E.; De Gregorio, G. L.; Mensi, M.; Strach, M.; Vavra, J.; Gadiyar, C.; Bhowmik, A.; Buonsanti, R. Synthesis of Cu/CeO_{2-x} Nanocrystalline Heterodimers with Interfacial Active Sites to Promote CO_2 Electroreduction. *ACS Catal.* **2019**, *9*, 5035–5046.

(11) Lord, R. W.; Holder, C. F.; Fenton, J. L.; Schaak, R. E. Seeded Growth of Metal Nitrides on Noble-Metal Nanoparticles To Form Complex Nanoscale Heterostructures. *Chem. Mater.* **2019**, *31*, 4605–4613.

(12) Hernández-Pagán, E. A.; Lord, R. W.; Veglak, J. M.; Schaak, R. E. Incorporation of Metal Phosphide Domains into Colloidal Hybrid Nanoparticles. *Inorg. Chem.* **2021**, *60*, 4278–4290.

(13) Balakrishnan, S. K.; Kamat, P. V. Au-$CsPbBr_3$ Hybrid Architecture: Anchoring Gold Nanoparticles on Cubic Perovskite Nanocrystals. *ACS Energy Lett.* **2017**, *2*, 88–93.

(14) Hodges, J. M.; Biacchi, A. J.; Schaak, R. E. Ternary Hybrid Nanoparticle Isomers: Directing the Nucleation of Ag on Pt-Fe_3O_4 Using a Solid-State Protecting Group. *ACS Nano* **2014**, *8*, 1047–1055.

(15) Buck, M. R.; Bondi, J. F.; Schaak, R. E. A Total-Synthesis Framework for the Construction of High-Order Colloidal Hybrid Nanoparticles. *Nat. Chem.* **2012**, *4*, 37–44.

(16) Chen, Y.; Shi, Z.; Feng, J.; Pang, B.; Yu, L.; Dong, L. Template synthesis of Ternary Hybrid Nanocrystals of CoS/Ag_2S-Fe_2O_3 with Near-Infrared Photoluminescence. *Microsc. Microanal.* **2019**, *25*, 2358–2359.

(17) Meekins, B. H.; Kamat, P. V. Role of Water Oxidation Catalyst IrO_2 in Shuttling Photogenerated Holes across TiO_2 Interface. *J. Phys. Chem. Lett.* **2011**, *2*, 2304–2310.

(18) Lim, Y. S.; Kwon, H.-S.; Jeong, J.; Kim, J. Y.; Kim, H.; Ko, M. J.; Jeong, U.; Lee, D.-K. Colloidal Solution-Processed $CuInSe_2$ Solar Cells with Significantly Improved Efficiency up to 9% by Morphological Improvement. *ACS Appl. Mater. Interfaces* **2014**, *6*, 259–267.

(19) Aldakov, D.; Lefrançois, A.; Reiss, P. Ternary and Quaternary Metal Chalcogenide Nanocrystals: Synthesis, Properties and Applications. *J. Mater. Chem. C* **2013**, *1*, 3756–3776.

(20) Shemesh, Y.; Macdonald, J. E.; Menagen, G.; Banin, U. Synthesis and Photocatalytic Properties of a Family of CdS-PdX Hybrid Nanoparticles. *Angew. Chem., Int. Ed*. **2011**, *50*, 1185–1189.

(21) Hernández-Pagán, E. A.; Leach, A. D. P.; Rhodes, J. M.; Sarkar, S.; Macdonald, J. E. A Synthetic Exploration of Metal–Semiconductor Hybrid Particles of $CuInS_2$. *Chem. Mater.* **2015**, *27*, 7969–7976.

(22) Witt, E.; Parisi, J.; Kolny-Olesiak, J. Selective Growth of Gold onto Copper Indium Sulfide Selenide Nanoparticles. *Z. Naturforsch., A: Phys. Sci*. **2013**, *68*, 398–404.

(23) Xu, Y.; Li, Q. Heterostructured CIGS–Au Nanoparticles: From Au–CIGS Side-by-Side Structure to Au-Core/CIGS-Shell Configuration. *Nanoscale* **2011**, *3*, 3238–3243.

(24) Dilsaver, P. S.; Reichert, M. D.; Hallmark, B. L.; Thompson, M. J.; Vela, J. Cu_2ZnSnS_4-Au Heterostructures: Toward Greener Chalcogenide-Based Photocatalysts. *J. Phys. Chem. C* **2014**, *118*, 21226–21234.

(25) Yu, X.; Shavel, A.; An, X.; Luo, Z.; Ibanez, M.; Cabot, A. Cu_2ZnSnS_4-Pt and Cu_2ZnSnS_4-Au Heterostructured Nanoparticles for Photocatalytic Water Splitting and Pollutant Degradation. *J. Am. Chem. Soc.* **2014**, *136*, 9236–9239.

(26) Ha, E.; Lee, L. Y. S.; Man, H. -W.; Tsang, S. C. E.; Wong, K. -Y. Morphology-Controlled Synthesis of Au/Cu_2FeSnS_4 Core–Shell Nanostructures for Plasmon-Enhanced Photocatalytic Hydrogen Generation. *ACS Appl. Mater. Interfaces* **2015**, *7*, 9072–9077.

(27) Rockett, A.; Birkmire, R. W. $CuInSe_2$ for Photovoltaic Applications. *J. Appl. Phys.* **1991**, *70*, 81–97.

(28) Ye, M.; Tang, R.; Ma, S.; Tao, Q.; Wang, X.; Li, Y.; Zhu, P. Electrical Transport Properties and Band Structure of $CuInSe_2$ under High Pressure. *J. Phys. Chem. C* **2019**, *123*, 20757–20763.

(29) Hamdadou, N.; Morsli, M.; Khelil, A.; Bernède, J. C. Fabrication of n-and p-Type Doped $CuFeSe_2$ Thin Films Achieved by Selenization of Metal Precursors. *J. Phys. D: Appl. Phys*. **2006**, *39*, 1042–1049.

(30) Wang, W.; Jiang, J.; Ding, T.; Wang, C.; Zuo, J.; Yang, Q. Alternative Synthesis of $CuFeSe_2$ Nanocrystals with Magnetic and Photoelectric Properties. *ACS Appl. Mater. Interfaces* **2015**, *7*, 2235–2241.

(31) Wu, N.; Li, Y.; Zeng, M.; Gao, J.; Tang, Y.; Zeng, Z.; Zheng, Y. Design of Chalcopyrite-Type $CuFeSe_2$ Nanocrystals: Microstructure, Magnetism, Photoluminescence and Sensing Performances. *J. Solid State Chem.* **2019**, *271*, 292–297.

(32) Jiang, X.; Zhang, S.; Ren, F.; Chen, L.; Zeng, J.; Zhu, M.; Cheng, Z.; Gao, M.; Li, Z. Ultrasmall Magnetic $CuFeSe_2$ Ternary Nanocrystals for Multimodal Imaging Guided Photothermal Therapy of Cancer. *ACS Nano* **2017**, *11*, 5633–5645.

(33) Zhang, Q.; Wang, J.; Jiang, Z.; Guo, Y.-G.; Wan, L.-J.; Xie, Z.; Zheng, L. J. Au–Cu Alloy Bridged Synthesis and Optoelectronic Properties of Au@$CuInSe_2$ Core–Shell Hybrid Nanostructures. *J. Mater. Chem.* **2012**, *22*, 1765–1769.

(34) Tappan, B. A.; Barim, G.; Kwok, J. C.; Brutchey, R. L. Utilizing Diselenide Precursors toward Rationally Controlled Synthesis of Metastable $CuInSe_2$ Nanocrystals. *Chem. Mater*. **2018**, *30*, 5704–5713.

(35) Wang, C.; Daimon, H.; Onodera, T.; Koda, T.; Sun, S. A General Approach to the Size- and Shape-Controlled Synthesis of Platinum Nanoparticles and Their Catalytic Reduction of Oxygen. *Angew. Chem., Int. Ed.* **2008**, *47*, 3588– 3591.

(36) Lord, R. W.; Fanghanel, J.; Holder, C. F.; Dabo, I.; Schaak, R. E. Colloidal Nanoparticles of a Metastable Copper Selenide Phase with Near-Infrared Plasmon Resonance. *Chem. Mater*. **2020**, *32*, 10227-10234.

(37) Fenton, J. L.; Steimle, B. C.; Schaak, R. E. Structure-Selective Synthesis of Wurtzite and Zincblende ZnS, CdS, and $CuInS_2$ Using Nanoparticle Cation Exchange Reactions. *Inorg. Chem.* **2019**, *58*, 672-678.

(38) Norako, M. E.; Brutchey, R. L. Synthesis of Metastable Wurtzite $CuInSe_2$ Nanocrystals. *Chem. Mater*. **2010**, *22*, 1613–1615.

(39) Seo, D.; Park, G.; Song, H. Plasmonic Monitoring of Catalytic Hydrogen Generation by a iSngle Nanoparticle Probe. *J. Am. Chem. Soc*. **2012**, *134*, 1221–1227.

(40) Bao, N.; Shen, L.; Takata, T.; Domen, K. Self-Templated Synthesis of Nanoporous CdS Nanostructures for Highly Efficient Photocatalytic Hydrogen Production Under Visible Light. *Chem. Mater*. **2008**, *20*, 110–117.

(41) Esparza, R.; García-Ruiz, A. F.; Velázques Salazar, J. J.; Pérez, R.; José-Yacamán, M. Structural Characterization of Pt–Pd Core–Shell nanoparticles by Cs-Corrected STEM. *J. Nanoparticle Res.* **2013**, *15*, 1342.

(42) Park, J.; Lim, S.; Kwon, T.; Jun, M.; Oh, A.; Baik, H.; Lee, H. Longitudinal Strain Engineering of $Cu_{2-x}S$ by the Juxtaposed Cu_5FeS_4 Phase in the $Cu_5FeS_4/Cu_{2-x}S/Cu_5FeS_4$ Nanosandwich. *Chem. Mater*. **2019**, *31*, 9070–9077.

(43) Steimle, B. C.; Fagan, A. M.; Butterfield, A. G.; Lord, R. W.; McCormick, C. R.; Di Domizio, G. A.; Schaak, R. E. Experimental Insights into Partial Cation Exchange Reactions for Synthesizing Heterostructured Metal Sulfide Nanocrystals. *Chem. Mater.* **2020**, *32*, 5461-5482.

(44) Sharp, C. G.; Leach, A. D. P.; Macdonald, J. E. Tolman's Electronic Parameter of the Ligand Predicts Phase in the Cation Exchange to $CuFeS_2$ Nanoparticles. *Nano Lett.* **2020**, *20*, 8556–8562.

(45) Williams, A. J.; McQueen, T. M.; Ksenofontov, V.; Felser, C.; Cava, R. J. The Metal–Insulator Transition in $Fe_{1.01-x}Cu_xSe$. *J. Phys.: Condens. Matter* **2009**, *21*, 305701.

(46) Hodges, J. M.; Morse, J. R.; Fenton, J. L.; Ackerman, J. D.; Alameda, L. T.; Schaak, R. E. Insights into the Seeded-Growth Synthesis of Colloidal Hybrid Nanoparticles. *Chem. Mater.* **2017**, *29*, 106-119.

(47) Schaak, R.E.; Williams, M. E. Full Disclosure: The Practical Side of Nanoscale Total Synthesis. *ACS Nano* 2012, *6*, 8492–8497.

Chapter 5

Summary and Outlook

The properties of colloidal nanomaterials are intimately dependent on their morphology, composition, and crystalline phase which has sparked intense research efforts to devise synthetic methods to control these parameters. However, unlike synthetic organic methods, the factors governing nanoparticle nucleation and growth are not well understood. There is a great need to develop synthetic guidelines which allow access to an increasing library of colloidally accessible nanomaterials from single component nanoparticles to more complex multicomponent systems. Seeded growth, the process by which new material domains are nucleated and grown on preformed nanoparticle seeds, has been one of the most versatile methods to increase particle complexity. This complexity however is largely limited to material composition and the resulting particle morphology. As previously mentioned, particle properties are also dependent on crystalline phase, i.e., atomic ordering. Other techniques beyond seeded growth are needed to modulate this property. One such method is through post-synthetic modification by cation exchange.

Cation exchange allows for the post-synthetic exchange of mobile host cations within an anion sublattice with guest cations in solution. The anion sublattices template the incoming guest cations without significant disruption to the overall particle morphology. The post-exchanged product thus takes on the same crystallographic symmetry as the pre-exchanged nanoparticle. Cation exchange can allow access to a larger phase space of materials which are not accessible or easily accessible through direct methods. I have shown in this dissertation how seeded growth (Chapters 2 and 5), direct synthesis (Chapter 3), and cation exchange (Chapters 4 and 5) can be used to synthesize new and increasing complex nanoparticle systems.

In Chapter 2, I discussed the synthesis of heterostructured nanoparticles formed by the seeded growth of transition-metal nitrides (Cu_3N and Cu_3PdN) on noble-metal seeds (Au and Pt). Through a series of selective control experiments, I elucidated the formation pathway of deposited transition metal nitride domain. Using Pt–Cu_3PdN as a model system, it was shown that the depositing transition metal nitride forms step-wise with the initial, indiscriminate deposition of Cu followed by the secondary deposition of Pd onto the edges and corners of the starting crystalline particles. This was followed by the coalescence, localization, and crystallization of deposited Cu and Pd to form the final Cu_3PdN material. It was also observed that the degree of seed faceting determined the resulting heterostructure morphology with higher degrees of faceting favoring core–shell morphologies. When growing Cu_3N on Pt, there was no regioselective growth observed. When growing Cu_3N on Au, AuCu alloy formation was observed instead of heterostructure formation. These insights helped establish synthetic guidelines for tuning the formed particle morphology between core–shell and hybrid as well as the role of secondary metal deposition to localize the seeded particle domain.

In Chapter 3, I demonstrated the colloidal synthesis of a new metastable phase of $Cu_{2-x}Se$. Characterization by EDS and XPS showed the particles possessed a nominal 2:1 stoichiometry (Cu:Se) whereas characterization by XRD did not show any similarity to a known phase of copper selenide. By expanding our search to include other copper chalcogenides, we found that a phase of $Cu_{2-x}Te$, weissite, possessed a similar structure. A structural model was created using weissite Cu_2Te as a template with computationally optimized lattice parameters. Time and temperature studies showed that our weissite-like $Cu_{2-x}Se$ underwent a phase change to the cubic berzelianite phase of $Cu_{2-x}Se$ with prolonged reaction times and at higher temperatures. UV-vis-NIR spectroscopy demonstrated a relatively stable broad plasmon absorbance peak at 1550 nm.

In Chapter 4, I discussed the seeded growth of ternary copper selenides on Pt nanoparticle seeds. It was observed that the ternary copper selenide hybrids form through a multistep process.

Initially, there is a deposition of $Cu_{2-x}Se$ to form Pt-$Cu_{2-x}Se$ hybrid nanoparticles. Then there is a subsequent cation exchange reaction after an injection of the M^{3+} (M = Fe, In) precursor salt solution to form the ternary selenide. When a combination of exchanging metal salts was used, instead of forming heterotrimers only single particle domains were formed giving heterodimers. Analysis by STEM-EDS showed that the newly formed domains consisted of only a single ternary selenide species. Through a series of control experiments, it was observed that the identity of the formed ternary selenide domain corresponded to the fastest exchanging metal cation: In^{3+} exchanging faster than Fe^{3+}. This result provides a qualitative guideline for synthesizing hybrid nanoparticle using *in situ* cation exchange chemistries.

In conclusion, I have described my contributions to the development of synthetic guidelines for the rational design of heterostructured, transition metal nitride nanomaterials by seeded growth demonstrating the role of secondary metals for regioselective deposition. I have shown the discovery of a new, metastable phase of copper selenide nanoparticles with NIR plasmonic absorption. Additionally, I have provided insights into the formation of ternary copper chalcogenides and their competitive synthetic pathways and the development of moderate temperature iron exchange. While probing formation pathways in nanoparticle synthesis remains a challenge for nanosynthetic chemists, insights such as those presented in this dissertation can help develop guidelines which will enable the rational development of designer nanocrystal architectures and new material phases.

VITA

Robert W. Lord

Education

Ph.D. Chemistry (2021) The Pennsylvania State University – *University Park, PA*
B.S. Chemistry (2016) Texas Tech University – *Lubbock, TX*

Honors and Awards

- Continuing Graduate Student Award (2019)
- Sloan Institutional Match Scholarship (2019)
- Department Travel Award (2019)
- Bunton-Waller Graduate Fellowship (2016)

Publications

- Garcia-Herrera, L. F.; McAllister, H. P.; Xiong, H.; Wang, H.; **Lord, R. W.**; O'Boyle, S. K.; Imamovic, A.; Steimle, B. C.; Schaak, R. E.; Plass, K. E. "Multi–Step Regioselectivity and Non–Kirkendall Anion Exchange of Copper Chalcogenide Nanorods," *Chem. Mater.* 2021, accepted.
- Di Domizio, G. A.; Alameda, L. T.; Fanghanel, J.; **Lord, R. W.**; Miller, J. R.; Schaak, R. E. Real-Time Monitoring of Completing Nanoparticle Formation Pathways During Cation Exchange Using Benchtop Light Scattering. *Chem. Mater.* 2021, accepted.
- Hernández-Pagán, E. A.; **Lord, R. W.**; Veglak, J.; Schaak, R. E. "Incorporation of Metal Phosphide Domains into Colloidal Hybrid Nanoparticles," *Inorg. Chem.* 2021, 60, 7, 4278-4290.
- **Lord, R. W.**; Fanghanel, J.; Holder, C. F.; Dabo, I.; Schaak, R. E. "Colloidal Nanoparticles of a Metastable Copper Selenide Phase with Near-Infrared Plasmon Resonance," *Chem. Mater.* 2020, 32, 10227-10234.
- Steimle, B. C.; **Lord, R. W.**; Schaak, R. E. "Phosphine-Induced Phase Transition in Copper Sulfide Nanoparticles Prior to Initiation of a Cation Exchange Reaction," *J. Am. Chem. Soc.* 2020, 142, 13345-13349.
- Steimle, B. C.; Fagan, A. M.; Butterfield, A. G.; **Lord, R. W.**; McCormick, C. R.; Di Domizio, G. A.; Schaak, R. E. "Experimental Insights into Partial Cation Exchange Reactions for Synthesizing Heterostructured Metal Sulfide Nanocrystals," *Chem. Mater.* 2020, 32, 5461-5482.
- Alameda, L. T.; **Lord, R. W.**; Barr, J. A.; Moradifar, P.; Metzger, Z. P.; Steimle, B. C.; Holder, C. F.; Alem, N.; Sinnott, S. G.; Schaak, R. E. "Multi-Step Topochemical Pathway to Metastable Mo_2AlB_2 and Related Two-Dimensional Nanosheet Heterostructures," *J. Am. Chem. Soc.* 2019, 141, 10852-10861.
- **Lord, R. W.**; Holder, C. F.; Fenton, J. L.; Schaak, R. E. "Seeded Growth of Metal Nitrides on Noble-Metal Nanoparticles to Form Complex Nanoscale Heterostructures," *Chem. Mater.* 2019, 31, 4605-4613.